

CIVIL ENGINEERING STUDIES

1 STRUCTURAL RESEARCH SERIES NO. 314



EVALUATION OF FLOW AND FRACTURE PROPENSITY OF NOTCHED STEEL PLATES BY MEANS OF A PHOTOELASTIC MODEL

Metz Reference Room
Civil Engineering Department
3106 C. E. Building
University of Illinois
Urbana, Illinois 61801

by
J. P. CANNON
and
W. H. MUNSE

A Technical Report
to the
SHIP STRUCTURE COMMITTEE
under
DEPARTMENT OF THE NAVY
Bureau of Ships Contract Nobs 88283
Project Serial No. SF 0130304, Task 2022
Project SR-149

UNIVERSITY OF ILLINOIS
URBANA, ILLINOIS
AUGUST 1966

EVALUATION OF FLOW AND FRACTURE PROPENSITY
OF NOTCHED STEEL PLATES BY MEANS
OF A PHOTOELASTIC MODEL

by

J. P. Cannon

and

W. H. Munse

A Technical Report
to the
SHIP STRUCTURE COMMITTEE
Under
DEPARTMENT OF THE NAVY

Bureau of Ships Contract Nobs 88283
Project Serial No. SF 0130304, Task 2022
Project SR-149

University of Illinois
Urbana, Illinois

August 1966

ABSTRACT

The object of this investigation was to gain a better understanding of the flow and fracture propensity of steel plates in which the Wells-type notch served as the fracture initiator. This type of notch is of importance in experimental investigations of the brittle fracture phenomenon because it successfully initiates low-stress brittle fractures in the wide-plate specimen in which it is used. The wide-plate specimen is thought to simulate effectively circumstances associated with known brittle fractures occurring in engineering practice.

The magnitude of the brittle fracture problem in steel structures is reviewed in general terms, as well as by citing representative case histories. A review of the most notable theoretical investigations of brittle fracture is given, including the Griffith theory, the Orowan-Irwin modification of the Griffith theory to account for notch-brittle materials, and highlights from the fracture mechanics approach to the brittle fracture problem. The factors affecting brittle strength are examined, with an emphasis on the concept of notch-constraint by which normally ductile metals, such as steel, can be induced to fracture in a brittle manner. Experimental brittle fracture studies are reviewed with an emphasis on tests of notched and welded wide-plates, for which representative data are discussed.

A model of the vicinity of the Wells notch used in the wide-plate tests was designed and fabricated out of epoxy material into which birefringence was "frozen." The use of three-dimensional

photoelasticity to examine the stresses in this model, which was loaded so as to simulate the wide-plate specimen, allowed detailed investigation of the stresses in the immediate notch vicinity. Isochromatic fringe photographs were obtained for both surface and mid-thickness slices of the model. Detailed investigation of the stress-state in material in the vicinity of the notch was conducted on sub-slices of the model examined under polarized light. From this investigation the von Mises equivalent yield stress, σ_e , and the maximum normal stress, σ_1 , in the vicinity of the notch were determined. Under the assumption that fracture is broadly a function of maximum normal stress, while flow is tied to the von Mises equivalent yield stress, flow and fracture propensity of material in the vicinity of the notch is appraised.

Very high strain concentrations were found to exist on the perimeter of the Wells notch with a maximum elastic concentration of the order of 13 occurring at the notch-tip. Severe constraint against plastic flow was found to exist a short distance from the tip of the Wells notch. This region is postulated to constitute a vicinity of increased susceptibility to cleavage type fracture. On the basis of the stresses found to exist in the Wells notch, three fracture initiation mode possibilities are postulated: (a) a shear mode, initiating at the notch-tip, leading to ductile fracture, (b) shear fracture, initiating at the notch-tip, converging into a cleavage fracture as the region of high triaxiality becomes involved in the fracture process, and (c) cleavage fracture initiating in the region of high triaxiality away from the notch-tip.

ACKNOWLEDGMENT

This investigation was carried out as part of the research program of the Department of Civil Engineering, University of Illinois. Initially, the study was conducted as part of a research project sponsored by the Ship Structure Committee, National Academy of Sciences for the Bureau of Ships, U. S. Navy.

Dr. C. E. Taylor, Department of Theoretical and Applied Mechanics, was consulted on the photoelastic aspects of the study. His assistance is gratefully acknowledged.

Others, too numerous to mention individually, have rendered helpful assistance with preparation of figures, machining and preparation of specimens, general laboratory work, typing and reproducing. The help of these, too, is appreciated.

TABLE OF CONTENTS

	Page
Acknowledgment.	iii
List of Tables.	vi
List of Figures	vii
CHAPTER 1. THE BRITTLE FRACTURE PROBLEM IN REVIEW.	1
1.1. The Brittle Fracture Problem.	1
1.2. Review of Brittle Fracture Theory	7
1.3. Review of Experimental Brittle Fracture Studies	14
1.4. Factors Affecting Brittle Fracture Strength	17
CHAPTER 2. OBJECT AND SCOPE OF THIS INVESTIGATION.	21
CHAPTER 3. NOTCHED AND WELDED WIDE-PLATE TESTS	23
3.1. Introduction.	23
3.2. Wide-Plate Specimen	23
3.3. Test Procedure.	24
3.4. Selection of Representative Tests	25
3.5. Presentation and Discussion of Test Results	26
CHAPTER 4. PHOTOELASTIC STRESS ANALYSIS OF WELLS NOTCH	32
4.1. Introduction.	32
4.2. Theory of Three-Dimensional Photoelasticity	33
4.3. Epoxy Model of the Wells Notch: Design, Fabrication, and Loading.	36
4.4. Isochromatic Fringe Photographs of Selected Model Slices.	39
4.5. Determination of the von Mises Equivalent Yield Stress.	42
4.6. Determination of Maximum Normal Stress on Notch Boundary.	46
CHAPTER 5. FLOW AND FRACTURE IN THE PROTOTYPE NOTCHED PLATE.	54
5.1. Introduction.	54
5.2. Degree of Simulation of the Prototype by the Epoxy Model	54
5.3. Maximum Normal Stress and von Mises Equivalent Yield Stress at Specimen Mid-Thickness.	57
5.4. Origin and Development of Fracture.	59
5.5. Possible Sources of Disparity in the Wide-Plate Test Results.	64
CHAPTER 6. SUMMARY AND CONCLUSIONS	67

TABLE OF CONTENTS (Continued)

	Page
BIBLIOGRAPHY	71
TABLES	75
FIGURES	85
APPENDIX A. PRINCIPLES OF PHOTOELASTICITY	124
A.1. Stress-Optical Properties of Birefringent Materials	124
A.2. Photoelastic Determination of the Von Mises Equivalent Yield Stress	128
Figures	134
APPENDIX B. NOTATION	136

LIST OF TABLES

Number		Page
1.1	Details of Five Cases of Field Brittle Fractures . . .	75
1.2	Crack-Extension Force, G, for Five Configurations. . .	76
3.1	Material Properties of Specimens Used in Wide-Plate Tests.	77
3.2	Wide-Plate Test Data: Series 1.	78
3.3	Wide-Plate Test Data: Series 2.	79
3.4	Wide-Plate Test Data: Series 3.	80
3.5	Wide-Plate Test Data: Series 4.	81
3.6	Wide-Plate Test Data: Series 5.	82
3.7	Wide-Plate Test Data: Series 6(a)	83
3.8	Wide-Plate Test Data: Series 6(b)	84

LIST OF FIGURES

Number		Page
1.1	Fracture of an Oil Storage Tank	85
1.2	Vertical Pressure Vessel With Lug Support Detail . . .	86
1.3	Griffith-Irwin Crack Extension Model	87
1.4	Fracture Stress Versus Notch Depth for Notched Plate Tests on Ship-Steel (After Orowan and Felbeck ⁽¹⁴⁾) . .	88
1.5	Stress-Strain Plot Showing the Concept of Notch Brittleness (After Orowan ⁽¹²⁾)	89
1.6	The Role of the Relative Temperature Dependencies of the Processes of Flow and Fracture in Determining the Transition Temperature (After Gensamer ⁽³⁷⁾)	90
3.1	Wide-Plate Specimen and Wells Notch Detail	91
3.2.	Fracture Stress Versus Test Temperature, Wide-Plate Test Series 1	92
3.3.	Fracture Stress Versus Test Temperature, Wide-Plate Test Series 2	92
3.4	Fracture Stress Versus Test Temperature, Wide-Plate Test Series 3	93
3.5	Fracture Stress Versus Test Temperature, Wide-Plate Test Series 4	94
3.6	Fracture Stress Versus Test Temperature, Wide-Plate Test Series 5	94
3.7	Fracture Stress Versus Test Temperature, Wide-Plate Test Series 6(a).	95
3.8	Fracture Stress Versus Test Temperature, Wide-Plate Test Series 6(b).	95
4.1	Two-Phase Model Illustrating Accomplishment of Stress Freezing	96
4.2	Isochromatic Fringe Photograph of Calibration Beam Into Which Stresses Have Been Frozen.	97

LIST OF FIGURES (Continued)

Number		Page
4.3	Unassembled Components of Epoxy Model of Wells Notch	98
4.4	Epoxy Model of Wells-Type Notch.	99
4.5	Beam Calibration Specimen and Curve for Determination of Stress-Optical Constant, F.	100
4.6	Isochromatic Fringe Photograph of Unsliced Model; $m = 1$	101
4.7	Isochromatic Fringe Photograph of Surface Slice of Model; $m = 3$	102
4.8	Isochromatic Fringe Photograph of Surface Slice of Model; $m = 5$	103
4.9	Isochromatic Fringe Photograph of Surface Slice of Model; $m = 7$	104
4.10	Isochromatic Fringe Photograph of Mid-Thickness Slice of Model; $m = 3$	105
4.11	Isochromatic Fringe Photograph of Mid-Thickness Slice of Model; $m = 5$	106
4.12	Photograph of Polarizing Microscope.	107
4.13	Von Mises Equivalent Stress at Selected Points	108
4.14	Von Mises Equivalent Stress at Selected Locations on Notch Perimeter	109
4.15	Regions for Which Boundary Stresses, σ_y , are Determined	110
4.16	Secondary Principal Stress-Difference, $\sigma_{1z} - \sigma_{3z'}$, In Vicinity of Notch-Tip: Region 1.	111
4.17	Secondary Principal Stress-Difference, $\sigma_{1x} - \sigma_{3x'}$, In Vicinity of Notch-Tip: Region 1.	112
4.18	Secondary Principal Stress-Difference, $\sigma_{1z} - \sigma_{3z'}$, In Vicinity of Notch-Flat: Region 2	113
4.19	Secondary Principal Stress-Difference, $\sigma_{1z} - \sigma_{3z'}$, Near Notch Boundary and Model Surface: Region 3	114

LIST OF FIGURES (Continued)

Number		Page
4.20	Secondary Principal Stress-Difference, $\sigma_{1z'} - \sigma_{3z'}$, Near Notch Boundary and Model Surface: Region 4 . . .	115
4.21	Secondary Principal Stress-Difference, $\sigma_{1x} - \sigma_{3x}$, Near Notch Boundary and Model Surface: Region 3 . . .	116
4.22	Secondary Principal Stress-Difference, $\sigma_{1x} - \sigma_{3x}$, Near Notch Boundary and Model Surface: Region 4 . . .	117
4.23	Secondary Principal Stress-Difference, $\sigma_{1x} - \sigma_{3x}$, At Model Surface, Versus Specimen Thickness: Regions 3 and 4.	118
4.24	Maximum Normal Stress, σ_y , at Selected Points on Notch Perimeter.	119
5.1	Maximum Normal Stress and Von Mises Equivalent Stress in Vicinity of Notch-Tip	120
5.2	Ratio of Maximum Normal Stress and Von Mises Equivalent Stress Versus Distance From Notch-Tip . . .	121
5.3	Photomicrograph (200X) Showing Cleavage Crack Initiation (Arrow) in Region Away From Notch Root (From Knott and Cottrell ⁽⁴⁹⁾).	122
5.4	The Role of a Notch in the Dual Fracture Mode Behavior of Steel (After Otani and Ideguchi ⁽⁵¹⁾) . . .	123
A.1	Retardation of Polarized Light Transmitted Through a Plane-Stress Model	134
A.2	Secondary Principal Stresses in Arbitrarily Oriented Cubes Cut From Model Into Which Stresses Have Been Frozen	135

CHAPTER 1

THE BRITTLE FRACTURE PROBLEM IN REVIEW

1.1. The Brittle Fracture Problem

The incidence of catastrophic brittle fractures in structures and structural components has reached proportions which identify this failure mode as one which must be taken into account increasingly by the structural designer. That this accounting is not made by application of conventional design is evidenced by the occasional occurrence of brittle-type fractures in structures subjected to forces no greater than those arising from assigned service loads. A discussion of five documented cases which are representative follows, with a summary of the material properties and failure details given in Table 1.1.

Case 1: Storage Tank^{(1)*}

A welded oil storage tank recently failed in a brittle manner after four and one-half years of service. This cylindrical tank, of 2 800 000 gal capacity, stood 36 ft high and had a diameter of 115 ft. The tank was fabricated of steel plates in six courses ranging in thickness from 0.59 in. at the bottom of the tank to 0.24 in. at the top (Fig. 1.1). All plates on the three lower courses were butt-welded; however, the circumferential joints between the three upper courses were made with fillet welds. The bottom course was fillet welded, inside and out, to the tank bottom plate.

*Numbers in parentheses refer to bibliography entries.

The tank contained fuel oil to a height of 25 ft at the time of failure. The associated nominal circumferential membrane stress in the lower course was computed to be 12 ksi. The ambient temperature was 5°F with the steel temperature at the point of fracture initiation estimated to be between 5° and 30°F. The fracture occurred suddenly and with no prior warning. The main failure initiated in the lowest course plate, at its junction with the tank bottom, and traversed vertically the entire tank height. The initial portion of the fracture was a brittle cleavage-type fracture, with the final portion being a more ductile shear-type fracture. The brittle fracture constituted two-thirds of the total fracture length, as shown in Fig. 1.1. The crack initiator was determined to be a small crack (1/4 in. x 1/2 in.) in the bottom course plate in the immediate vicinity of the junction between this plate and the tank bottom. It was determined, by post-fracture examination, that the crack existed in the plate prior to welding. The path of the fracture and the details of the initiator crack are shown in Fig. 1.1. It should be noted in passing that there was secondary fracturing in other regions of the tank, undoubtedly triggered by the main fracture.

Case 2: Unfinished Ship⁽²⁾

A brittle fracture is reported to have occurred in an unfinished ship, while it was still on the building way, through a steel which generally would not be considered brittle. The material had a Charpy V-notch energy absorption of 50 ft-lb at 5°F. The fracture occurred at 41°F near the forward end of the poop deck in a ship of 8500 tons dead weight. Several stiffening members of different

orientations met at this point, which implies the existence of a high triaxial state of stress. The design of this detail was poorly conceived and executed, and no doubt contributed to the initiation of the failure.

Case 3: Welded Oil Tanker⁽³⁾

In November 1960 a brittle fracture occurred in a welded oil tanker (12 000 gross tons) which had been constructed in 1952. While the docked ship was being loaded, a large crack developed in the upper deck at about midship. The partially-loaded tanks were thought to produce nominal tensile stresses in the upper deck of approximately 14 ksi. The crack initiated in the 7/8-in. deck-plate at a flame-cut float gauge opening, having a shape approximating an ellipse with a minor axis of 2.5 in. and a major axis of 8.0 in. The ship's longitudinal direction, corresponding to the direction of maximum tensile stress, was perpendicular to the major axis of the gauge opening. Cracks propagated from both ends of the opening in a direction perpendicular to that of the maximum tensile stress. The major crack propagated completely across the width of the deck-plate in which it initiated and continued across one quarter of the width of the adjacent deck-plate, where it arrested some ten feet from its point of initiation. The shorter crack traversed some two feet from the gauge opening before arresting in the weld material between deck-plates. The fractured surface in the immediate vicinity of the gauge opening was rusted, suggesting that time had elapsed between the formation of the initial crack and the onset of rapid brittle fracture. The surface of the latter was new and crystalline in appearance. The

steel deck-plate material had a yield point of 40 ksi, a value considerably greater than the nominal stress in the deck at the time of failure, and showed 23.5% elongation to fracture on an 8-in. gauge length. This material conformed to the required standards for ship-building steels which prevailed at the time of the tanker's construction.

Case 4: Pressure Vessel⁽¹⁾

Case 4 involves the fracture of a pressure vessel used as a regenerator. The vertically-oriented cylindrical pressure tank was 4 ft in diameter and 15 ft long with a wall thickness of 0.4 in. (Fig. 1.2). During service, air at a temperature of 68°F and a pressure of 3 atm (44 psi) was exchanged abruptly with nitrogen at -356°F and 0.1 atm (1.5 psi). Each gas occupied the vessel for about three minutes before the next change. The nominal air pressure induced a nominal tank-wall membrane stress of approximately 3 ksi. The failure occurred after eight months of service, by which time the vessel had been subjected to 115 000 cycles of the previously-mentioned gas exchange. The completely brittle fracture was attended by a loud report, occurring at the moment of one of the abrupt gas exchanges. Fracture initiation occurred at a fatigue crack which had developed at one of four supporting lugs located near the bottom of the vessel (Fig. 1.2). The fracturing directions were random at the bottom of the vessel where the temperature was lowest, changing to a generally vertical direction toward the top. Cracking was arrested in material with a temperature of about 32°F.

Case 5: Railway Tank Car⁽¹⁾

This case involves the brittle fracture of a railway tank car used for transporting liquified gas. The car was cylindrical in shape, having a diameter of approximately 10 ft, a length of approximately 40 ft, and a tank-shell thickness of 0.7 in. The car had been in service for sixteen years at the time of the fracture occurrence. The loading imposed on the car was 28 tons of gas, composed of 56% butane, 40% propane, and small amounts of ethane and methane, confined under 4 atm of pressure at a temperature of 25^oF. The tank-car-shell material was a carbon-steel plate with a yield point of approximately 45 ksi and an ultimate strength of approximately 73 ksi. The occurrence of the fracture was initiated by the impact on the car caused by shunting. The fracture originated from a fatigue crack at the welded junction of a T-section, which was one of four sections supporting the tank at each of four corners, and the tank proper. The fracture traversed in a direction generally parallel to the longitudinal axis of the tank, for a total crack distance of ten or twelve ft. The tank shell subsequently exploded after the initial fracture had allowed leakage and ignition of the tank contents. An interesting aspect of the support detail for the tank is that a reinforcing weld had been applied to it by the builder in a purposeful attempt to improve the strength at that point. This reinforcing weld proved to be the stress-raiser from which the fatal crack initiated.

Though these cases are representative of the kinds of brittle fractures which have developed, they do not adequately convey an appreciation for the total number of brittle fractures occurring in the past

quarter-century. A search of the literature confirms that there have been many failures in which such fractures occurred. Shank's survey⁽⁴⁾ treats 58 failures of non-ship structures fabricated from mild-steel plate. Included in this survey are such structures as standpipes, pressure vessels, tanks (oil, water, molasses), penstocks, gas lines, power shovels, and bridges. Hodgson and Boyd⁽⁵⁾ summarize failures of 87 riveted and 95 welded ships built from 1945 to 1956 in foreign ship yards. Brittle fractures in ships built in this country have been numerous and are well documented in the literature.^(6,7) The welded tankers fabricated in connection with World War II proved particularly susceptible to brittle fracture. Of 569 all-welded tankers, 118, or 20.7%, developed brittle fractures of sufficient severity to render the vessels temporarily or permanently useless or dangerous. Eighty-eight out of 599 (14.7%) tankers, purposely riveted in regions of high fracture susceptibility, developed brittle fractures. Failure rates for cargo and/or passenger ships were somewhat lower, being 16.8% in 3498 vessels and 10.5% in 3093 vessels for all-welded and partially-riveted ships respectively. These data represent only ships longer than 300 ft and do not include failures subsequent to March 31, 1952.⁽⁷⁾

The alarming wartime rate of ship brittle fractures has been arrested, due to increased understanding of brittle fracture resulting largely from intense study inspired by the problem itself. Continued attention to and accounting for this problem is imperative, for brittle fractures still occur. Fractures have occurred, subsequent to World War II, in gas transmission lines, in pressurized-cabin commercial jet planes, in large steam turbine-generator rotors, and in pressure vessels of many kinds.⁽⁸⁾

The future incidence of brittle fractures cannot be predicted with certainty. However, the trend toward the use of less ductile higher strength materials has brittle fracture implications to which the structural engineer must give increasing attention. Raising a material's static yield strength does not, in general, raise its brittle strength by a commensurate amount. Thus, as material yield strength is increased, conventional elastic design, in which member stresses are in direct proportion to the yield stress (for a given factor of safety), is increasingly unconservative with respect to brittle fracture. Use of design procedures which assume that structural strength is independent of the elastic stress distribution must also be used with caution in structural components which are susceptible to brittle fracture. This assumption, while simplifying the stress analysis and design, will not necessarily be honored by brittle fracture.

1.2. Review of Brittle Fracture Theory

Griffith^(9,10) is responsible for the most widely accepted crack-extension theory, which he proposed nearly a half century ago. His effort was stimulated by the inconsistency between the theoretical strength of solid bodies and their observed strength. He postulated that the discrepancy between these two strengths was due to the presence of cracks in the material. By utilizing an energy approach, he evaluated the effect of these cracks on strength. The fundamental concept which distinguishes Griffith's theory is his recognition of the fact that the boundary between crack stability (non-extension) and crack instability (extension) is marked by unchanging total potential energy.

energy of the system when small variations in crack length are permitted. Griffith further recognized that, for a completely brittle material, the potential energy serving to resist crack extension arises from the surface tension between the crack faces. The potential energy, W , of these forces tending to resist crack extension can be written as $W = 4a\alpha$, where a is half crack length and α is the surface tension. Figure 1.3 shows the model, of unit thickness, which Griffith used for his development.

For crack instability to be possible, the potential energy due to the surface tension must be overcome by energy tending to promote crack extension. The crack-promoting energy derives from the stressed body's strain energy which is available for release by an extending crack. The strain energy term, U , attributable to the crack, has been shown to be equal to the work done by forces, acting at the crack boundary, to close the crack.⁽¹¹⁾ For a state of plane-stress, this is equal to $\frac{\pi a^2 \sigma^2}{E}$, where σ is the uniform tensile stress (Fig. 1.3). From the two energy contributions, W and U , the Griffith criterion for crack extension can be obtained by differentiating the total system potential, $V = W + U$, with respect to crack length, a , and setting the result equal to zero. This yields

$$\sigma = \sqrt{\frac{2\alpha E'}{\pi a}} \quad (1.1)$$

Griffith's theory, then, predicts rapid crack extension when the rate of strain energy released becomes as great as the rate at which energy can be absorbed by the surface tension forces, both rates being taken with respect to crack length. It remains to note the assumptions

which must be satisfied in order for the Griffith theory to have validity. The first assumption requires a completely brittle material in that the work done in resisting crack extension must be provided entirely by the surface tension forces. A clear violation of this assumption would be the existence of yielding of material in the vicinity of the extending crack, which would add a plastic work term to the energy tending to resist crack extension. Secondly, the Griffith theory is a linear elastic theory and, thus, depends on the validity of Hooke's Law, thereby utilizing a constant modulus of elasticity, E . Finally, the assumption of a plane crack front is utilized.

The wide usage to which the Griffith formulation has been put derives in large part from the consistency between the predicted strengths and the actual strengths realized in specimens for which the Griffith assumptions are satisfied. Griffith^(9,10) provided laboratory verification of his theory, utilizing specimens of glass into which cracks were etched. Subsequent corroboration of Griffith's theory has been provided by other investigators who recognized and accounted for its limitations.

Orowan⁽¹²⁾ and Irwin,⁽¹³⁾ conducting independent investigations, have suggested a modification of Griffith's theory in an attempt to overcome Griffith's principal limitation, that of requiring completely brittle material. Their modification introduces a second term in the formulation of the energy which resists crack extension. For steel and other ductile materials, this term derives from the plastic work which is performed on the material in the immediate vicinity of a propagating

crack. Orowan and Irwin recognized that this plastic work term can be superimposed directly with the surface tension term, α , provided the plastic work is confined to a thin layer of material at the fracture surfaces. It has further been determined that this plastic work term for steel renders the surface tension term negligible, because the former is three or four orders of magnitude greater than the latter. (12,14) Utilizing these assumptions and approximations, the Griffith-Orowan-Irwin equation becomes

$$\sigma_f = \sqrt{\frac{EG_c}{\pi a}} \quad (1.2)$$

where G_c is the energy associated with mating crack surfaces. The term, G_c , contributed by the plastic work in the vicinity of the new crack surfaces, has been termed crack-toughness in the so-called "Fracture Mechanics" approach. (8)

The fracture mechanics approach, advanced primarily by Irwin and his associates, is the foundation for the most significant fracture theory currently in use. (8, 15,16,17,18) The wide acceptance of this philosophy as a standard has had a great impact, too, on experimental fracture work, which has often been designed to confirm or adjust existing fracture mechanics postulates and provide an evaluation of the parameters in the terms of which fracture mechanics concepts are formulated. Fracture mechanics does not represent an abandonment of the Griffith principles. Rather, the Griffith theory, as modified to account for notch-brittle materials, is the starting point for the formulation of the theory of fracture mechanics.

The dimensional equivalence of Griffith's crack-resisting term, α , and notch-toughness, G_c , for the model of Fig. 1.3, can be confirmed by comparing Eqs. (1.1) and (1.2) from which it is seen that $G_c = 2\alpha$. The Griffith strain energy release-rate is generalized by Irwin, renamed crack-extension force, and denoted G . The crack-extension force, G , for the Griffith model, can be inferred from Eq. (1.2) which can be written, for non-fracture conditions, as

$$\sigma = \sqrt{\frac{EG}{\pi a}} \quad (1.3)$$

from which

$$G = \frac{\pi a \sigma^2}{E} \quad (1.4)$$

It is apparent that when the crack-extension force, G , becomes equal to the "crack-resisting force" or notch-toughness, G_c , the fracture condition is satisfied (Eq. (1.2)) and rapid fracture ensues. The crack-extension force, G , and its counterpart, notch-toughness, G_c , are referred to a unit thickness of material in the plane of the crack and perpendicular to the direction of crack advancement. Strain energy release-rates have units of force confirming the correctness of Irwin's "crack-extension force" terminology, while G , and G_c , have units of force per length, seen to be consistent with Eq. (1.2), (1.3), and (1.4).

Seeking a more thorough understanding of the source of fracture occurrence, Irwin found a unique relationship between the stresses in the immediate vicinity of the advancing crack and the crack-extension force, G .^(16,8) The stress analysis by which this was accomplished

utilized a stress function approach suggested by Westergaard.⁽¹⁹⁾ The plane-stress components of the stress tensor in the immediate vicinity of the crack tip, i.e., for small r , were thus found to be

$$\begin{aligned}\sigma_x &= \sqrt{\frac{GE}{\pi}} \frac{\cos \theta/2}{\sqrt{2r}} \left(1 - \sin \frac{\theta}{2} \sin \frac{3\theta}{2}\right) + \text{constants} \\ \sigma_y &= \sqrt{\frac{GE}{\pi}} \frac{\cos \theta/2}{\sqrt{2r}} \left(1 + \sin \frac{\theta}{2} \sin \frac{3\theta}{2}\right) \\ \tau_{xy} &= \sqrt{\frac{GE}{\pi}} \frac{\sin \theta/2}{\sqrt{2r}} \left(\cos \frac{\theta}{2} \cos \frac{3\theta}{2}\right)\end{aligned}\tag{1.5}$$

where r and θ are polar coordinates, referenced from the crack tip as shown in Fig. 1.3. For plane-strain the values are multiplied by $\sqrt{\frac{1}{1-\mu^2}}$ where μ is Poisson's ratio. This relationship between crack-extension force, G , and the stress distribution immediately surrounding a notch is general and applies to a wide range of cracking and loading configurations. A stress distribution of similar form had been obtained by Inglis⁽²⁰⁾ and others for a model similar to that of Fig. 1.3. Irwin's contribution was to link these stresses with crack-extension force and to extend the result to a sufficient number of configurations to permit generalization.⁽¹¹⁾

A useful term, stress-intensity factor, K , defined as the common factor of all of the stress components of Eq. (1.5), can be written as

$$K = \sqrt{\frac{GE}{\pi}}^* \quad \text{or} \quad G = \frac{\pi}{E} K^2 \tag{1.6}$$

* Alternatively, the stress-intensity factor is sometimes defined by $K = \sqrt{GE}$.

It can be seen from Eq. (1.5) that the value of the normal stress, σ_y , as r approaches zero along the line $Y = 0$ (i.e., $\theta = 0$), can be defined in terms of K as

$$\sigma_y = \frac{K}{\sqrt{2r}} \quad (1.7)$$

Alternatively, the stress-intensity factor can be defined as

$$K = \lim_{r \rightarrow 0} \sqrt{2r} \sigma_y \quad (1.8)$$

The practical application of fracture mechanics involves the determination of a crack-extension force, G , (or alternatively a stress-intensity factor, K) and a notch-toughness, G_c , (alternatively K_c). The former, G , depends on the size and shape of both the member and the crack, and on the applied boundary forces. Crack-extension force values for several configurations are shown in Table 1.2. The crack-toughness, G_c , is defined for a material in a particular condition as the value of crack-extension force at which crack propagation impends.⁽¹¹⁾ Notch-toughness can be measured in the laboratory by destructive testing of specimens for which values of crack-extension force can be calculated. This type of testing must be cautiously applied to steel because of the possibility of initiation's being suppressed, even though conditions exist that will support propagation.⁽¹¹⁾ The mechanism by which initiation is checked is not thoroughly understood, though it may be related to steel's possession of at least two separate fracture modes, one brittle, the other ductile. This dual behavior, known as "notch-brittleness," will be discussed in section 1.4. The amount by which G_c

exceeds G , calculated for service loads, provides a measure of the margin of strength against fracture occurrence under service loads.

As in the Griffith theory, linear elasticity was presumed in the fracture mechanics formulation. The widely held view^(8,11,12) that fracture, at least of steel, is always preceded by some plastic flow at the notch root, renders the formulation somewhat incorrect at the outset. There are many problems, however, for which the assumption of a linear stress-strain relationship represents a useful approximation. The cases for which this error becomes inadmissible can often be treated by adopting a modified-crack-length concept, in which the plastic zone size is considered to add, for purposes of G_c calculations, an increment of crack length to the real crack length.⁽⁸⁾ More refined treatment of the effect of the inelasticity which is inherent in the problem awaits the availability of a more thorough plasticity analysis.⁽¹¹⁾

1.3. Review of Experimental Brittle Fracture Studies

Experimental investigation of the brittle fracture phenomenon has closely paralleled the theoretical studies and has provided important verification and modification of theoretical results. Griffith supported his theoretical formulation with an ingenious set of tests conducted with small, spherical glass pressure-vessels into which cracks, of measurable and controllable dimensions, were etched.^(9,10) The results of these tests were in substantial agreement with his theoretical predictions. More recent experimental work has been stimulated largely by the need to extend Griffith's work to more commonly used structural

materials, that is materials which, rather than being completely brittle, exhibit some plastic deformation before the onset of brittle fracture.

Tests on small-scale specimens have been conducted for many years to determine the energy-absorbing capacity of structural material when subjected to environment conducive to brittle fracture. An example of this type of test is the Charpy V-notch impact test. One shortcoming of such a test is the inability of this specimen and the load to which it is subjected to duplicate, or adequately simulate, the conditions to which actual structures or structural components are subjected. Notable attempts have been made in experimental investigations to alleviate, if only partially, this shortcoming. Parallel experimental investigations have accompanied the evolution of the modified Griffith formulation, taking into account the lack of complete brittleness in real structural materials such as steel. Orowan and Felbeck⁽¹⁴⁾ conducted an experimental investigation using material from a ship which had failed by brittle fracture. Test specimens consisted of intermediate-sized notched steel plates in which the notch depth was carefully controlled and measured. These specimens were subsequently loaded to failure with tension applied perpendicularly to the plane of the crack. The results relating fracture stress and crack length are plotted in Fig. 1.4. These tests would seem to provide substantial verification for the inverse square root influence of crack length on fracture strength which is predicted by the Griffith theory. Many tests on similar intermediate-sized specimens have been conducted since the development of Irwin's fracture mechanics approach to provide verification and extension of this philosophy. (18,21,22)

Since 1945 important tests have been conducted on notched and welded wide-plates. These tests, which are classified as large-scale tests, have contributed significantly in rendering the fracture mechanics approach operational. They have also provided much information in their own right concerning the factors which determine brittle fracture strength of structural components and the relative influence of these factors. A valuable contribution made by wide-plate tests is that of simulating more completely the conditions to which actual structures are subjected in the field. This is reflected by the behavior of wide-plate specimens which often fail in a manner similar to that observed in structures.

The development of a successful low-fracture-stress wide-plate test specimen was a process which initially met with failure. It was Kennedy⁽²³⁾ who conducted the first wide-plate test which resulted in a truly brittle low-stress fracture. His tests also considered such variables as temperature, residual stress, heat treatment after welding, preheating, plate thickness, mechanical discontinuities in the form of notches or flaws, welding voltage, general geometry, and methods of loading. Many of his conclusions relating these variables to brittle fracture likelihood are considered valid today. Greene⁽²⁴⁾ conducted a series of wide-plate tests, the primary objective of which was the evaluation of the effect of residual stresses on fracture strength. In more recent years, wide-plate tests with a variety of objectives have been conducted in several countries. Noteworthy among these is the work of Wells and his associates in England,^(25,26,27,28,29,30,11) Kihara and his associates from Japan,⁽³¹⁾ and several investigators in

the United States, especially at the University of Illinois^(32,33,34,35) and the University of California.⁽³⁶⁾ The details of the typical notched and welded wide-plate specimen, as well as some of the more important test results, will be outlined in a separate chapter.

1.4. Factors Affecting Brittle Fracture Strength

A concise delineation of the factors which affect brittle fracture is rendered impossible by the complexity of the problem, although several such factors have been identified by intensive theoretical and experimental investigations into the nature of the fracture process. The relative influence of and the interaction between these various factors have not been fully evaluated, and it is not likely that they soon will be. Some of the factors, and an indication of the extent to which they affect fracture, are suggested by previous theoretical and experimental studies, the highlights of which are summarized in the preceding two sections. It is seen from Eq. (1.3) that applied stress and flaw size are two such factors. It is not as apparent which factors contribute, or in what amount, to the so-called fracture-toughness, G_c .

The plot of Fig. 1.5 attempts to conceptualize, if only in a qualitative way, some of the factors which contribute to the occurrence of fracture.⁽¹²⁾ Maximum normal stress is plotted against true plastic strain. Curve "Y_d" is the yield, or flow, stress-strain curve of a ductile metal in an ordinary tensile test. This curve terminates with ductile fracture which is accompanied by considerable plastic deformation. It is postulated that there exists a characteristic brittle

strength curve which is represented as curve "B." If a normal environment exists, metal will show a preference for the ductile mode of failure, that is curve Y_d , or its associated ductile fracture, is everywhere lower than curve B. Yielding occurs, followed by fracture in a shear failure mode, before normal stresses sufficient to cause brittle fracture are reached. The flow stress-strain relationship represented by curve Y_d is not unalterable; it can be changed to attain brittle fracture in place of the usual ductile failure mode. Designating a constraint factor, q , as the amount by which the curve Y_d is raised for a given strain, one can visualize the possibility of the elevated curve, " qY_d ," intersecting the brittle curve, B, resulting in a brittle fracture condition. The ductile fracture condition is precluded, in this case, by insufficient deformation. One factor which can alter the stress-strain properties of a material is temperature. It is well known that lowering the temperature can significantly raise the yield stress of a metal, which in terms of Fig. 1.5 is equivalent to $q > 1.0$. It is also known that material yield point is raised by increasing strain-rate, thereby giving values of $q > 1.0$. Materials whose flow characteristics are not much influenced by temperature and strain-rate exhibit fracture behavior which is, predictably, not strongly temperature or strain-rate dependent. (8) A third, more realistic, mechanism by which the flow curve, Y_d , can be raised to intersect the brittle strength curve, B, is the addition of what can be termed a constraint, which restricts the flow of the material, thereby providing the support for higher maximum normal stress. The most obvious way of altering the relationship between tendency to flow,

which is a function of the difference in principal stresses, and the tendency to fracture, which is postulated to be tied to the maximum normal stress, is to change the state of stress acting on the body.

As examples of the role of state of stress on the tendency for brittle fracture, several types of specimens may be considered. A specimen loaded in torsion has a difference in principal stresses, $\sigma_1 - \sigma_3$, equal to twice the maximum normal stress, σ_1 , which results in a maximum shear stress, τ_{\max} , equal to the maximum normal stress. On the other hand, an unnotched tensile specimen has a maximum normal stress equal to twice the maximum shear stress. These examples indicate that the tensile test constrains or prevents material flow in comparison with the torsion test, given that the maximum normal stress, σ_1 , is kept constant between the two tests. These principles are illustrated schematically in Fig. 1.6, where the effect of the state of stress, as determined by the type of test, on propensity to fracture brittly is shown. (37) The plot in Fig. 1.6 also illustrates the concept of transition temperature, marking the temperature boundary between ductile and brittle behavior. This temperature is obviously not an invariable material property, but is related, among other things, to stress-state or test-type. The final type of test which is illustrated in Fig. 1.6 is that of the notched wide-plate tensile test specimen, which exhibits more constraint against plastic flow, through the introduction of tri-axial tensions in the notch vicinity, than does the unnotched tensile test specimen.

Because a material can exhibit ductile behavior in the unnotched condition, and brittle behavior when a notch is introduced,

it is termed a "notch-brittle" material.⁽¹²⁾ Steel is a notch-brittle material. The effect of a particular notch on tendency to constrain yielding will be discussed in later chapters.

Stresses, which are not accounted for in a stress analysis, but which nevertheless exist, are also important in determining brittle fracture strength. That residual stresses, for instance, can exert a profound influence on brittle fracture strength can be appreciated by recognizing that the stress intensity factor, K , is influenced by the presence of residual stresses in the vicinity of the crack. These residual stresses result from fabrication processes such as rolling and welding.

The condition of the material itself is of great importance in determining fracture strength. Mylonas⁽³⁸⁾ has demonstrated that plastic strain-history, by altering material properties, can influence fracture behavior markedly. It is also generally accepted that mill techniques, alloying, and heat treatment, both during the steel-making process and during structure fabrication, alter the material's tendency to fracture.

The discussion of factors which affect brittle fracture strength can be related to the fracture mechanics philosophy by accounting, in fracture mechanics language, for the effect of each factor. Thus, residual stresses become crack-extension forces, G , and metallurgical changes become adjustments in notch-toughness, G_c . This is not to say that the foregoing discussion and the concepts advanced by Figs. 1.5 and 1.6 are reconcilable in every detail with the techniques of fracture mechanics as presently constituted. There exists, currently, no such consensus on the solution of the fracture problem.

CHAPTER 2

OBJECT AND SCOPE OF THIS INVESTIGATION

The complexity of the brittle fracture phenomenon makes it imperative to segregate the various aspects of the problem. This chapter identifies the aspects of the brittle fracture problem with which the current investigation is concerned.

This study is primarily an experimental investigation, although the results of the experimentation are related to some of the theoretical formulations which are discussed in Chapter 1. Experimental results are also used as the basis for conclusions which are drawn regarding some of the causes of brittle fracture. Of the laboratory specimens discussed in Chapter 1, examination is confined to the notched and welded wide-plate test, with an emphasis on the effect of the so-called Wells notch on the fracture strength of such plates. The wide-plate tests occupy a singular role in the efforts to evaluate brittle fracture strength experimentally. It is rational to believe that the best simulation of service fracture conditions is provided by the wide-plate test. This confidence seems justified in view of wide-plate test behavior, which demonstrates significant correlation with that of structures which have failed in a brittle manner while in service. This correlation and the large amount of available wide-plate test data suggest that intensive study of the phenomenon of fracture in the wide-plate test may be fruitful.

A single chapter is devoted to gaining a perspective of some of the wide-plate test results, after which particular interest is centered on the fracture initiation propensity of the Wells-type notch, which is widely used as the stress-raiser in the wide-plate tests. An effort is made in this investigation to examine the possible causes, in terms of the stress environment in the vicinity of the notch, of the scatter exhibited in wide-plate test results. That scatter is great can be determined by noting the sizeable difference between the behavior of so-called identical specimens. This disparity of test results in twin specimens suggests the need to know more about the environment in the immediate vicinity of fracture initiation, as opposed to what can be termed the gross specimen environment. The local environment, at least from a stress point of view, is examined by the use of an epoxy model of the Wells notch. The model material exhibits birefringence, enabling experimental determination, by the photoelastic method, of the model stresses induced by a system of forces chosen to simulate those to which the wide-plate prototype is subjected. One chapter is devoted to outlining the principles of the method used, the model fabrication and testing procedure, and the test results. A separate chapter translates these results back to the wide-plate tests and to the general phenomenon of brittle fracture. The analysis emphasizes an evaluation of the flow and fracture characteristics of the Wells notch by utilizing a concept of constraint-factor similar to that discussed in Chapter 1 and illustrated in Fig. 1.5. Finally, the results of this investigation are summarized and conclusions are presented.

CHAPTER 3

NOTCHED AND WELDED WIDE-PLATE TESTS

3.1. Introduction

The importance of the welded wide-plate test in assessing brittle fracture strength has been outlined briefly in Chapter 1. The present chapter contains a description of a typical wide-plate test specimen and the test procedure used for these specimens. Representative test results obtained by various investigators are presented and discussed. Particular emphasis is focused on those specimens that had a fracture behavior suggesting a significant influence of the notch from which fracture initiated.

3.2. Wide-Plate Specimen

The notched and welded wide-plate specimen depicted in Fig. 3.1 is typical of that used by the major wide-plate investigations in England⁽²⁵⁾ and the United States.⁽³³⁾ The specimen consists of flat plate material, the thickness of which has usually ranged from $3/4$ to $1-1/2$ in., though one series of tests conducted by Wells utilized plates of 3-in. thickness.⁽²⁷⁾ A specimen is fabricated in two halves which are joined by a longitudinal full-penetration butt-weld along the entire length of the specimen. The width of the welded specimen has usually been 2 or 3 ft, although tests have been conducted on plates as narrow as 1 ft⁽⁴⁰⁾ and as wide as 6 ft⁽³⁹⁾. The length of the test specimens has varied somewhat, although generally the

length/width ratio has ranged between 1 and 2. The most important detail which the wide-plate specimens have in common is the stress-raiser from which fracture is initiated. Greene⁽²⁴⁾ first suggested a notch of a type similar to those used in the specimens which are treated in the present study. Wells⁽²⁵⁾ developed and successfully used the notch in its present form. It is referred to in this work as a Wells-type notch or a Wells notch.

Though notches can be placed after welding,⁽³³⁾ the notch shown in Fig. 3.1(b) is fabricated into the plate-halves prior to welding. Only specimens having this latter sequence of notch placement and welding are considered in the present study. Notching is accomplished with a circular-saw cut of constant depth from the beveled edge of the two plates. The two notched plates are then welded together into a specimen with two chevron-shaped notches, lying in the XZ plane, and located at specimen mid-length. Though the particular notch shown in Fig. 3.1(b) is for plates of 3/4-in. thickness, the essential features and proportions of the Wells notch are retained in plates of greater thickness. The overall view of the wide-plate specimen and the uniform tensile loading to which it is subjected are shown in Fig. 3.1(a).

3.3. Test Procedure

The wide-plate testing procedures employed by various investigators are similar in their essential features. The specimen generally is secured to the testing machine pull-heads by welding. The capacity of the machines most commonly used ranges from 600 000 lb to over

4 000 000 lb. Capability to cool the wide-plate specimen to low test temperatures is necessary. This has often been provided by open-top tanks secured to the sides of the specimen. The tanks are filled with coolant so that the specimen can be cooled to a uniformly low temperature. The temperature is generally measured with thermocouples. When the desired test temperature is reached, the specimen is loaded monotonically to failure at a load-rate selected to preclude fracture initiation strain-rate effects. Instrumentation is often provided which develops, automatically, a load-deformation curve for the specimen. Fractures are designated as either complete or two-staged, depending on whether the initial fracture propagates immediately through the entire plate or arrests and needs additional load to complete the failure. In the latter case, both initiation and re-initiation stresses are noted. Attention is given to the fracture appearance, since it provides an important indication of fracture mode, velocity of fracture, fracture stress, and general material toughness.

3.4. Selection of Representative Tests

The tests which are reported herein represent only a fraction of the tests which have been conducted on notched and welded wide-plates. They have been chosen to be illustrative of the fracture initiation behavior of the wide-plate specimens. This brief, but representative, consideration of wide-plate test data allows practical interpretation of the Wells notch stress analysis, the results of which are presented in Chapters 4 and 5. In order to circumvent the additional complexity which various thermal and mechanical treatments insert into the problem,

attention is confined to plates tested in the as-welded condition. This precludes present consideration of the effects of pre-heating, post-heating, thermal stress relief, strain aging, and mechanical stress relief. Six series of tests are considered, with the specimens within each series differing only in the temperature at which the fracture test is conducted. The difference between the various test series is primarily that of type of steel. There are also minor variations in plate geometry, including differences in plate thickness, width, and length. Two of the series have slight differences in the dimensions of the Wells-type notch from that used in the remaining four series. None of these differences occur, other than accidentally, among specimens of a given series. The slight variation in variables in the different series is of minor importance, because the comparisons that are drawn are based primarily upon the behavior of specimens within a particular series. Thus, the differences between the various series are not evaluated.

3.5. Presentation and Discussion of Test Results

Tests representing six variations in steel are reported. The dependent variable, fracture stress, is evaluated as a function of test temperature. The material properties of the six varieties of steel are given in Table 3.1. The six mild steels used exhibit yield points ranging from approximately 30 ksi to 40 ksi, with a range of temperatures of -49°F to $+83^{\circ}\text{F}$ for the 15 ft-lb level in the Charpy V-notch test. Examination of the chemical properties of the steels indicates a reasonably good control on carbon content for all, with the

possible exception of Series 5, in which the carbon content is on the order of 0.3%. The other chemical properties are also shown in Table 3.1. In the following discussion of these results particular attention is paid to comparisons that are drawn between the behavior of specimens which were fabricated so as to be identical.

Series 1. ⁽²⁵⁾ This series, the first of many conducted by Wells, utilized a material which was relatively poor in fracture resistance. The 1-in. thick steel plate was a semi-killed mild steel, exhibiting a temperature of 83°F for the 15 ft-lb energy absorption level in the Charpy V-notch test. The test results on eight as-welded specimens and a sketch of the specimen and notch detail are shown in Table 3.2. The high fracture susceptibility of this series can be seen in Fig. 3.2, which shows fracture stress* plotted against test temperature. A possible strength-temperature transition curve is sketched for these data. It is also possible that this transition curve could be shifted somewhat to the right. In either case, the difficulty of getting a permissible strength-temperature transition curve to fit the data perfectly is obvious. The six points in the lower left region of the curve, while somewhat scattered, are not inconsistent. It is difficult, however, to reconcile the respective behaviors demonstrated by specimens D and H. These specimens fractured at quite different stresses, with the further complication that the larger fracture stress is associated with the lower temperature. It is disparities such as

* For purposes of this investigation, the fracture initiation stress, whether it leads to complete fracture or to arrest, is the quantity considered. Thus, initiation stresses only are plotted in Figs. 3.2 through 3.8, though arrested fractures are differentiated from complete fractures with an arrow above the plotted point.

this which suggest the existence of slight, but very influential, uncontrollable differences in the specimens.

Series 2.⁽²⁶⁾ This material, designated by Wells as P steel, is a semi-killed mild steel, not unlike that of Series 1, although it exhibits somewhat more toughness. Seven tests are represented in this series. The results of these tests are shown in Table 3.3, with the fracture stress-test temperature relationships plotted in Fig. 3.3. The scatter exhibited by these data is not sufficient to cause great concern, although it will be recognized that the behavior of specimens 2 and 3, when compared with that of specimen 6, leaves something, consistency-wise, to be desired.

It is interesting to note that the wide-plate transition temperature is about 20°F lower in Series 2 than in Series 1, which is the same difference exhibited by the respective Charpy transition temperatures, as determined by the 15 ft-lb criterion.

Series 3.⁽²⁶⁾ This series represents tests conducted on specimens fabricated from Q steel, which is a semi-killed mild steel with a higher than ordinary manganese-to-carbon ratio. The Mn/C ratio in Series 3 was approximately 7.5, while in the mild steel used in Series 2 the ratio was 3.0. The additional manganese results in a somewhat tougher material, as indicated by the significant reduction in temperature for the 15 ft-lb level in the Charpy test. The results of the seven tests in this series are presented in Table 3.4 and the associated stress-temperature plot in Fig. 3.4. The scatter between the data and the assumed transition curve is not excessive, although the discrepancy between the behavior of specimens 7 and 8 and that of specimen 6 is apparent.

Illustrative of the fact that there is no one-to-one correspondence between the Charpy data and the wide-plate test data is the rather slight increased toughness exhibited in the wide-plate tests of Series 3 over that of Series 2, compared with the large difference in the corresponding Charpy transition values.

Series 4. ⁽²⁶⁾ Nine tests of specimens fabricated from fully-killed, grain-controlled, normalized mild steel comprise this series. The toughness of this material is indicated by the -49°F temperature required for the 15 ft-lb Charpy V-notch level. The test results, given in Table 3.5 and plotted in Fig. 3.5, give evidence of the most disconcerting discrepancy noted thus far. The strength transition temperature for eight of the specimens appears never to have been reached; that is, testing appears to have been conducted above the transition temperature. Specimen 6, however, tested in the middle part of the temperature range represented in the complete test series, exhibits extremely low fracture strength. It is disparities such as this, that cannot be assigned to scatter, which highlight the importance of determining fundamental causes of fracture initiation.

Series 5. ⁽³³⁾ Steel used in this series of three tests conforms to ASTM specification A212 Grade B (firebox quality). This mild steel, the properties of which are given in Table 3.1, exhibits intermediate toughness characteristics and is on the border line of being unwelded because of the relatively high carbon content. The data from these tests, shown in Table 3.6 and plotted in Fig. 3.6, are inconclusive as to fracture stress-temperature transition curve. What is clear, however, is the disparity between the results of the three tests.

Identical specimens 1-2 and 1-3 exhibit different fracture stresses, and specimen 1-1, tested at a higher temperature, exhibits the lowest fracture stress of the three specimens.

Series 6.⁽⁴⁰⁾ The final test series included herein comprises two parts, differentiated by the specimen width. All specimens in this series were fabricated from ABS-Class C ship-steel, which has a yield point of nearly 40 ksi at room temperature. The other properties of this relatively tough steel are tabulated in Table 3.1. Four tests in this series, denoted as Series 6(a), were conducted on 12-in. wide specimens. Other details associated with this specimen are depicted on the sketch accompanying Table 3.7, in which the test results are tabulated. Figure 3.7 is a plot of fracture stress versus test temperature for these data. It is noted that identical specimens WP-5 and WP-15 exhibit widely different fracture stresses, although this behavior is not irreconcilable if the infinitely steep stress-temperature transition curve is used.

The remaining tests of this series, denoted as Series 6(b), were conducted on specimens of 24-in. width. The test results are listed in Table 3.8 and the associated stress-temperature plot is given in Fig. 3.8. If the test point representing specimen WP-24 is excluded from the plot, it appears that testing is being conducted on the lower leg of the strength-temperature transition curve, not having reached a high enough temperature to produce high stress fractures. Specimen WP-24 does not honor this conclusion, however, exhibiting a fracture stress approximately 13 ksi above that of the other specimens, even though tested at some 50°F below the temperature of WP-27. It must be admitted

that the disparity between specimen WP-24 and its twin, specimen WP-26, is not completely irreconcilable, inasmuch as neither would be considered to be a truly ductile or high stress fracture. Still, it would seem that the disparity between these two specimens, and indeed between WP-24 and the three specimens WP-26, WP-27, and WP-25, cannot be attributed solely to scatter.

The brittle fracture phenomenon, while known to exhibit considerable scatter in test data, cannot be assumed to exhibit, without reason, the irreconcilable diversity of behavior that has been shown to exist in some of the tests which have been reported in this section. The possible causes of this disparity are pursued in subsequent chapters.

CHAPTER 4

PHOTOELASTIC STRESS ANALYSIS OF WELLS NOTCH

4.1. Introduction

The brittle fracture of notched and welded plates, reported in Chapter 3, suggests the need to know more about the flow and fracture characteristics of specimens with the Wells-type notch (Fig. 3.1). A valid stress analysis of the vicinity of fracture initiation is a prerequisite for determining these characteristics. An elastic solution, utilizing the usual assumptions of isotropy and homogeneity, affords a useful approximation of the effect of the applied load in the wide-plate test because of the low nominal applied stresses often associated with fracture. This is not to suggest that there is no yielding of the material in the vicinity of the notch; however, with the low-stress fractures there is no gross yielding.

A valid theoretical stress analysis in the vicinity of the Wells notch cannot presume either plane-stress or plane-strain. Plane-stress provides an accurate description of the state of stress in an unnotched plate, or in regions distant from the vicinity of the notch in the notched plate, while plane-strain represents a limiting state in the vicinity of the notch. The abruptness of the geometrical discontinuity in the Wells notch poses additional difficulties in the formulation of a valid theoretical solution.

The advisability of using an experimental stress analysis is suggested by the difficulty of establishing a theoretical analysis.

The method used must allow determination of internal stresses, since fracture initiation may be most likely to occur at plate mid-thickness. Strain gauge and two-dimensional photoelastic techniques lack the capacity to determine an internal stress-state. The three-dimensional photoelastic "frozen stress" technique, which does allow determination of internal stresses, is used in this investigation. The principles governing the valid application of three-dimensional photoelasticity, the model details, the test procedure, a description of the model slices examined, and the results of the analysis are presented in subsequent sections of this chapter.

4.2. Theory of Three-Dimensional Photoelasticity

Many light-transmitting materials exhibit stress-birefringence, by which the light transmission characteristics of the material are uniquely affected by the stresses. The laws governing this stress-optical relationship are presented in Appendix A. One of the most useful stress-optical laws can be expressed as

$$\sigma_i - \sigma_j = \frac{N_k \cdot F}{t_k} \quad (4.1)$$

where i, j, k = mutually orthogonal coordinate axes

σ_i, σ_j = principal stresses

N_k = fringe-order for light transmitted in k direction

t_k = thickness of material through which light is transmitted

F = material optical property, constant for light of a given wave length.

Further details of the basis of this relationship are contained in Appendix A.1.

Equation (4.1) obviously can be used for cases of plane-stress in which the loading is acting on the model during the evaluation of fringe-order, N . This two-dimensional analysis lacks sufficient generality to be useful for appraising stresses in the vicinity of the Wells notch. Fortunately, it is possible to "fix" or "freeze" stresses into a material so that Eq. (4.1) can be applied to an unloaded material which will behave, optically, as if it were loaded. (41,42) Furthermore, careful slicing of the model will not disturb the optical characteristics. Thus, internal stress-states can be examined and evaluated.

The mechanism by which stresses are "frozen" into a material is illustrated in Fig. 4.1. (42) The model material is assumed to consist of two quite different components, an elastic primary phase, P , surrounded by a viscous secondary phase, S . The stiffness of the primary phase is not much affected by temperature changes, while the secondary phase exhibits stiffness that varies from a high value at low temperatures to zero at a certain critical temperature, termed T_c . Optically, from the standpoint of birefringence, the primary phase is much more sensitive than the secondary phase. In terms of Eq. (4.1), $F_p \ll F_s$, where subscripts p and s refer to primary and secondary phases, respectively. Figure 4.1(a) shows the unloaded, unheated model. In Fig. 4.1(b) the tensile load, $R = R_p + R_s$, has been added and is shared, in a manner dependent on the amount of each component phase, as well as on the component unit stiffnesses. The model elongation, Δ_l ,

is a function of the combined stiffnesses, K_p and K_s , for the temperature involved. The conditions of stress and deformation associated with temperatures greater than the critical temperature are depicted in Fig. 4.1(c). The secondary phase has lost its stiffness and the entire load is carried by the primary phase, thereby causing a large additional elongation, Δ_2 . The temperature cycle is now reversed and the model is cooled (Fig. 4.1(d)). The secondary matrix regains its stiffness, but remains in its elongated unstressed state with the load still carried by the primary phase. Upon cooling to ambient temperature, the load is removed as shown in Fig. 4.1(e). The recoverable elongation will not be greatly different from Δ_1 and the stress in the primary system will not be greatly reduced, being held in equilibrium at high stress by the much stiffer secondary phase. Optically, the sensitive primary phase is much more influential than the insensitive secondary phase. Thus, Eq. (4.1) can be applied to the unloaded "frozen" model, or a slice thereof, as if it were loaded.

The successful use of the two-phase model in explaining the frozen stress mechanism is not accidental. The material used for photoelastic analysis of three-dimensional stress-states has a complex polymer primary network immersed in a fusible phase. It is essentially a spring of low modulus embedded in a viscous matrix. ⁽⁴¹⁾

The results of stress-freezing are illustrated in Fig. 4.2 in which a fringe photograph of the constant-moment region of a calibration beam specimen into which stresses have been fixed is shown. The procedure by which the calibration specimen is utilized to determine the optical material constant, F , is presented in section 4.3.

4.3. Epoxy Model of the Wells Notch: Design, Fabrication, and Loading

The wide-plate specimen (Fig. 3.1) with the Wells-type notch is the prototype for the model which is discussed in this section. The stresses of most interest are those in the immediate vicinity of the notch. The equipment used to fix the stresses limits the total size of the model. Thus, to magnify the sensitivity of the model in the notch vicinity, only a small region surrounding the Wells notch is modeled. For the scale chosen, four units of length on the model represent one unit of length on the prototype. Thus, the 0.75-in. prototype plate thickness becomes a 3.0-in. thickness in the model. This scale, though somewhat arbitrary, is considered to be sensitive enough to allow accurate determination of stresses in the vicinity of the Wells notch.

The material used in the model was an epoxy polymer described by Leven.⁽⁴³⁾ This is a two-component epoxy which is made by combining 50 parts, by weight, of liquid catalyst (phthalic anhydride) with 100 parts of liquid epoxy (Araldite 6020). These components, mixed properly and cycled thermally, set into a hard translucent material which exhibits birefringence when stressed.

The model was machined in three parts (Fig. 4.3) from a carefully selected casting. Two of the three parts are identical and represent the plates of the prototype. The third part fits between the two plate components and corresponds to the weld in the prototype. The notching operation was accomplished in a manner similar to that used for the prototype. The notches were placed in the individual plate components with a saw-cut of constant depth from the beveled edge. The

circular-saw blade used for the epoxy model was 0.028 in. thick and corresponded to the 0.007-in. thick circular-saw blade used in the prototype. This notching operation was performed prior to joining the two beveled plate components to the center weld component. The gluing of the three components followed the notch preparation and was accomplished with an epoxy mixture not unlike the parent material.

A uniformly-distributed tensile load was applied to the ends of the completed model, as shown in Fig. 4.4. Whipple-tree mechanisms distributed the total load uniformly to eight equally-spaced loading points on the model ends. The model length of 10 in. was chosen to avoid end effects in the vicinity of the notch. The nominal stress acting on the gross section of the model was 12.1 psi, while the net stress acting on the plane defined by $Y = 0$ was equal to 14.2 psi. The total net tensile load on the model was 436 lb.

For the stress-freezing operation, the loaded model was placed in a large oven equipped with a thermostatic control which provided a constant rate of temperature increase. A rate of temperature increase of approximately 2°C per hour for the heating cycle and a rate of decrease of approximately 1°C for the cooling cycle were maintained. The gradual heating and cooling were necessary in order to prevent the development of unwanted thermal stresses. Upon completion of the thermal cycle, the model was unloaded in preparation for slicing.

The machining of all specimens for which stresses were to be determined was conducted so as to preserve the frozen stress pattern. Regions containing wanted slices were cut from the entire model with a band saw. Sufficient waste material was allowed in order to keep the temperature in the final slice region from rising appreciably. The

final slice dimensions were reached by successive milling in a vertical mill equipped with a fly-cutter. The final four mill cuts, from first to last, were 0.010, 0.005, 0.003, and 0.002 in. High cutter speeds, coupled with low table feed rates, were used to keep surface temperature and pressure low.

The small calibration beam specimen was subjected to the same thermal cycle as was the model so that the material constant, F , could be determined for use in stress computations for the notched model. The beam was machined from material taken from the same casting as that used to fabricate the model. The stresses in the beam, subjected to a constant moment in its central region, are assumed to be given by the flexure formula, $\sigma = \frac{My}{I}$. The stress so computed becomes the left term, $\sigma_i - \sigma_j$, in Eq. (4.1). Referenced to the diagram in Fig. 4.5, the subscripts i , j , and k become x , y , and z , respectively. The transverse normal stress, σ_y , is assumed to be zero. Equation (4.1), written with the material constant, F , as the dependent variable, becomes

$$F = \frac{(\sigma_y - \sigma_x)t_z}{N_z} = \frac{My \cdot t_z}{IN_z} \quad (4.2)$$

Values of F for a particular distance, y , from the neutral axis can be computed by measuring the associated fringe-order, N_z . Several measurements of N_z , for various values of y , allow a least square averaging of the individual determinations of F . Thus, the average value of F was found to be 2.6 lb/in.-fringe (Fig. 4.5).

Extreme care was exercised, subsequent to freezing of the stresses into the model, to alleviate the development, with time, of

extraneous edge stress. This effort included keeping individual model slices and larger unsliced components in a dessicator so that the slice boundaries would not absorb moisture.

4.4. Isochromatic Fringe Photographs of Selected Model Slices

Several large-field fringe photographs have been taken of selected portions of the epoxy model. These photographs give a visual representation of lines of constant principal stress-difference (isochromatics), whereby the regions of maximum stress gradient can be deduced and approximate values of maximum principal stress-difference inferred.

A lens-type transmission polariscope with an 8-in. diameter field was utilized to obtain the fringe photographs. A mercury-arc lamp provided an essentially monochromatic light source. Circularly-polarized light, obtained by adding quarter-wave plates to the polarizer and analyzer elements of a plane-polariscope, was used to suppress the isoclinic fringes from the photographs. A camera with a lens of long focal length and an 8 in. x 10 in. film holder was used to take the pictures. The portion of the model to be photographed was placed in an immersion tank filled with halowax oil to render a sharper fringe distinction. The immersion tank was equipped with partial mirrors by which light could be passed through the model slice several times by a process of successive reflections and refractions. Using this accessory, the isochromatic fringe patterns resulting from multiple light passages through the model were photographed. This technique increases the number of fringes and is known as fringe-multiplication.⁽⁴⁴⁾

The photograph shown in Fig. 4.6 shows the isochromatic fringe pattern resulting from circularly-polarized light passing once through the entire model thickness. Although Eq. (4.1) can be applied to this fringe pattern, the results would be of no practical import since the principal stress-differences so obtained would be only averages through the large thickness. However, Fig. 4.6 does contain useful information. The symmetry of the frozen stress pattern in the vicinity of the notch is readily evident. Gross dissymmetry of stress would be very obvious in this photograph because of the large thickness through which the light was passed. It is also relevant to note that excellent definition of high-order fringes is obtained in this photograph, inasmuch as the nominal applied stress fringe-order is approximately 15. A final important conclusion that can be drawn from examination of Fig. 4.6 is that the glued joints transmit fringes, apparently unaltered and intact, from the side plate components. This is evident from the continuity of the isochromatic fringes across the joint. Confirmation of the integrity of the joint lends credibility to the assumption that the prototype weld region can be simulated by the center component of the model.

Two plane slices, the faces of which approach principal-plane conditions, were cut from the model. One of these slices was taken from the model surface. The second slice was taken at model mid-thickness. Both slices were 0.125 in. thick and 8 in. high, and had a width extending from one edge of the model to $1/16$ in. beyond the model center line. Isochromatic fringe photographs of these two slices and their orientation in the model are shown in Figs. 4.7 through 4.11.

The isochromatic fringe photographs of the surface slice of the model are shown in Figs. 4.7, 4.8, and 4.9, for light passing through the slice thickness 3, 5, and 7 times, respectively. The application of Eq. (4.1) to these cases requires the multiplication of the actual slice thickness by the number of passages of light through it. Hence, the fringe-order is directly related to the amount of fringe-multiplication. It can be observed from the photographs that additional fringe-order is obtained by the fringe-multiplication technique at the expense of fringe distinctness. It is observed that both ends of the notch-slit exhibit a sizeable stress concentration, although the concentration on the "weld" side of the notch-slit is apparently significantly greater than that on the plate side. The validity of this observation is confirmed and discussed in section 4.6.

Figures 4.10 and 4.11 represent isochromatic fringe photographs of the slice taken from the mid-thickness of the model. The overall slice dimensions conform to those of the surface slice previously discussed. The fringe-multiplication technique was applied to obtain isochromatic fringe photographs of this slice. The photograph of Fig. 4.10 resulted from using a fringe multiplication of 3, while the photograph of Fig. 4.11 was obtained by using a fringe multiplication of 5. It is noted that both ends of the notch-slit produce a large stress concentration. The full stress concentrating power of the tip of the Wells notch is not shown in these photographs, since, at the notch, the thickness of the material through which the light passes decreases from the basic slice thickness to zero. Hence, fringe-orders do not "keep pace" with stresses in this region. Subsequently presented

material contains a more precise evaluation of the stress concentration at the tip of the notch.

4.5. Determination of the von Mises Equivalent Yield Stress

The correct appraisal of the flow characteristics of the material in the vicinity of the Wells notch requires a valid stress analysis and a correct yield criterion linking the stresses to the propensity of the material to flow. Photoelastic appraisal of the frozen stresses in the epoxy model is assumed to provide a correct stress analysis. The selection of a yield criterion is usually made between two classical theories. The Tresca criterion postulates that material flow will impend when the maximum shear stress reaches a certain value, which can be defined as a material property. This criterion, then, presumes that the likelihood of yielding is appraisable upon determination of the maximum and minimum principal stresses acting at a point, without regard for the intermediate principal stress. The von Mises criterion, on the other hand, postulates that flow is tied to the shear-distortion strain energy and that yielding will occur when this energy reaches a certain magnitude. The von Mises hypothesis can also be expressed in terms of the principal stresses by defining an equivalent yield stress, σ_e , as follows

$$2\sigma_e^2 = (\sigma_1 - \sigma_2)^2 + (\sigma_2 - \sigma_3)^2 + (\sigma_3 - \sigma_1)^2 \quad (4.3)$$

The von Mises equivalent stress, σ_e , can be considered representative of the yielding power of a particular stress-state. The occurrence of

yielding is signalled when the equivalent von Mises stress, computed from Eq. (4.3), attains a value equal to the material's conventional yield strength measured in the uniaxial tensile test (Appendix A.2). The von Mises criterion is presumed in this investigation.

The similarity between Eqs. (4.3) and (4.1) suggests that the von Mises equivalent stress might be determined by photoelastic measurements. Brock⁽⁴⁵⁾ has developed the relationships linking Eqs. (4.1) and (4.3) (Appendix A.2). The resulting equation of most interest is

$$\sigma_e^2 = \left(\frac{F}{2t}\right)^2 [N_x^2(2 + \sin^2 2\theta_x) + N_y^2(2 + \sin^2 2\theta_y) + N_z^2(2 + \sin^2 2\theta_z)] \quad (4.4)$$

where F = material stress-optical constant

t = thickness of medium through which light is transmitted

N_x, N_y, N_z = fringe-orders for light transmission in X, Y, Z directions

$\theta_x, \theta_y, \theta_z$ = isoclinic parameters for light transmitted in X, Y, Z directions.

The quantities on the right side of Eq. (4.4) are measurements associated with small cubes cut from epoxy models into which stresses have been frozen. These quantities can be measured directly from the cube without having additional knowledge of the stress environment surrounding the cube. The fringe-orders are the retardation measurements, according to Eq. (4.1), for the mutually orthogonal, but otherwise arbitrary, coordinate directions, X, Y, and Z. The angles $\theta_x, \theta_y, \theta_z$, are the respective isoclinic parameters for these three coordinate directions. The details of development of this equation are contained in Appendix A.2.

A polarizing microscope⁽⁴⁶⁾ was utilized to make the photoelastic determinations of the fringe-orders and the isoclinic parameters. The microscope consists of the usual microscope components, supplemented by polarizing elements designed and located so as to produce polarized light by which the photoelastic parameters can be appraised. A photograph of the instrument used is shown in Fig. 4.12. A noteworthy feature of this instrument is the compensator,^{*} which can be introduced in the optical path between the model and the analyzer element.⁽⁴⁶⁾ The compensator has the capability of introducing a variable, but measurable, amount of birefringence into the optical path. Inserting compensator birefringence equal in magnitude, but opposite in sense, to that of the model, renders the total relative retardation of the model-compensator system zero. Since the zero retardation condition is distinguishable, the compensator reading can be related directly to the model retardation. The isoclinic parameters are measured, as in an ordinary polariscope, by obtaining light extinction with the model's principal-stress axes oriented coincidentally with the polarizer-analyzer axes.

The measurement of the von Mises equivalent stress has been confined to cubes whose centers lie in the plane defined by $Y = 0$. The Wells notch also lies in this plane; hence, these measurements will obviously be of most interest from the standpoint of fracture initiation. Figure 4.13 shows the size and location of the cubes which were located at mid-thickness and at the surface of the model. In regions away from

* Compensators of both the Babinet- and Berek-type design were used in this investigation.

the notch, where low stress gradients pertain, the cubes were 0.25 in. on a side. In the vicinity of the notch, the cubes were reduced to 0.125 in. on a side in order to obtain a better indication of the higher stress gradients. Also shown in Fig. 4.13 is the von Mises equivalent stress, σ_e , normalized with respect to the gross nominal axis stress, σ_{y-nom} , plotted against the distance from the specimen center line. The measurements associated with cubes taken from the surface of the model show an expected tendency to hover around 1.0 until the notch is approached. As the notch is approached, the von Mises equivalent stress rises sharply. The method by which the stress analysis of the material adjacent to the notch face was conducted is discussed in section 4.6.

The von Mises equivalent stress measurements associated with cubes cut from the mid-thickness of the model coincide closely with those of the surface cubes in regions distant from the notch vicinity. As the quarter-width of the model is approached, however, the value of the von Mises equivalent stress decreases, to a minimum approximately 2 in. from the model mid-width. From this minimum, occurring approximately 1 in. from the tip of the notch, the von Mises equivalent yield stress rises sharply to a maximum value at the free surface represented by the notch-tip.

Figure 4.14 shows the results of measurements on additional small cubes taken from the periphery of the Wells notch. It can be noted that there is a mild reduction of the von Mises equivalent stress in the region between the model surface and the plate mid-thickness along either of the peripheral boundaries of the Wells notch. It must be

understood that these measurements do not represent the von Mises stress, σ_e , at the notch face, but rather an average σ_e through the cube. Details concerning the evaluation of the notch-boundary stress are presented in section 4.6.

4.6. Determination of Maximum Normal Stress on Notch Boundary

The determination of the stress tensor components at a general point in a three-dimensional photoelastic model is not as easily accomplished as is the direct calculation of the von Mises equivalent stress from Eq. (4.4). The reason for this fundamental difference in difficulty between determining the von Mises stress and the individual stress components is due to the fact that it is impossible, from conventional photoelastic measurements, to differentiate between a given stress-state and the same stress-state to which a hydrostatic tension or compression is superimposed. Thus, the possibility of determining the individual stress components at a point, by direct photoelastic measurements only, is precluded. The inability to differentiate, by photoelastic means, the two stress-states does not impose the same limitation on the determination of the von Mises equivalent stress, since the addition of an arbitrary hydrostatic tension or compression has no effect on the propensity to yield, as measured by the von Mises criterion. Stress-separation on the model interior can be effected, utilizing photoelastic data, by a numerical integration of the governing differential equations of equilibrium.⁽⁴⁷⁾ This procedure, while being quite general, is not noted for its accuracy, especially in regions which have a high stress gradient. Stress-separation

is facilitated at unloaded model boundaries by the absence of shear and normal stresses. Fortunately, the stresses of most interest generally occur at such boundaries. In the case of the model of the Wells notch (Fig. 4.4), large stresses develop around the perimeter of the machined notch. Some stress measurements from the entire notch boundary are reported in this section, although the major effort is devoted to four regions of the notch-model interface (Fig. 4.15). All regions are in the plane of the notch defined by $Y = 0$.

One region for which stresses are reported is at the sharp tip of the Wells notch occurring at plate mid-thickness. A second region of interest is the "flat" or "land" at the interface between the side components and the centerpiece of the model. The third and fourth regions of particular interest are the junctions between the notch boundaries and the plate surface. One is in the "weld" material and has an acute junction angle, while the other is in the side plate components and has an obtuse junction angle.

To obtain the stress at the tip of the notch, the mid-thickness slice, for which isochromatic fringe photographs are shown in Figs. 4.10 and 4.11, was used. The portion of the slice in the notch-tip vicinity was cut from the main slice and placed in an immersion cell filled with halowax oil, which had an index of refraction matching that of the epoxy material. The immersed slice was analyzed with the polarizing microscope equipped with the Berek compensator, which has been described in section 4.5.

The first data from this slice was obtained with polarized light transmitted through the slice in the Z direction of the model. A mechanical stage on the microscope provided capability to traverse

the slice in the X direction. Relative retardation measurements were taken as the slice was traversed toward the notch-tip. These measurements, in general, represent a secondary principal stress-difference, termed $\sigma_{1z} - \sigma_{3z}$, where the second subscript, z, refers to the direction of the light transmission. However, as the notch-tip is approached this stress-difference approaches the value of the normal stress, σ_y , at the notch-tip. The retardation measurements for the light passing through the decreased thickness of material at the notch-tip were converted to stresses by Eq. (4.1), thus accounting for the reduced thickness of the medium through which the light was transmitted. Results of these measurements, expressed as a stress concentration, are plotted in Fig. 4.16, wherein the notch-tip stress is estimated by extrapolation. The data near the notch-tip exhibits some scatter, which makes it difficult to establish the notch-tip stress precisely. Neglect of the data point nearest the notch-tip allows an extrapolation, consistent with the remaining data, which yields a notch-tip stress concentration of approximately 12. The likelihood of an error in the stress determined for the neglected data point is relatively great, since the small thickness of material through which light is transmitted is not measured, but is calculated from the assumed notch geometry. The thickness so-calculated can be significantly in error, particularly on a percentage-of-real-thickness basis. In addition, the effect of time-edge-stress would be to produce an apparent stress-difference of lower magnitude than actually exists.

The results of retardation measurements of polarized light transmitted in the X direction through the slice containing the notch-tip are shown in Fig. 4.17. The stress difference, $\sigma_{1x} - \sigma_{3x}$,

non-dimensionalized with respect to the nominal gross-section applied stress, is shown as a function of the specimen thickness through which light was transmitted. The specimen thickness, t_x , was reduced successively toward the notch-tip. Thus, the value of stress-difference, extrapolated to the notch-tip, represents the actual notch-tip principal stress, σ_y . The consistency of the data in Fig. 4.17 is evident. The order of magnitude of the notch-tip stress concentration, so-determined, is in good agreement with the range of possible concentrations implied by the data of Fig. 4.16. However, the data of Fig. 4.17 imply possible notch-tip stress concentrations within the range 1.3 ± 1 , which is a much narrower range than can be specified from Fig. 4.16.

Photoelastic measurement of stresses in the vicinity of the flat near the interface between the side plate components and the center section (Fig. 4.15) was carried out in a manner similar to that used for the notch-tip. The normal stress in the thickness direction was again eliminated from the photoelastic measurements by passing the light through the slice in the Z direction. Three small subslices were taken in this region (Fig. 4.18) and provide three separate sets of retardation data for microscope traverses of the specimens in the X direction. The data for these three sets of measurements are very consistent, as shown in Fig. 4.18. The maximum stress concentration is seen to be of the order of 5. The stress-difference gradient is extremely high, as evidenced by the transition from a stress concentration of approximately 2 to the interface-concentration of 5 in an X distance of 0.030 in. This corresponds to a prototype X distance of 0.0075 in.

The areas in the vicinity of the notch, as it emerges to the surface of the model, are the regions in which the final detailed stress investigation was made. These areas are denoted as regions 3 and 4 in Fig. 4.15 and are located at the ends of the notch-slit. Identical methods were used to investigate these two regions; hence, they are discussed together. The initial size of the segments on which the analysis was conducted is shown by the dotted outline in Fig. 4.15. Additional orthogonal axes, X' and Z' , are defined, as shown in Fig. 4.15, such that the Z' axis is parallel to the internal boundary of the machined notch.

The analysis of the specimens from regions 3 and 4 was conducted in a manner which produced a reliable estimate of the stress at the junction of the notch with the specimen's surface. No attempt was made to determine precisely the stresses in other regions of the segment. Two separate procedures, which allow somewhat independent checks to be made on the maximum stresses so-determined, were followed in the stress evaluation of these points. The first of these procedures is similar to that used in the analysis of regions 1 and 2 previously reported in this section. That is, polarized light was passed through the slice in a direction parallel to a known principal stress, thus eliminating that stress from the relative retardation. It can be seen from Fig. 4.15 that the Z' direction fulfills this requirement as the notch interface is approached. Thus, traverses of the specimen on the polarizing microscope stage in the X' direction, while light is transmitted in the Z' direction, allow evaluations of the principal stress-difference, which tends toward the value of the

individual normal stress, σ_y , as the notch interface is approached. One additional refinement was made because of the size of the initial specimen. The thickness of the segment in the Z (or Z') direction was successively reduced by machining after relative retardation measurements were made for the preceding thickness. This permitted an evaluation of the stresses at the notch-model interface as the model surface was approached.

The results of the stress measurements for region 3 are plotted in Fig. 4.19, in which each symbol represents retardation measurements taken for a constant thickness in the Z' direction. These measurements present a very consistent picture and give evidence of a stress concentration at the junction of the notch-model interface and the model surface of the order of 6. It can be noted in this figure that the distribution of principal stress-difference, $\sigma_{1Z'} - \sigma_{3Z'}$, through the thickness (Z' direction) seems to be rather uniform, inasmuch as the stress readings taken for one thickness coincide essentially with readings taken for all other thicknesses.

The corresponding plot for region 4, the obtuse notch-surface junction, is shown in Fig. 4.20. It is seen that there are two types of stress-difference gradient as the notch surface is approached. The first, for large specimen thickness in the Z' direction, is like that represented in Fig. 4.19 for region 3. The second, for light passing through thicknesses smaller than 0.200 in., indicates a nearly flat stress-difference gradient as the X' traverse is made. It is significant to note that the extrapolations from either set of data yield approximately the same maximum stress concentration of 2.5 at the model surface.

Another set of retardation measurements was made on the specimens from regions 3 and 4 by passing light through the specimens parallel to the model surface, that is, in the X direction. This, coupled with successive slicing of the specimen in the X' direction, allowed determination of the secondary principal stress-difference for various specimen thicknesses as a function of distance from the model surface. This corresponds to a specimen traverse in the Z direction. Plots of stress-difference, $\sigma_{1X} - \sigma_{3X}$, versus distance from the model surface, with specimen thickness, t_x , represented parametrically, are shown in Fig. 4.21 for the region 3 specimen and in Fig. 4.22 for the region 4 specimen. Included in these plots are extrapolations, to the model surface, of the data representing a single specimen thickness. Figure 4.23 represents these surface values of stress-difference as ordinates plotted against abscissa values of specimen thickness in the X direction. Extrapolation of these data to zero specimen thickness gives the normal stress, σ_y , at the junction of the notch with the model surface. The correlation between the stresses so-determined and the stresses evaluated by the transmission of light in the Z' direction is excellent. Thus both measurement methods indicate stress concentration of the order of 6 and 2.5 in regions 3 and 4 respectively. It is emphasized that the plots of stress concentration in Figs. 4.19 to 4.23 are proportional to the average principal stress-difference through the thickness in question. This becomes an individual normal stress component, σ_y , as the material thickness approaches zero at a stress-free boundary.

The futility of using surface strain gauges to determine accurately the maximum stress concentrations in region 3 is evident by reference to Fig. 4.19. A 1/32-in. (.0312 in.) strain gauge placed adjacent to the notch would average the stress in the material having a stress concentration ranging from approximately 1 to more than 6. It is of interest to note that 1/32-in. strain gauges placed in regions 3 and 4 on the surface of prototype plates (Fig. 3.1) yielded stress concentrations of approximately 3 and 2, respectively, thus confirming the relative magnitudes as well as the expected averaging effect. (40)

To check the order of magnitude of stresses in portions of the notch perimeter other than those of regions 1, 2, 3, and 4, spot checks were made on the specimens, which had been used in the determination of the von Mises equivalent stress, around the perimeter of the notch. These specimens, previously discussed, are shown in Fig. 4.14. Light was transmitted in the Z' direction and as close to the notch-model interface as possible. To the extent that these ideal conditions are met, this procedure gives the value of the normal stress, σ_y , directly. Stress concentrations so-determined, together with the values determined previously for regions 1, 2, 3, and 4, are shown in Fig. 4.24. The values determined from the single reading test cannot be treated with the same confidence as those determined in regions 1, 2, 3, and 4 where more measurements were made. Still, it is noted from Fig. 4.24 that there are no irreconcilable discrepancies in the data presented.

CHAPTER 5

FLOW AND FRACTURE IN THE PROTOTYPE NOTCHED PLATE

5.1. Introduction

The purpose of this chapter is to relate the results of the photoelastic stress analysis of the epoxy model to the data from the prototype notched and welded wide-plate tests. Information from Chapter 1 is utilized in this effort, with special emphasis on section 1.4, which outlines the factors that affect brittle fracture, including the concept of notch-brittleness presented in Fig. 1.5. The degree to which the epoxy model simulates, or fails to simulate, the conditions associated with the wide-plate test is initially discussed. An assessment is made, if only qualitatively, of the fracture-related conditions in the wide-plate tests which are not adequately modeled by the photoelastic specimen.

5.2. Degree of Simulation of the Prototype by the Epoxy Model

Some aspects of similarity between the epoxy model and the prototype have previously been alluded to. It has been mentioned (Chapter 4) that the isochromatic fringe photograph (Fig. 4.6) of the entire epoxy model verifies the high degree of structural integrity of the glued joint between the side plate components and the center "weld" component. Isotropy and homogeneity of both the model and the prototype have also been assumed. Inasmuch as an elastic analysis has been conducted, the material modulus does not need to be identical in the model and prototype.

On the other hand, Poisson's ratio, while of no consequence in the analysis of stresses for the case of plane-stress, does affect the analysis for the case of plane-strain. The stress-state in the vicinity of the notch approaches that of plane-strain, while that of plane-stress pertains at points distant from the notch. Poisson's ratio for the epoxy model material is known to be somewhat greater than that for steel. As a result, somewhat larger normal stress, σ_z , through the thickness can be expected to develop in the model than that which exists in the prototype specimen. However, it is thought that the difference between the model and prototype stress-state is small.

The size of the model was necessarily limited to a region corresponding to the vicinity of the notch in the wide-plate specimen. Hence, the question arises as to whether the model adequately simulates the stress-state in the wide-plate test. More specifically, is the model wide enough to provide sufficient material upon which the transverse normal stress component, σ_x , developed as a consequence of the notch, can be supported? Examination of transverse normal stress distributions obtained by Neuber⁽⁴⁸⁾ for similarly loaded elements having somewhat similar notches indicates that there is some transverse normal stress in the prototype plate at the width which marks the edge of the model. This stress represents a relatively small fraction of the maximum transverse normal stress which develops within the region represented by the model. Thus, the absence of the σ_x stress at the model edge is not thought to jeopardize the valid use of the model to simulate the primary conditions of the prototype.

The uniform tensile loading to which the model was subjected simulates the applied loads in the low-temperature fracture tests of notched and welded wide-plate specimens. This model loading does not account for the forces, and resultant stresses, to which the wide-plate is subjected as a result of the welding operation. However, the results of the stress analysis are useful to assess, qualitatively, the effect of the weld on the notch stress, since the differential strains associated with the weld thermal cycle leave an essentially tensile residual stress in the longitudinal direction in the vicinity of the notch.

Attention is confined, in the epoxy model, to the elastic stress distribution, whereas it is generally accepted that some inelastic deformations precede and accompany all fractures in the wide-plate tests.⁽¹¹⁾ In translating the model strain concentrations to the wide-plate prototype, order-of-magnitude correspondence between inelastic strains and those predicted assuming complete elasticity is expected. The stress concentration follows the strain concentration except when yielding intervenes. Determining the final stress-state, then, will depend on knowing the strains and the stress-strain relationship of the material in question. In summary, the epoxy model study provides useful information on strain concentrations for both the elastic and inelastic range of loading, while the significant stress determinations of the model are confined to the elastic loading range.

5.3. Maximum Normal Stress and von Mises Equivalent Yield Stress at Specimen Mid-Thickness

The flow and fracture characteristics of specimens in which the Wells notch is employed as the fracture initiator are expressible in terms of the von Mises equivalent stress and the maximum normal stress, respectively. This section examines the distribution of these two stress components at the specimen mid-thickness in the plane in which the notch lies, that is, the plane defined by $Y = 0$.

Determination of the maximum normal stress distribution is based on photoelastic measurements described in Chapter 4, on available theoretical solutions for similar specimens, and on experience. The points for which it is possible to accomplish direct stress-separation by utilizing only photoelastic data are located at free boundaries of the specimen. Three such boundaries occur in the region in question, one at the epoxy model edge, a second at the notch-tip, and a third at the notch-flat opposite the notch-tip. The respective stress concentrations for these regions were found to be 1, 13, and 5. The directly-determined notch-tip maximum normal stress is plotted as a data point in Fig. 5.1 which shows the maximum normal stress, normalized with respect to the nominal applied stress, plotted against the distance from the notch-tip. The dashed portions of the plot represent the approximate stress distribution across the specimen width. The chosen distribution was influenced by Neuber's⁽⁴⁸⁾ and Westergaard's⁽¹⁹⁾ theoretical stress analyses of a similarly-loaded flat plate containing an elliptically-shaped, plane-front crack. The choice of the normal stress distribution curve has also been partially influenced by

experience and reason. The choice of a stress gradient from the tip of the notch to where the stress distribution approaches nominal conditions is most susceptible to error in determining the approximate stress distribution. While this gradient could conceivably vary considerably from that shown in Fig. 5.1, the exact gradient would not provide a basically different argument from the one presented with the assumed stress distribution.

The von Mises equivalent yield stress, σ_e , normalized with respect to nominal applied stress, is also shown in Fig. 5.1. This stress was determined in every case from Eq. (4.4) for which evaluation of fringe-orders and isoclinic parameters was accomplished by photoelasticity, as described in Chapter 4. This plot is a partial reproduction of that shown in Fig. 4.13. While the region of high stress gradient near the crack-tip could have stresses somewhat different from those implied by the curve, small variations in the distribution in this region do not negate the basic conclusions which are drawn regarding these data.

Fracture initiation can be thought, at least in broad terms, to be related to the maximum normal stress, σ_1 , while the occurrence of yielding is governed by the magnitude of the equivalent yield stress, σ_e , for the von Mises criterion. Thus, it seems useful to consider the ratio of the maximum normal stress to the equivalent yield stress as a likely measure of the tendency to fracture instead of yield. It is understood that this formulation does not determine, in absolute terms, whether fracturing or yielding occurs, but only measures a relative tendency. Accordingly, the ratio, σ_1/σ_e , determined from the

stress distribution shown in Fig. 5.1, is shown in Fig. 5.2. The maximum value of this ratio is of the order of 3 and occurs approximately 1 in. from the model notch-tip, which corresponds to 0.25 in. from the tip of the notch in the wide-plate prototype. Orowan⁽¹²⁾ cites theoretical evidence establishing an upper limit of approximately 3.3 for the constraint factor, q , discussed in Chapter 1 (Fig. 1.5). He further suggests that this value will likely be approached, at a point, only after significant yielding has occurred in adjacent material. The σ_1/σ_e ratio can be thought of as being equivalent to q . Thus, it appears that the Wells notch is very severe, indeed, in terms of triaxiality or suppression of flow, since it exhibits a maximum σ_1/σ_e of approximately 3 for completely elastic conditions. The point of maximum σ_1/σ_e has obvious brittle fracture implications, the details of which are discussed in subsequent sections.

5.4. Origin and Development of Fracture

Assuming that fracture is broadly dependent on the attaining of a certain normal stress, while material flow is determined by the shear-deformation energy, the region most susceptible to true brittle fracture initiation is away from the notch-tip in specimens with a Wells notch. The plot of σ_1/σ_e in Fig. 5.2 implies that ordinarily-ductile material located at a point approximately 0.5 in. from the center line of the prototype is the most susceptible to pure brittle fracture initiation. The point most likely to undergo substantial plastic deformation, leading to fibrous fracture in the shear mode, is the notch-tip, followed by the material along the whole notch perimeter

(Fig. 5.1). Where, then, does fracture initiate in wide-plate specimens employing the Wells notch as the initiator? If no plastic deformation were to occur anywhere in the specimen preceding fracture, then it could be concluded from examination of Fig. 5.1 that the most likely point of brittle fracture initiation is that coinciding with the maximum value of $\sigma_1/\sigma_{y\text{-nom}}$, i.e. at the notch-tip. However, this is an unrealistic prescription. It is more tenable to believe that all fractures, at least in crystalline materials such as steel, start as shear fractures following plastic flow, merging into brittle fracture, if this mode is to appear at all, as regions conducive to brittle fracture and/or repressive of shear fracture are reached. Hence, one distinct possibility is that fracture initiation occurs at the tip of the Wells notch, most likely as a fibrous shear fracture, progressing continuously into a true brittle fracture as the region of high triaxiality, marked in Fig. 5.2 by large values of σ_1/σ_e , becomes involved in the fracture process. This possibility presumes that major relief of triaxiality will not have occurred before the crack reaches the region in question. Shear fracture initiation, with the attendant flow at the tip of the notch, does not imply high nominal applied stresses. The extremely high local stress concentration (on the order of 13 as shown in Chapter 4) generates stresses at the notch-tip of yield magnitude under a very low applied stress. Too, it must be remembered that longitudinal tensile residual stresses, a consequence of the welding process, exist in the material surrounding the notch-tip prior to the application of any external load.

Alternatively, the specimen failure could conceivably initiate as a brittle fracture at the point of high notch constraint (high σ_1/σ_e), progressing from there toward both the specimen center line and its edge to complete fracture or to fracture arrest, depending on the availability of releasable strain energy. This possibility, although presuming that notch-tip fracture initiation is bypassed in favor of initiation a short distance away from the notch-tip, does not assume that no yielding will occur at the tip of the notch. Indeed, the high strain concentration which has been shown to exist at the notch-tip guarantees significant local material flow prior to fracture initiation, whether initiation be associated with a brittle fracture in the cleavage mode or a ductile fracture in the shear mode. Associated with load greater than that necessary to initiate notch-tip material flow is a spreading yield zone. Finally a normal stress distribution of shape similar to the curve depicted in Figure 5.2 can be expected. Some adjustment of the curve would be necessary to account for strain hardening, occurring first at the notch-tip, and for the effect of inelasticity on the notch constraint factor. Although the stress distributions in Figs. 5.1 and 5.2 are not strictly applicable after material flow occurs, since they were calculated on the basis of elasticity, the preceding arguments are qualitatively valid even beyond inception of material flow at the tip of the notch.

The occurrence of cleavage fracture initiation a small distance away from the notch-tip is not unknown; it has been verified in slow bend tests of Charpy-type specimens. (49,50) Initiation, in these tests, took place in material located approximately 0.02 in. from the plane-notch

front. Apparently a less severe notch exists in this case, in terms of ability to develop triaxiality, than with the Wells notch. A microphotograph of a cleavage crack so-developed is shown in Fig. 5.3.

The preceding considerations can also be visualized in a stress-strain plot similar to that shown in Fig. 1.5. A modified plot, more applicable to wide-plate test data and terminology, is shown in Fig. 5.4. (51) The lower curve represents the flow stress-strain curve for an unnotched specimen, whereas the raised flow stress curve represents the notched specimen. The same shifting of the flow stress curve can be obtained, to a lesser degree, by decreasing testing temperature and/or increasing strain-rate, as discussed in Chapter 1. The mechanism by which a notch can suppress material flow is illustrated in the plots of Figs. 5.1 and 5.2. Basically, through the introduction of triaxial tensions, a notch allows development of additional maximum principal stress without commensurately increasing the tendency to flow. In fact, as seen from Chapter 4 and Appendix A.2, the introduction of a hydrostatic tension, while increasing the maximum tensile stress by an amount equal to that added tension, does not alter the tendency to yield as measured by the von Mises criterion. Thus, the region of high σ_1/σ_e shown in Fig. 5.2 has a significantly raised flow stress curve in a plot such as shown in Fig. 5.4, while regions either closer to the notch-tip or farther away from the notch-tip exhibit flow stress more like that of the unnotched specimen. In the event that the introduction of triaxial tensions raises the flow stress curve sufficiently to intersect the cleavage fracture stress curve, then cleavage fracture will ensue, precluding sufficient strain to reach the

ductile shear fracture condition. It is neither pretended that the foregoing arguments are complete in every detail nor that the concepts of Fig. 5.4 are accepted universally, without qualification, as the cardinal principles governing fracture.⁽⁵²⁾ This classic representation of the dual fracture mode capability of steel is merely adopted as a vehicle with which to discuss the possible flow and fracture characteristics of the Wells notch. It is not thought, however, that the model represented by Fig. 5.4 is in fundamental error in a manner which negates the validity of its use to characterize the fracture process in broad terms.

The concepts presented in Fig. 5.4 and discussed in the preceding paragraph are not completely identical to or reconcilable with the Irwin fracture mechanics approach. If a distinction can be made, it may well be that Fig. 5.4 refers only to fracture initiation, assumed to be based on a maximum normal stress attainment, whereas the fracture mechanics approach, like the Griffith criterion, prescribes the conditions necessary to sustain fracture.

The propensity of a material to fracture in a brittle manner is not independent of its metallurgical condition. Possible variations in material properties and the fracture implications of such variations must be considered of fundamental importance in a comprehensive study of fracture. Passing note only is made of aspects of material condition in this study. The material of most interest, so far as fracture initiation is concerned, is that in the vicinity of the notch. The previous arguments of this chapter, which have not differentiated material toughness at one location from that at another, may be

substantially correct. Kihara⁽⁵³⁾ has obtained wide-plate test data from which it can be inferred that a zone of lower material toughness exists for a distance of approximately 0.75 in. from the plate center line in a welded plate of 1.0-in. thickness. The two suggested locations of fracture initiation, that is, at the notch-tip and in the region of highest σ_1/σ_e (Fig. 5.2), clearly fall in this zone, the notch-tip being 0.25 in. from the plate center line, and the point of maximum notch constraint being approximately 0.5 in. from the plate center line.

5.5. Possible Sources of Disparity in the Wide-Plate Test Results

Examination of the wide-plate test data reported in Chapter 3 (Figs. 3.2 - 3.8) allows some general conclusions to be drawn regarding all wide-plate tests which employ the Wells notch as the stress-raiser at which fracture initiation occurs. The dual fracture mode behavior of notched steel specimens is confirmed by these data which represent specimens exhibiting both high- and low-stress fractures. The transitional behavior between these two fracture modes is clearly illustrated in the figures. The most significant factor in these data is the extremely low applied nominal stress required to fracture some of the specimens.

Another aspect of these data which was discussed briefly in Chapter 3 is the rather significant degree of scatter exhibited by the data when plotted as fracture stress versus temperature. A few extreme cases, which are of particular interest, show results which seem unassignable to normal scatter. For convenience, two sources of scatter can be assumed. One is considered to be the high gradient exhibited

by stress, strain, rates of stress and strain, and material properties in the locality of fracture initiation. Coupled with the dual fracture modes, which often merge rather abruptly from one into the other, and the possibility of two-stage fractures, this high rate of change of conditions inherently promotes scatter. However, it is questionable whether some of the more severe disparities in the wide-plate test data reported herein could be assigned to this type of scatter. The second potential source of scatter, not completely independent of the first, is associated with the possibility of basic differences between specimens thought to be identical when tested to fracture. These differences can occur either during the machining of the specimen, for example, by inadvertently altering the geometry of the notch, or spontaneously, as by cracking, during specimen fabrication. The specimen differences which originate with machining are minimized by careful workmanship.

One example of spontaneous specimen alteration during fabrication is that of cracking at the root of the notch prior to the low temperature fracture test. This event could cause wide disparity of fracture strength between cracked and uncracked specimens. That it is also a distinct possibility can be appreciated by a consideration of the high strains and stresses to which the notch-tip is subjected by the forces which develop during fabrication. The major source of these stresses and strains is the welding process. It has been shown that in an unnotched plate of similar proportions to the notched plates used in the wide-plate tests reported herein, tensile welding residual stresses in the center of the plate approach yield stress magnitude.⁽³⁴⁾ The implication is clear that strains substantially higher than those

required to produce yield stress have occurred during the welding process. In the notched plate, much more severe conditions pertain in that the straining effect of the gross forces due to welding is multiplied at the notch-tip by the very high concentration which exists there. It has been shown that extensive prestraining before the fracture test can have the effect of exhausting some of the material's ductility, thereby lowering its subsequent energy absorbing capacity.⁽⁵⁴⁾ Thus, a very real possibility of cracking at the notch-tip during or immediately after welding exists. It is true that for identical specimens, specimen response to supposedly equivalent environments should be such as to make each specimen equally susceptible to this cracking. However, it is reasonable to expect that the conditions necessary to cause notch-tip cracking and/or the environment's acting to cause such cracking vary slightly from one specimen to the next.

The specimen in which weld cracking occurred would be expected to behave quite differently from the uncracked specimen in the fracture test. In general, it seems that notch-tip cracking during or immediately after welding would lead to a less severe, though slightly longer, notch. Thus, the specimens which exhibit no notch-tip cracking are postulated to exhibit lower fracture stress behavior than those specimens that have developed internal cracks. It is emphasized that the confirmation of high strain gradients in the material immediately surrounding the Wells notch is prerequisite to the foregoing postulation of notch-tip cracking.

CHAPTER 6

SUMMARY AND CONCLUSIONS

A significant research effort has been expended in recent years to increase understanding of the brittle fracture of structural metals. Concern for brittle fracture susceptibility has been heightened by the incidence of such fractures. The present study is concerned with the flow and fracture characteristics of the Wells notch used in the initiation of brittle fractures in notched and welded wide-plates.

The scope of this investigation is outlined in Chapter 2, after a review of the brittle fracture phenomenon is presented in Chapter 1. Results of some wide-plate tests are presented in Chapter 3. Two conclusions can be drawn from these data:

1. Notched and welded wide-plates, when tested to failure, exhibit susceptibility for two fracture modes. The shear fracture mode occurs under high applied stress and results in a fibrous-appearing fracture and significant gross deformation. Cleavage fracture, which is crystalline in appearance, is the second mode. Cleavage fractures can occur at applied stresses which are high or low, but, in any event, will be accompanied by little gross deformation. Since the occurrence of brittle cleavage fractures in steel plates is confined to plates containing severe notches, steel is known as a notch-brittle material.

2. Test data for notched and welded wide-plates exhibit a significant amount of scatter, which is characteristic of the fracture phenomenon.

The details of a frozen-stress photoelastic study by which stresses in the vicinity of the Wells notch were investigated are contained in Chapter 4. An interpretation of the results of this stress analysis, in terms of the wide-plate test, is presented in Chapter 5. Conclusions which can be drawn from this material are:

1. Stresses in the vicinity of the Wells notch, due to applied loads in the wide-plate specimen, can be modeled by a three-dimensional photoelastic specimen into which stresses have been frozen. An epoxy model is utilized in this study to determine the elastic stress distribution in the material adjacent to the Wells notch.

2. High strain concentrations exist in the region adjacent to a Wells notch when tensile loads perpendicular to the plane of the notch are applied to a specimen. The elastic stress concentration at the tip of the notch is of the order of 13 ± 1 , and at the notch-flat is approximately 5. The elastic stress concentrations at the junction of the notch with the plate surface are also high. Concentrations of approximately 6 and 2.5 pertain for the "weld" and plate side of the notch, respectively. Strain concentrations of similar magnitude exist at other points on the notch perimeter.

3. Very high stress gradients were found to be associated with the regions of high stress. A significant attenuation of stress intensity appears to occur within 0.01 in. of the notch boundary of the prototype wide-plate.

4. Severe suppression of material flow, as determined by the von Mises criterion, occurs in specimens employing the Wells notch. The region, in the plane of the notch, at which this suppression is

greatest is located about 0.25 in. from the tip of the notch in the prototype wide-plate specimen.

5. Conditions of stress, strain, and freedom to yield are most conducive to fibrous shear fracture at the tip of the Wells notch in the wide-plate specimen. Brittle cleavage fracture is likely to occur, if at all, a short distance from the notch-tip, in a region of proven high triaxiality corresponding to low magnitudes of von Mises equivalent yield stress. This region, in addition to providing significant constraint against yielding, can have relatively high maximum normal stress and relatively low material toughness, both of which are conducive to cleavage fracture.

6. The most likely fracture initiation modes and locations in wide-plate specimens employing a Wells notch are postulated to be:

(a) fibrous shear fracture, initiating at the tip of the notch,

(b) brittle cleavage fracture, initiating away from the notch-tip in the region of high triaxiality, and

(c) fibrous shear fracture, initiating at the tip of the notch and becoming a brittle cleavage fracture as the region of high triaxiality is reached.

7. Scatter and disparities in the test data for wide-plate specimens are thought to result from the high gradient for conditions, such as stress, strain, rates of stress and strain, and material toughness, in the vicinity of fracture initiation, as well as the dual fracture mode behavior of steel for which significant scatter is inherent. One of the consequences of sharply varying environment in

the notch vicinity can be the development, in some specimens, of cracking at the notch-tip prior to the fracture test. In the fracture test, behavior of such cracked specimens can be expected to differ significantly from that of uncracked specimens.

BIBLIOGRAPHY

1. Sub-Commission D, "Behavior of Metals Subjected to Welding," Int. Inst. of Welding, Doc. No. IX-353-63, 1963.
2. Vedeler, G., "To What Extent Do Brittle Fracture and Fatigue Interest Shipbuilders Today?," Sveiseteknikk, vol. 17, no. 3, pp. 36-47, 1962.
3. Japanese Delegation, "Brittle Fracture of the Deck in the Quick-Freeze Chamber of a Refrigerator Ship," Int. Inst. of Welding, Doc. No. IX-347-63, 1963.
4. Shank, M. E., "A Critical Survey of Brittle Failure in Carbon Plate Steel Structures Other than Ships," Welding Res. Coun. Bull. Series, No. 17, 1954.
5. Hodgson, J. and Boyd, G. M., "Brittle Fracture in Welded Ships," Trans. Inst. Naval Arch., vol. 100, pp. 141-180, 1958.
6. Williams, M. L. and Ellinger, G. A., "Investigation of Structural Failures of Welded Ships," Welding J., vol. 32, no. 10, Res. Suppl., pp. 498s-527s, 1953.
7. Brown, D. P., "Observations on Experience with Welded Ships," Ibid., vol. 31, no. 9, pp. 765-782, 1952.
8. Irwin, G. R., "Fracture Mechanics," Proc. First Symposium Naval Struct. Mech., Stanford Univ., pp. 557-594, 1958.
9. Griffith, A. A., "The Phenomena of Rupture and Flow in Solids," Phil. Trans. Roy. Soc. London, A, vol. 221, pp. 163-198, 1921.
10. Griffith, A. A., "The Theory of Rupture," Proc. First Int. Cong. Appl. Mech., Delft, pp. 55-63, 1924.
11. Wells, A. A., "Brittle Fracture Mechanics: A Survey of Published Work," Int. Inst. of Welding, Doc. No. IX-239-59, 1959.
12. Orowan, E., "Fundamentals of Brittle Behavior in Metals," Fatigue and Fracture of Metals (Symposium), John Wiley, pp. 139-167, 1952.
13. Irwin, G. R., "Fracture Dynamics," Fracture of Metals (Symposium), Am. Soc. Metals, Cleveland, pp. 147-166, 1948.
14. Felbeck, D. K. and Orowan, E., "Experiments on Brittle Fracture of Steel Plates," Welding J., vol. 34, no. 11, Res. Suppl., pp. 570s-575s, 1955.

15. Irwin, G. R., "Relation of Crack Toughness Measurements to Practical Applications," Ibid., vol. 41, no. 11, Res. Suppl., pp. 519s-528s, 1962.
16. Irwin, G. R., "Analysis of Stresses and Strains Near the End of a Crack Traversing a Plate," J. Appl. Mech., vol. 24, no. 3, pp. 361-364, 1957.
17. Irwin, G. R., "Fracturing and Fracture Mechanics," Theor. and Appl. Mech. Rept. 202, Univ. of Ill., 1961.
18. ASTM Symposium Contributors, Fracture Toughness Testing and Its Applications (Symposium), ASTM, Chicago, 1964.
19. Westergaard, H. M., "Bearing Pressures and Cracks," Trans. ASME, vol. 61, pp. A49-A53, 1939.
20. Inglis, C. E., "Stresses in a Plate Due to the Presence of Cracks and Sharp Corners," Trans. Inst. Naval Arch., vol. 55, pt. I, p. 219, 1913.
21. ASTM Committee, "Fracture Testing of High Strength Sheet Materials," ASTM Bull., No. 243, pp. 29-40, January, 1960.
22. ASTM Committee, "Fracture Testing of High Strength Sheet Materials," Ibid., No. 244, pp. 18-28, February, 1960.
23. Kennedy, H. E., "Some Causes of Brittle Failures in Welded Mild Steel Structures," Welding J., vol. 24, no. 11, Res. Suppl., pp. 588s-598s, 1945.
24. Greene, T. W., "Evaluation of the Effect of Residual Stresses," Ibid., vol. 28, no. 5, Res. Suppl., pp. 193s-204s, 1949.
25. Wells, A. A., "The Brittle Fracture Strengths of Welded Steel Plates," Trans. Inst. Naval Arch., vol. 98, p. 296, 1956.
26. Wells, A. A., "Brittle Fracture Strength of Welded Steel Plates," Brit. Welding J., vol. 8, no. 5, pp. 259-277, 1961.
27. Wells, A. A., "Brittle Fracture Strengths of Welded and Notched 3 Inch Thick Steel Plates," Ibid., vol. 8, no. 8, pp. 389-401, 1961.
28. Wells, A. A. and Burdekin, F. M., "Effects of Thermal Stress Relief and Stress Relieving Conditions on the Fracture of Notched and Welded Wide Plates," Brit. Welding Res. Assoc. Rept. B6/23/62, 1962.
29. Woodley, C. C., Burdekin, F. M., and Wells, A. A., "Mild Steel for Pressure Equipment at Sub-Zero Temperatures," Ibid., C88/4/63, 1963.

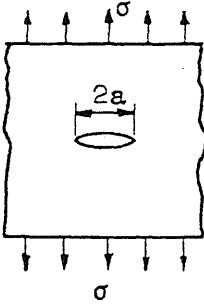
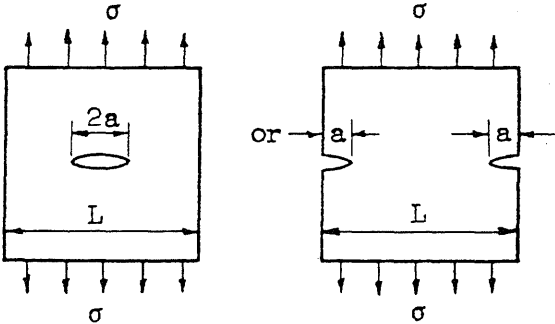
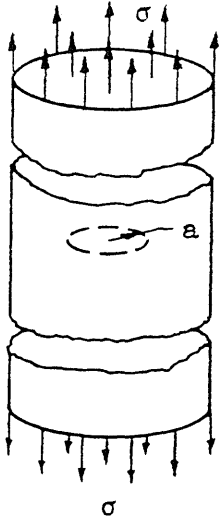
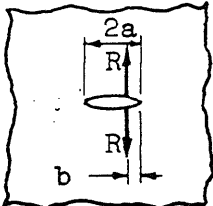
30. Wells, A. A., "Influence of Residual Stresses and Metallurgical Changes on Low-Stress Brittle Fracture in Welded Steel Plates," Welding J., vol. 40, no. 4, Res. Suppl., pp. 182s-192s, 1961.
31. Kihara, H., "Recent Studies in Japan on Brittle Fracture of Welded Steel Structure(s) Under Low Applied Stress Level," Japan Inst. Welding, September, 1961.
32. Wilson, W. M., Hechtman, R. A., and Bruckner, W. H., "Cleavage Fractures of Ship Plates," Univ. of Ill. Bull., Engineering Experiment Station, No. 388, March, 1951.
33. Hall, W. J., Nordell, W. J., and Munse, W. H., "Studies of Welding Procedures," Welding J., vol. 41, no. 11, Res. Suppl., pp. 505s-518s, 1962.
34. Nordell, W. J. and Hall, W. J., "Two Stage Fracturing in Welded Mild Steel Plates," Ibid., vol. 44, no. 3, Res. Suppl., pp. 124s-134s, 1965.
35. Hall, W. J., Joshi, J. R., and Munse, W. H., "Studies of Welding Procedures--Part II," Ibid., vol. 44, no. 4, Res. Suppl., pp. 182s-192s, 1965.
36. Boodberg, A., Davis, H. E., Parker, E. R., and Troxell, G. E., "Causes of Cleavage Fracture in Ship Plate--Tests of Wide Notched Plates," Ibid., vol. 27, no. 4, Res. Suppl., pp. 186s-199s, 1948.
37. Gensamer, M., "General Survey of the Problem of Fatigue and Fracture," Fatigue and Fracture of Metals (Symposium), John Wiley, pp. 1-17, 1952.
38. Mylonas, C., "Static Brittle Fracture Initiation Without Residual Stresses," Welding J., vol. 40, no. 11, Res. Suppl., pp. 516s-520s, 1961.
39. Barton, F. W. and Hall, W. J., "Brittle Fracture Tests of Six-Foot Wide Prestressed Steel Plates," Welding J., vol. 39, no. 9, Res. Suppl., pp. 379s-384s, 1960.
40. Munse, W. H., Cannon, J. P., and Kiefner, J. F., "Effect of Repeated Loads on Brittle Fracture in Welded Ship Plate," Unpublished Research Status Report, Dept. of Civil Engr., Univ. of Ill., 1964.
41. Drucker, D. C., "Three-Dimensional Photoelasticity," Handbook of Experimental Stress Analysis, M. Hetenyi, ed., John Wiley, pp. 924-965, 1950.
42. Heywood, R. B., Designing by Photoelasticity, Chapman and Hall, London, 1952.

43. Leven, M. M., "Epoxy Resins for Photoelastic Use," Photoelasticity (Symposium), M. M. Frocht, ed., Macmillan, pp. 145-165, 1963.
44. Post, D., "Isochromatic Fringe Sharpening and Fringe Multiplication in Photoelasticity," Proc. Soc. Exp. Stress Anal., vol. XII, no. 2, pp. 143-156, 1955.
45. Brock, J. S., "The Determination of Effective Stress by Means of Small Cubes Taken from Photoelastic Models," David Taylor Model Basin Rept. 829, September, 1952.
46. Wahlstrom, E. E., Optical Crystallography, Third ed., John Wiley, 1960.
47. Frocht, M. M. and Guernsey, R., "Studies in Three-Dimensional Photoelasticity," Proc. First U.S. Natl. Cong. Appl. Mech., ASME, pp. 301-307, 1952.
48. Neuber, H., Theory of Notch Stresses: Principles for Exact Calculation of Strength with Reference to Structural Form and Material, U.S. Govt. Translation, AEC-tr-4547, Second ed., 1961.
49. Knott, J. F. and Cottrell, A. H., "Notch Brittleness in Mild Steel," J. Iron and Steel Inst., vol. 201, pt. 3, pp. 249-260, 1963.
50. Wilshaw, T. R., "The Deformation and Fracture of Mild Steel Charpy Specimens," Dept. Matl. Science Rept. 66-6, Stanford Univ., 1966.
51. Otani, M. and Ideguchi, Y., "A Proposal on the Interpretation of the Mechanism of Fracture Transition in Notched Specimen(s)," Int. Inst. of Welding, Doc. No. IX-366-63, 1963.
52. Barrett, C. S., "Session on Cleavage Fracture," Fracture (Conference), B. L. Averbach, D. K. Felbeck, G. T. Hahn, and D. A. Thomas, eds., MIT and John Wiley, pp. 1-8, 1959.
53. Kihara, H., "Discussion of Doc. X-226-59 by C. Mylonas," Int. Inst. of Welding, Doc. No. X-258-60, 1960.
54. Mylonas, C. and Rockey, K. C., "Exhaustion of Ductility by Hot Straining--An Explanation of Fracture Initiation Close to Welds," Welding J., vol. 40, no. 7, Res. Suppl., pp. 306s-310s, 1961.

TABLE 1.1. DETAILS OF FIVE CASES OF FIELD BRITTLE FRACTURES

CASE	FAILURE DETAILS				MATERIAL PROPERTIES									
	Nominal Stress σ_f , ksi	Initiation Temp. °F.	Initiator	Remarks	Physical Properties				Chemical Properties (%)					
					σ_y ksi	σ_{ult} ksi	Elongation % (gage length)	Charpy V-Notch Energy, ft-lb (Temperature, °F)	C	Mn	Si	S	P	Other
1 Oil Storage Tank	12	5-30	Crack in between course plate; existed before welding	Material proved sensitive to strain ageing; low material toughness in initiation vicinity in service 4 1/2 years	--	55-62	23-30 (8 in.)	20 (10)	0.03-0.06	0.31-0.33	Trace	0.03-0.034	0.038-0.041	0.01-0.012 (N)
2 Ship	--	41	Point where stiffening members, of various orientation, met	Unfinished ship still on building way	--	--	---	50 (14)	--	--	--	--	--	--
3 Oil Tanker	14	--	Flame cut float gage opening	Material exhibited very low toughness; in service 8 years	37	65	25.5 (8 in.)	~ 7 (40)	--	--	--	--	--	--
4 Pressure Vessel	3	~ -350	Fatigue crack at junction of support lug and tank	High temperature gradient from top to bottom of tank; likely high thermal stresses; mild steel materials; in service 8 months	--	--	---	--	0.25	0.69	0.10	0.02	0.03	0.02 (A1)
5 Railway Tank Car	--	16	Fatigue crack at reinforcement weld which had been "strengthened"	Fracture triggered by shunting impact; in service 16 years	42-49	71-76	--- (Reduction in Area = 30%)	50 (16)	0.21	1.38	0.47	0.012	0.045	0.0036 (N)

TABLE 1.2 CRACK-EXTENSION FORCE, G, FOR FIVE CONFIGURATIONS (8)

CONFIGURATION	CRACK-EXTENSION FORCE, G *
	$\frac{\sigma^2 \pi a}{E}$
	$\frac{\sigma^2 L}{E} \tan \frac{\pi a}{L}$
	$\frac{4\sigma^2 a}{\pi E}$
	$\frac{R^2}{\pi E} \left(\frac{2a-b}{ab} \right)$

* Tabulated values are for plane-stress; for plane-strain multiply by $1-\mu^2$ where μ is Poisson's ratio.

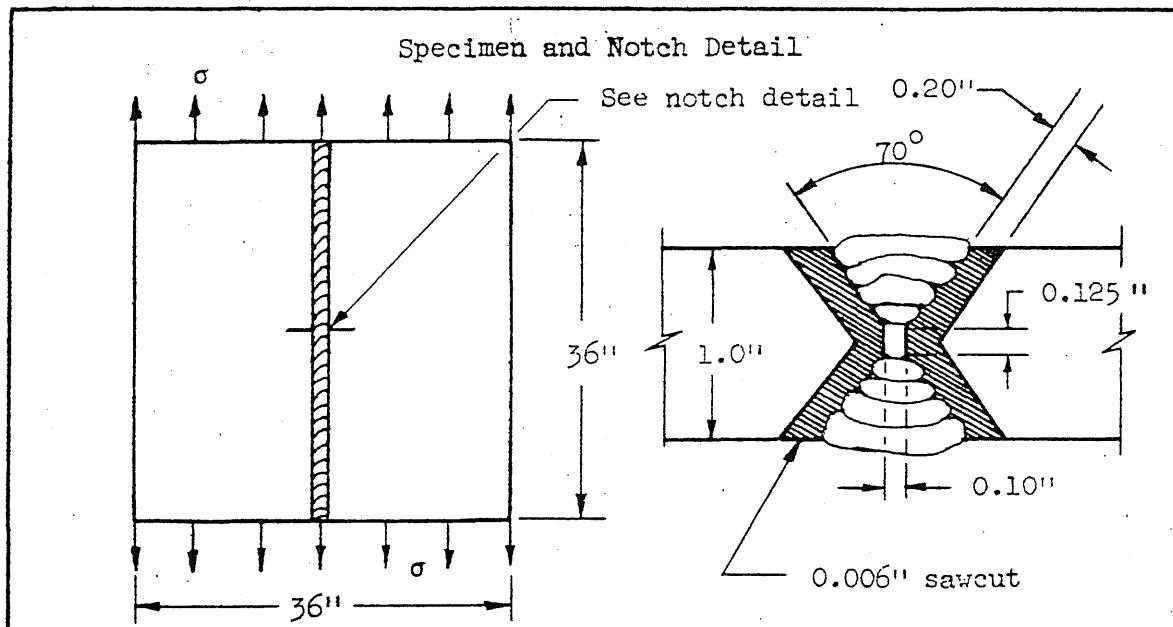
TABLE 3.1. MATERIAL PROPERTIES OF SPECIMENS USED IN WIDE-PLATE TESTS

Test Series	PHYSICAL PROPERTIES					CHEMICAL PROPERTIES (%)								
	σ_y	σ_{ult}	Elongation	Red. in Area	Charpy V-Notch Temp. at 15 ft-lb $^{\circ}F$	C	Mn	P	S	Si	Cr	Cu	Sn	Al
	ksi	ksi	%	%										
1	28.6 (est.)	57.6	--	52.8	83	0.175	0.70	0.043	0.051	0.04	----	0.12	0.012	--
2	29.4	54.8	31	--	63	0.18	0.54	0.026	0.039	0.04	0.06	0.10	0.024	0.005
3	33.2	54.8	35	--	3	0.14	1.07	0.039	0.042	0.02	0.02	0.08	0.013	0.001
4	37.6	56.8	33	--	-49	0.15	1.05	0.028	0.041	0.17	0.04	0.08	0.025	0.005
5	36.2 [*] 40.1 ^{**}	70.6 [*] 82.1 ^{**}	37 [*] 33 ^{**}	--	25	0.30	0.76	0.008	0.028	0.26	--	--	--	--
6	39.4	70.6	35	--	5	0.24	0.69	0.022	0.03	0.20	0.08	0.22	--	0.034

* Specimens 1-1 and 1-2

** Specimen 1-3

TABLE 3.2 WIDE-PLATE TEST DATA: SERIES 1 (25)

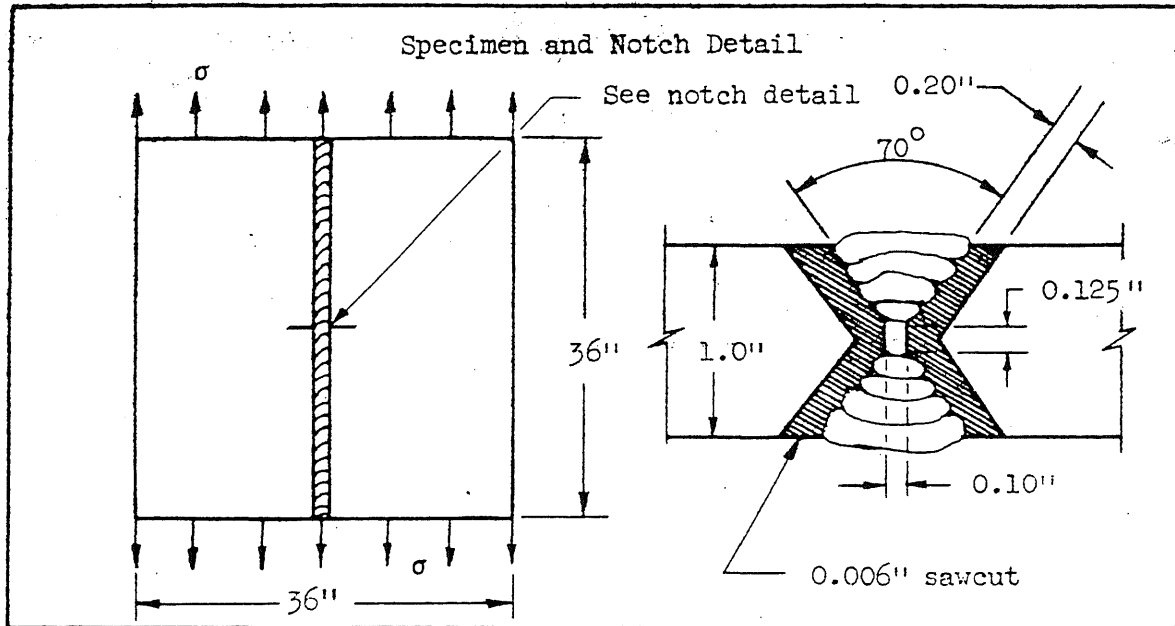


<u>SPECIMEN</u>	<u>TEST TEMPERATURE, °F</u>	<u>NOMINAL FRACTURE STRESS, KSI</u>
A	22	0/31.4 *
B	25	0.6/31.2
C	30	2.4/31.0
D	43	2.6/32.0
E	18	5.8/31.6
F	23	5.8/31.6 **
G	24	10.2/32.0
H	39	18.8

* Two-stage fractures denoted in this manner.

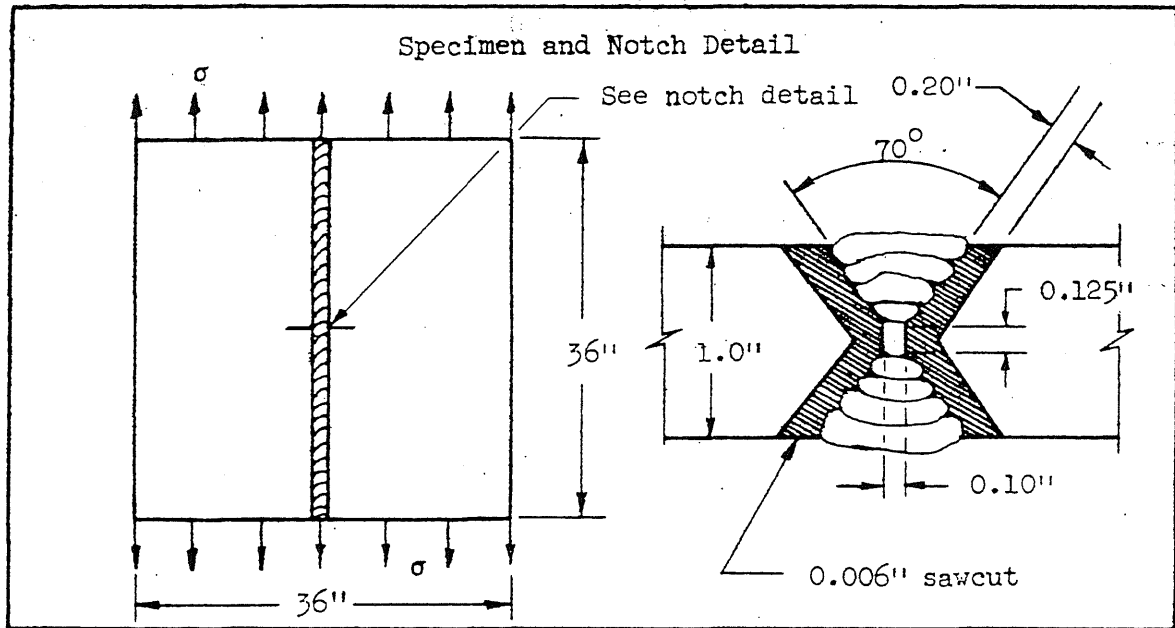
** Tested to failure at 59° F.

TABLE 3.3 WIDE-PLATE TEST DATA: SERIES 2 (26)



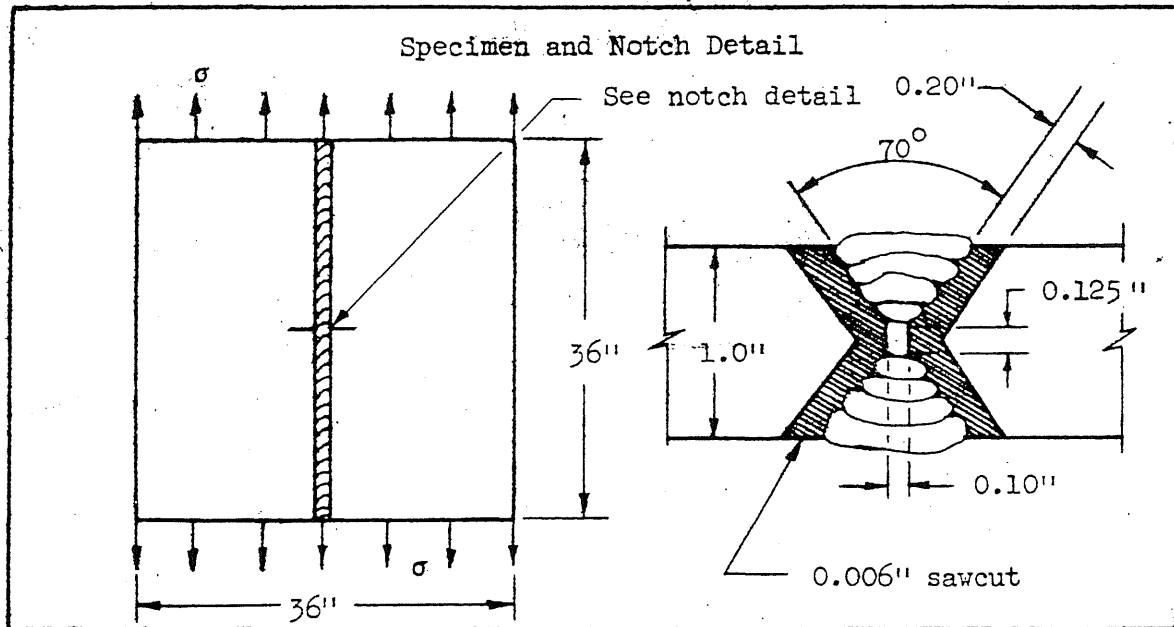
<u>SPECIMEN</u>	<u>TEST TEMPERATURE, °F</u>	<u>NOMINAL FRACTURE STRESS, KSI</u>
1	-18	7.0/36.8
2	-13	20.2
3	-13	17.4
6	-4	10.4
7	10	17.0
9	14	28.8
15	20	32.0

TABLE 3.4 WIDE-PLATE TEST DATA: SERIES 5 (26)

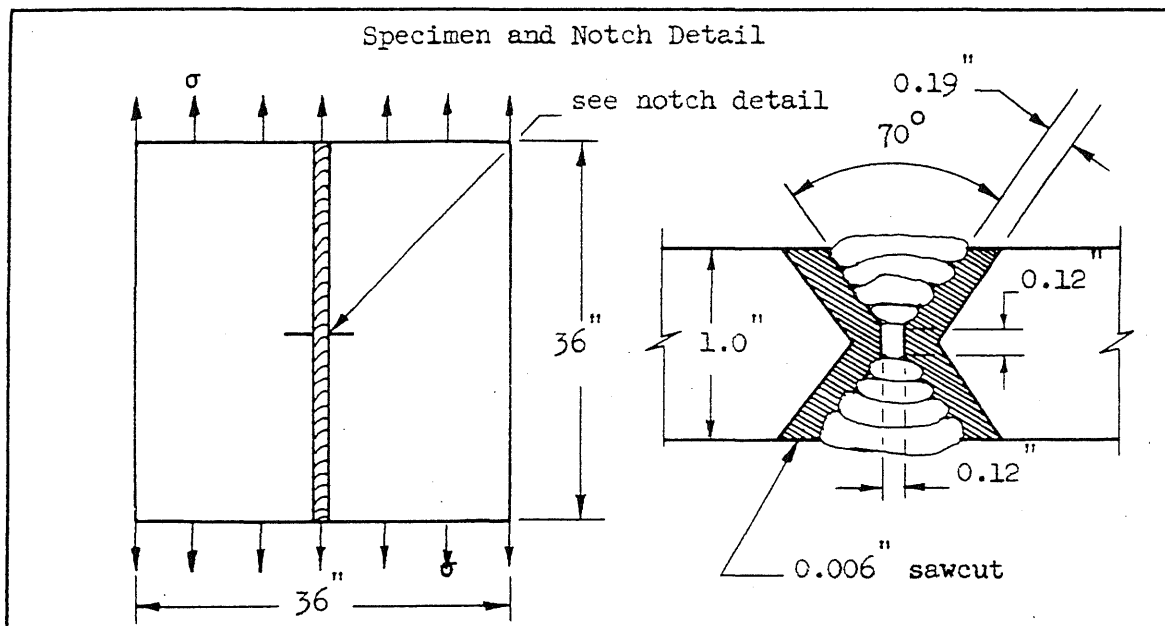


<u>SPECIMEN</u>	<u>TEST TEMPERATURE, °F</u>	<u>NOMINAL FRACTURE STRESS, KSI</u>
1	-31	10.0
3	-13	7.6/38.0
4	- 8	1.6/36.6
5	12	37.0
6	- 4	35.0
7	2	13.2
8	3	16.8

TABLE 3.5 WIDE-PLATE TEST DATA: SERIES 4 (26)

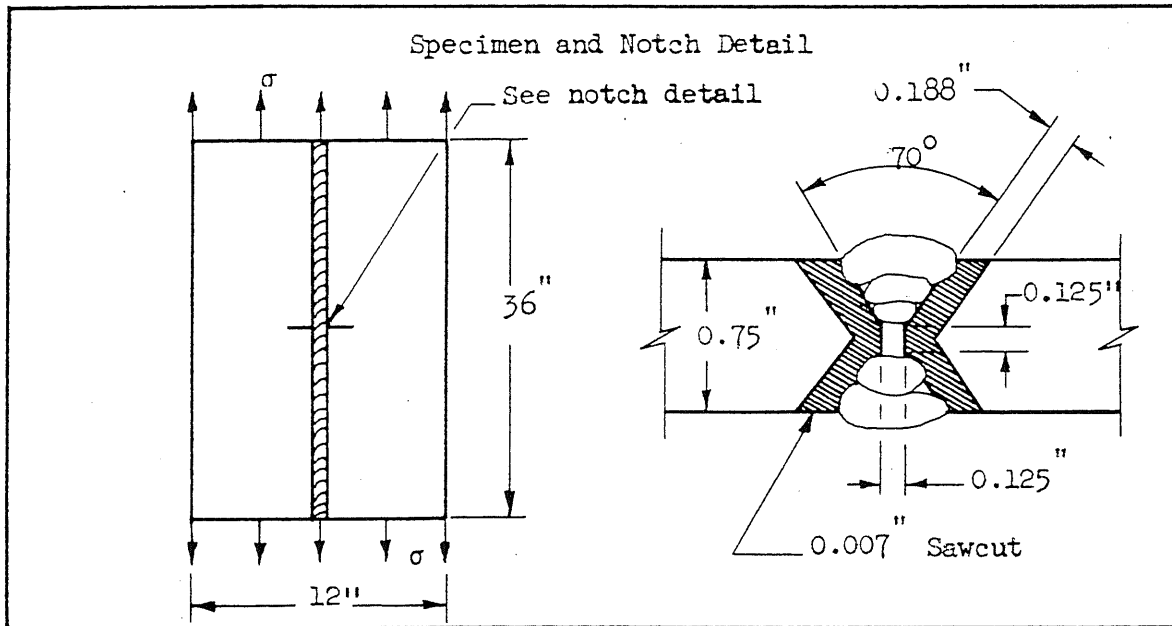


<u>SPECIMEN</u>	<u>TEST TEMPERATURE, °F</u>	<u>NOMINAL FRACTURE STRESS, KSI</u>
1	-76	44.6
3	-61	42.0
4	-58	44.6
5	-54	42.0
6	-40	6.8/47.8
8	-40	47.0
9	-31	43.6
10	-25	43.0
12	-13	42.2

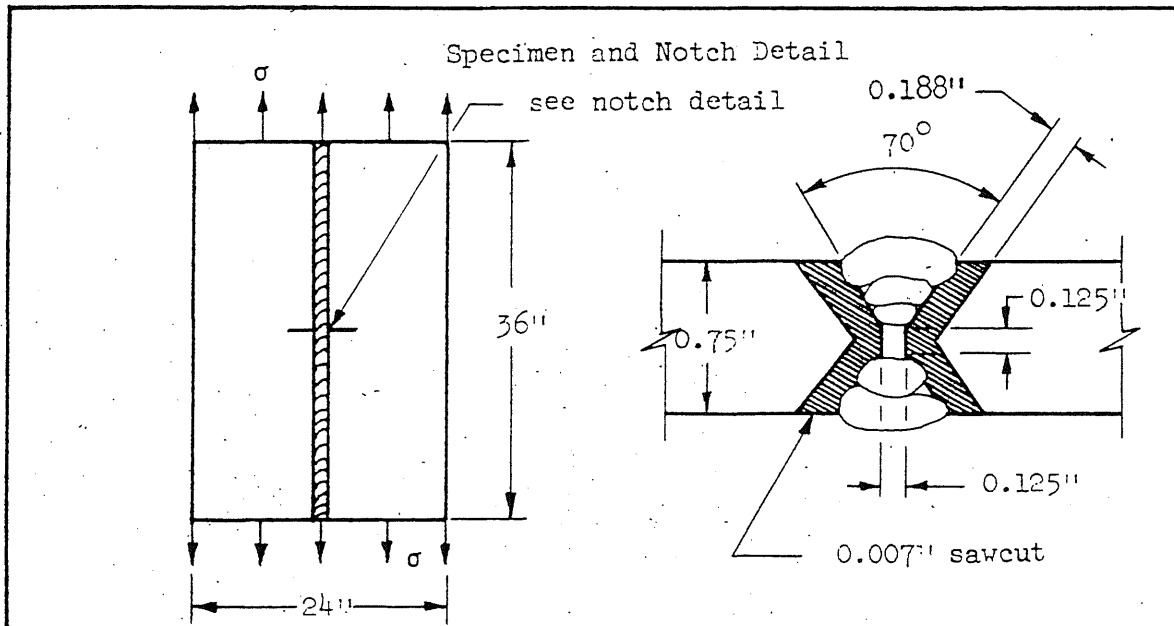
TABLE 3.6 WIDE-PLATE TEST DATA: SERIES 5⁽³³⁾

<u>SPECIMEN</u>	<u>TEST TEMPERATURE, °F</u>	<u>NOMINAL FRACTURE STRESS, KSI</u>
1-1	-30	6.4/43.0
1-2	-40	9.4
1-3	-40	22.4

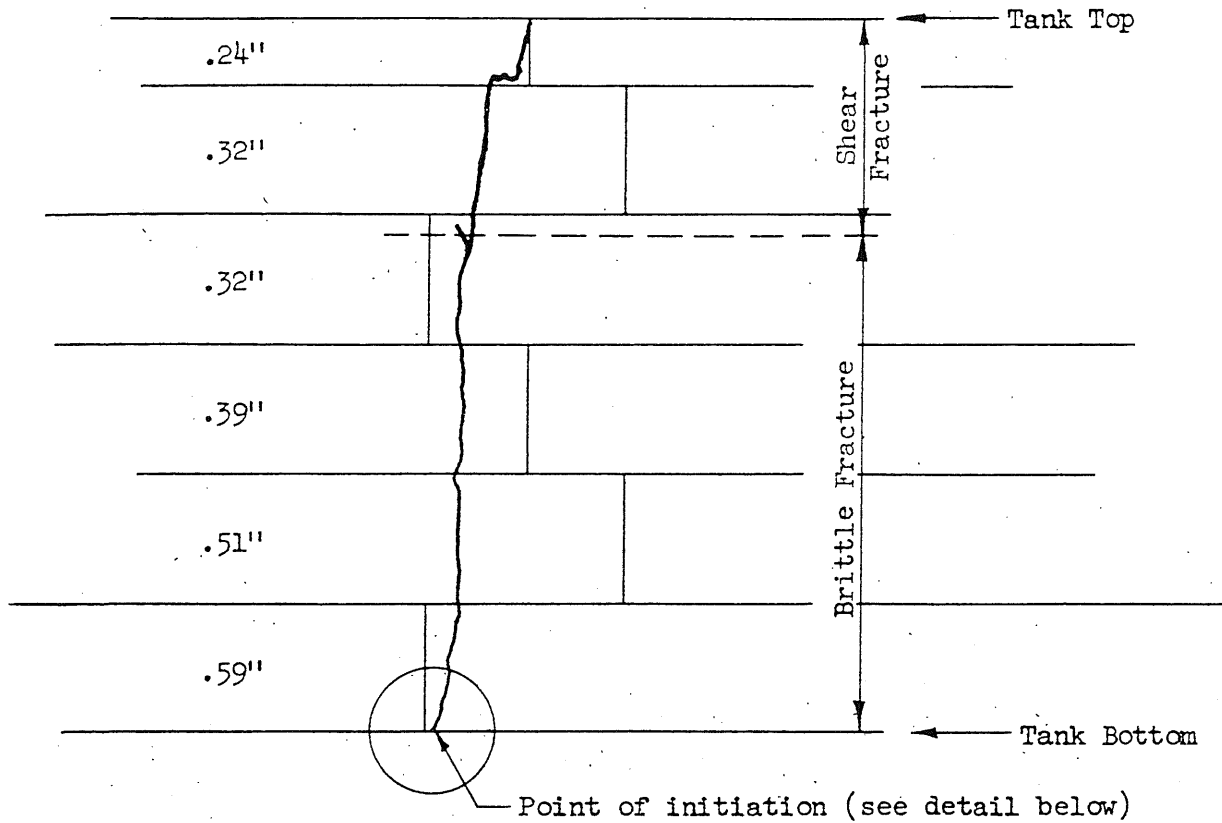
TABLE 3.7 WIDE-PLATE TEST DATA: SERIES 6(a) (40)



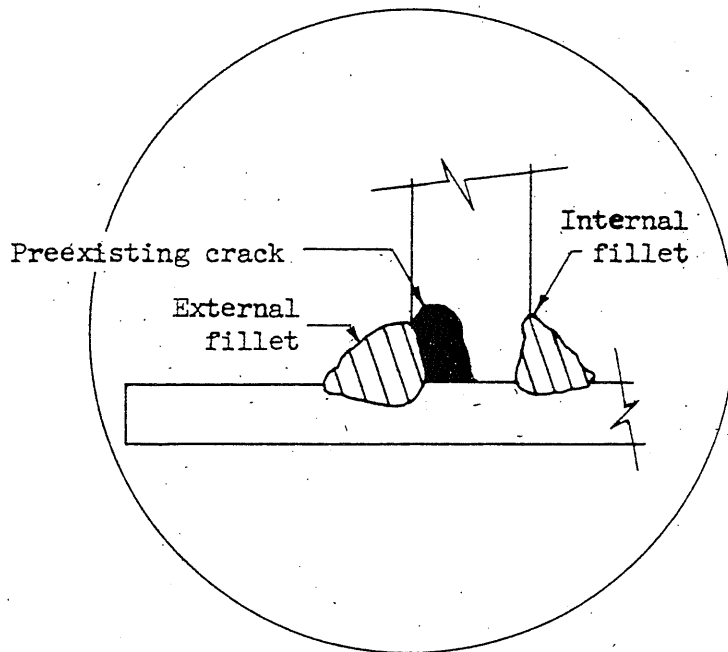
<u>SPECIMEN</u>	<u>TEST TEMPERATURE, °F</u>	<u>NOMINAL FRACTURE STRESS, KSI</u>
WP-2	-46	49.2
WP-5	-80	13.3
WP-15	-80	56.7
WP-16	-92	18.0

TABLE 3.8 WIDE-PLATE TEST DATA: SERIES 6(b)⁽⁴⁰⁾

<u>SPECIMEN</u>	<u>TEST TEMPERATURE, °F</u>	<u>NOMINAL FRACTURE STRESS, KSI</u>
WP-18	-70	6.0
WP-19	-42	4.6/49.5
WP-24	-21	17.9
WP-25	- 2	4.0/52.3
WP-26	-20	5.0/37.0
WP-27	28	5.4/54.2



(a) POSITION OF THE MAIN FRACTURE IN THE SHELL OF THE TANK (1/10" = 1.0')



(b) DETAIL OF THE ORIGIN OF THE CRACK (Actual Size)

FIG. 1.1 FRACTURE OF AN OIL STORAGE TANK

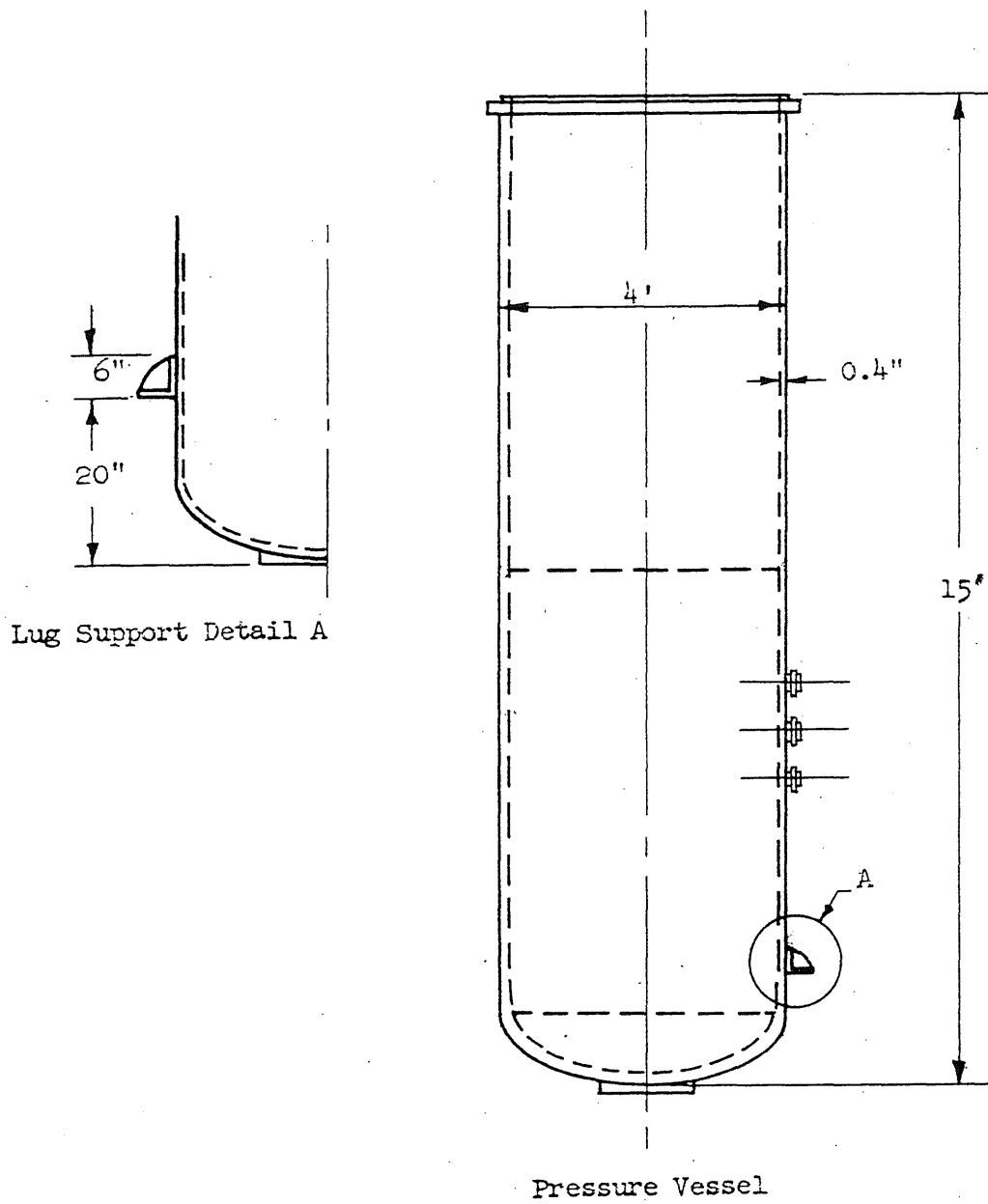


FIG. 1.2 VERTICAL PRESSURE VESSEL WITH LUG SUPPORT DETAIL

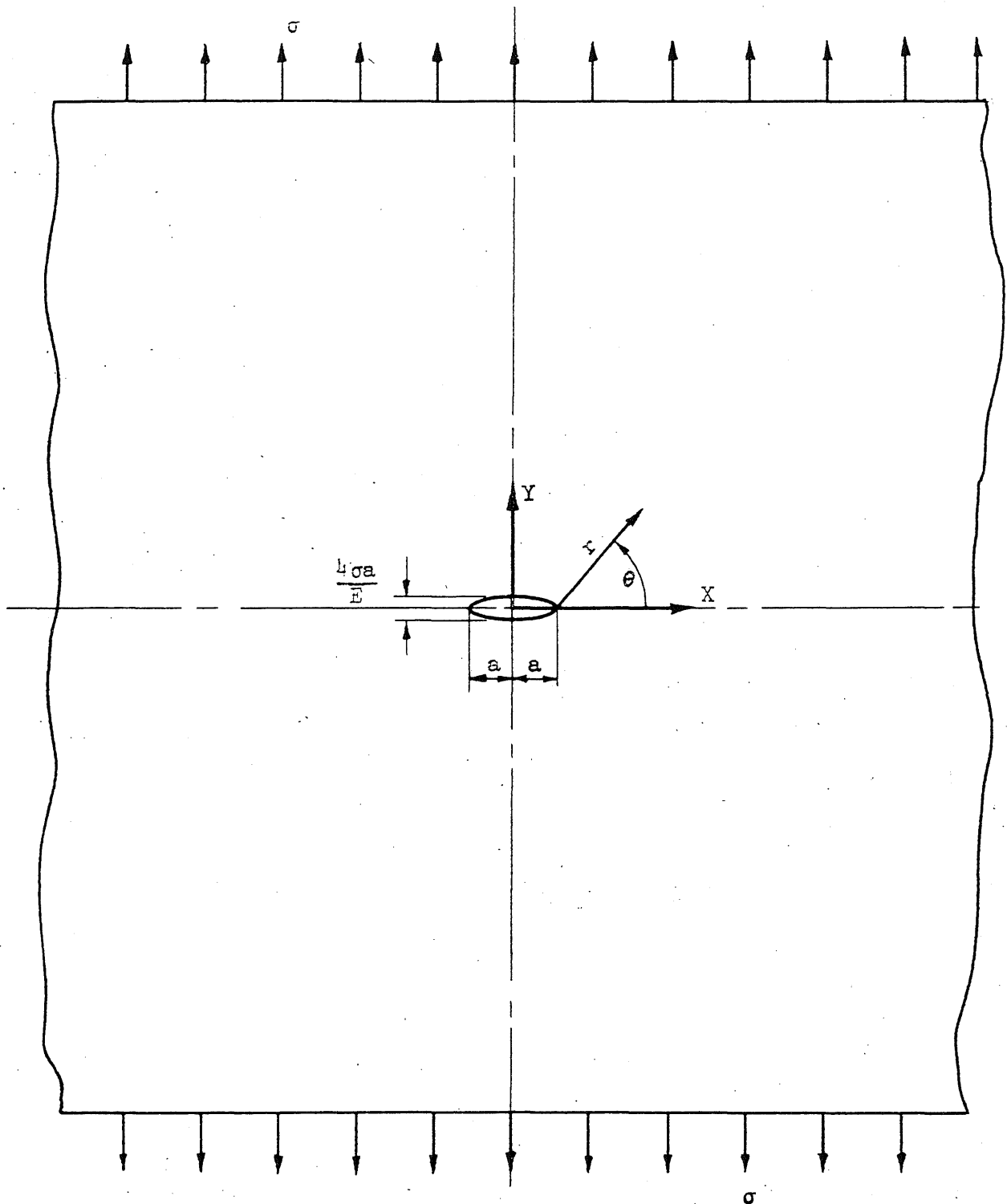


FIG. 1.3 GRIFFITH-IRWIN CRACK EXTENSION MODEL

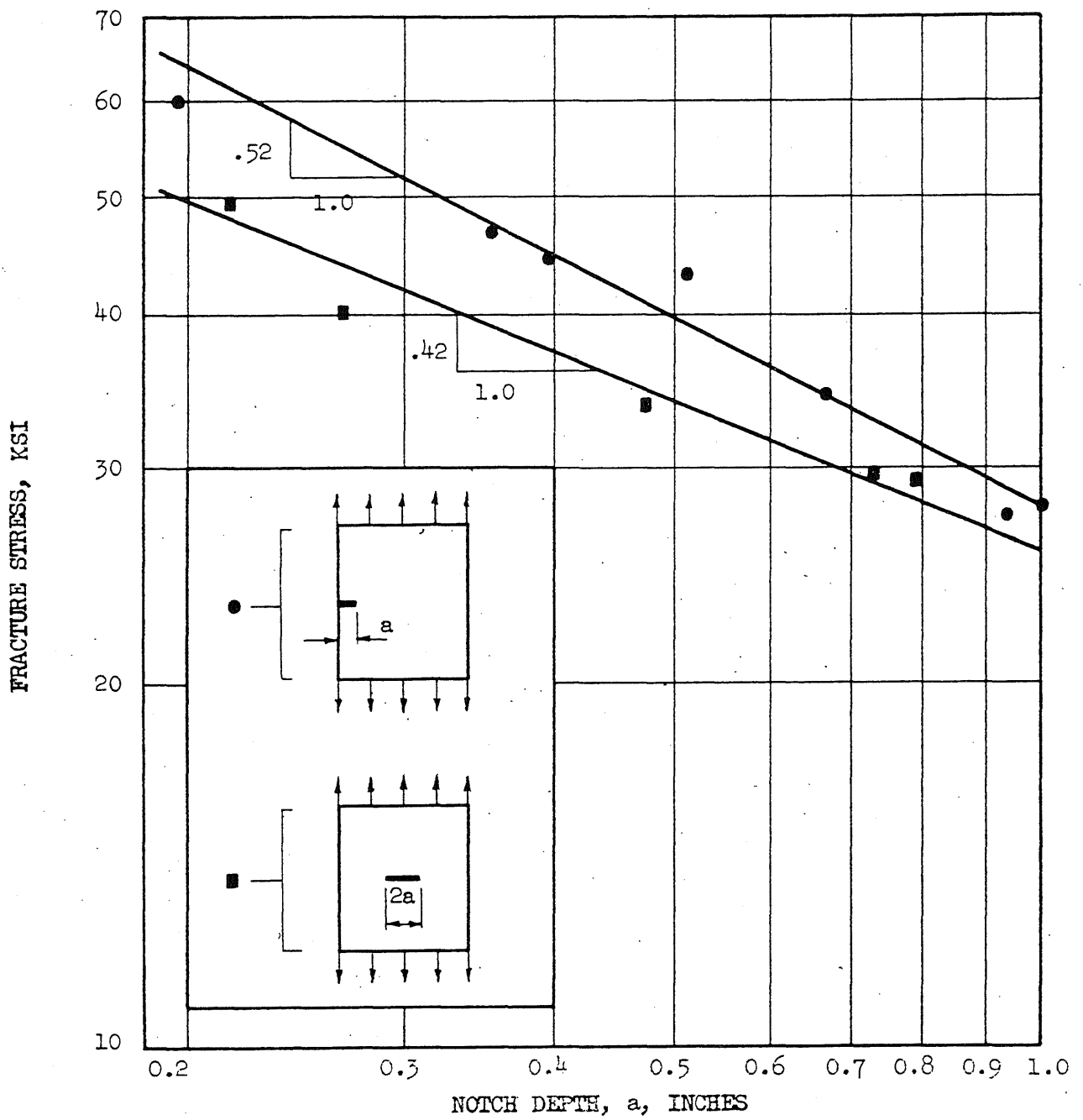


FIG. 1.4 FRACTURE STRESS VERSUS NOTCH DEPTH FOR NOTCHED
 PLATE TESTS ON SHIP-STEEL (After Orowan and Felbeck⁽¹⁴⁾)

Y_d = Normal Tensile Stress-Strain
Curve

q = Constraint Factor

B = Brittle Strength Curve

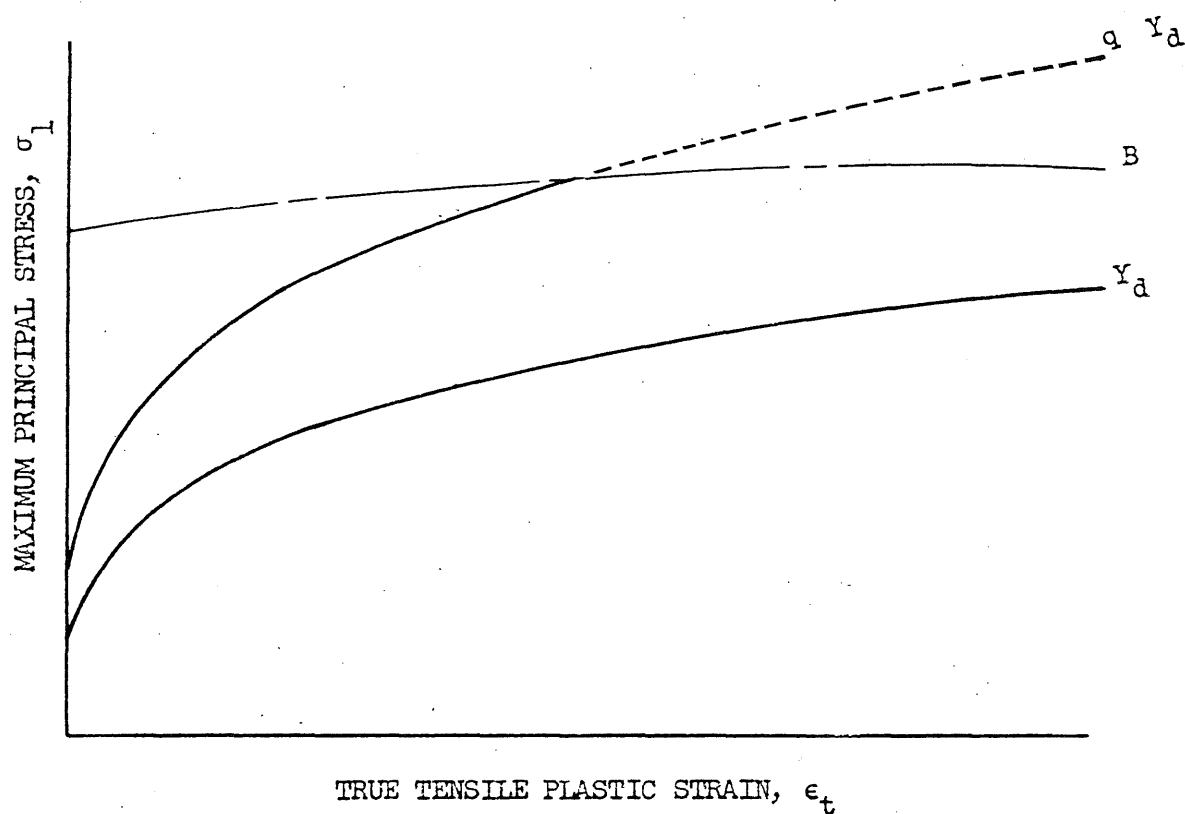


FIG. 1.5 STRESS-STRAIN PLOT SHOWING THE CONCEPT
OF NOTCH BRITTLENESS (After Orowan⁽¹²⁾)

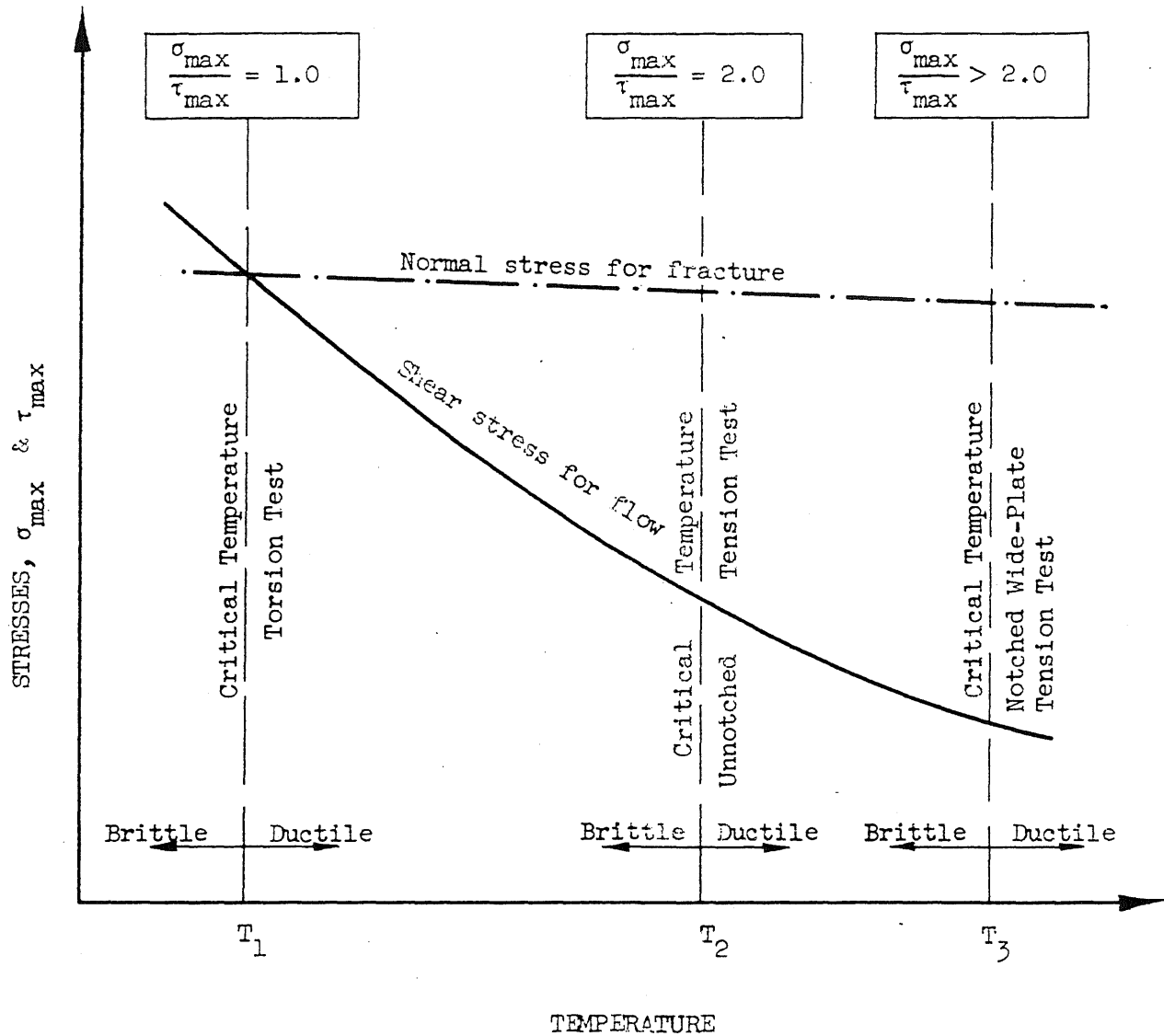


FIG. 1.6 THE ROLE OF THE RELATIVE TEMPERATURE DEPENDENCIES OF THE PROCESSES OF FLOW & FRACTURE IN DETERMINING THE TRANSITION TEMPERATURE (After Gensamer⁽³⁷⁾)

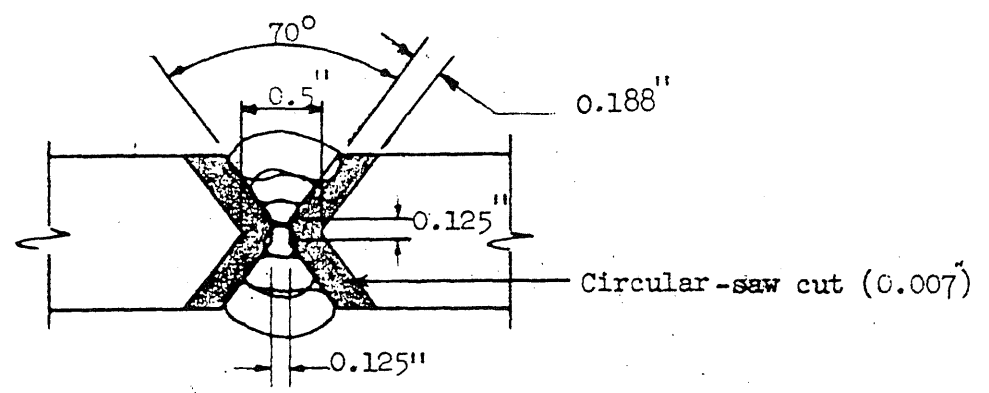
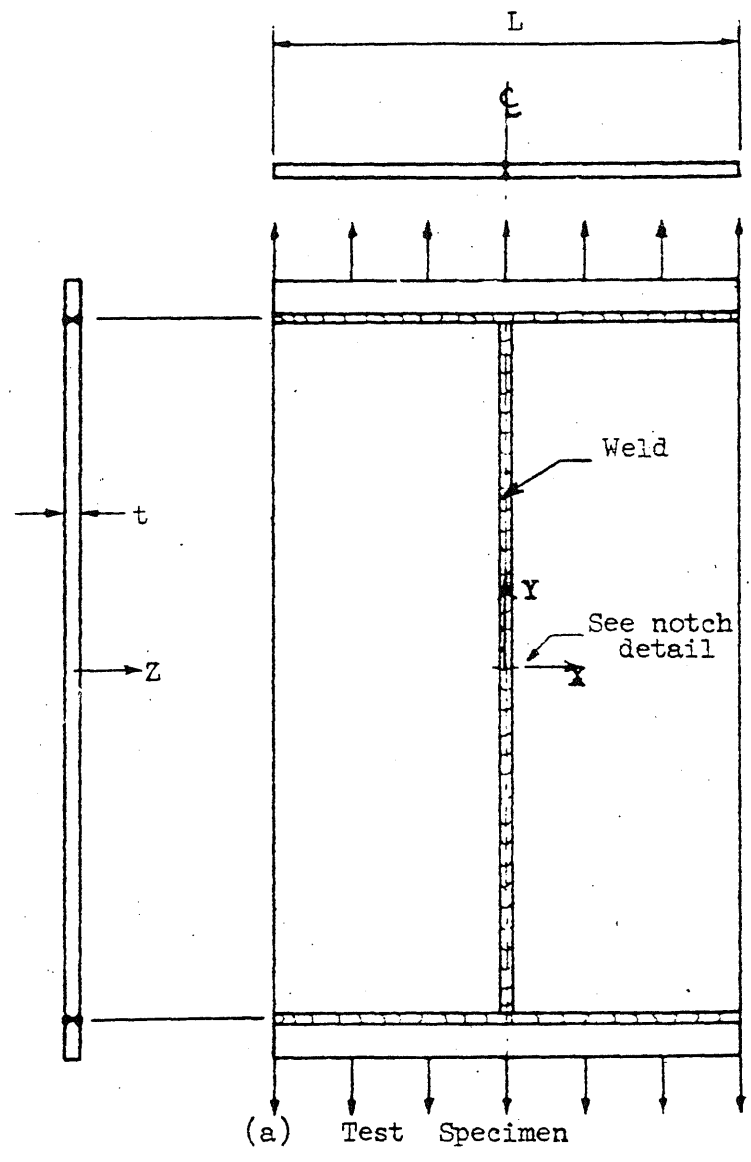


FIG. 3.1 WIDE-PLATE SPECIMEN AND WELLS NOTCH DETAIL

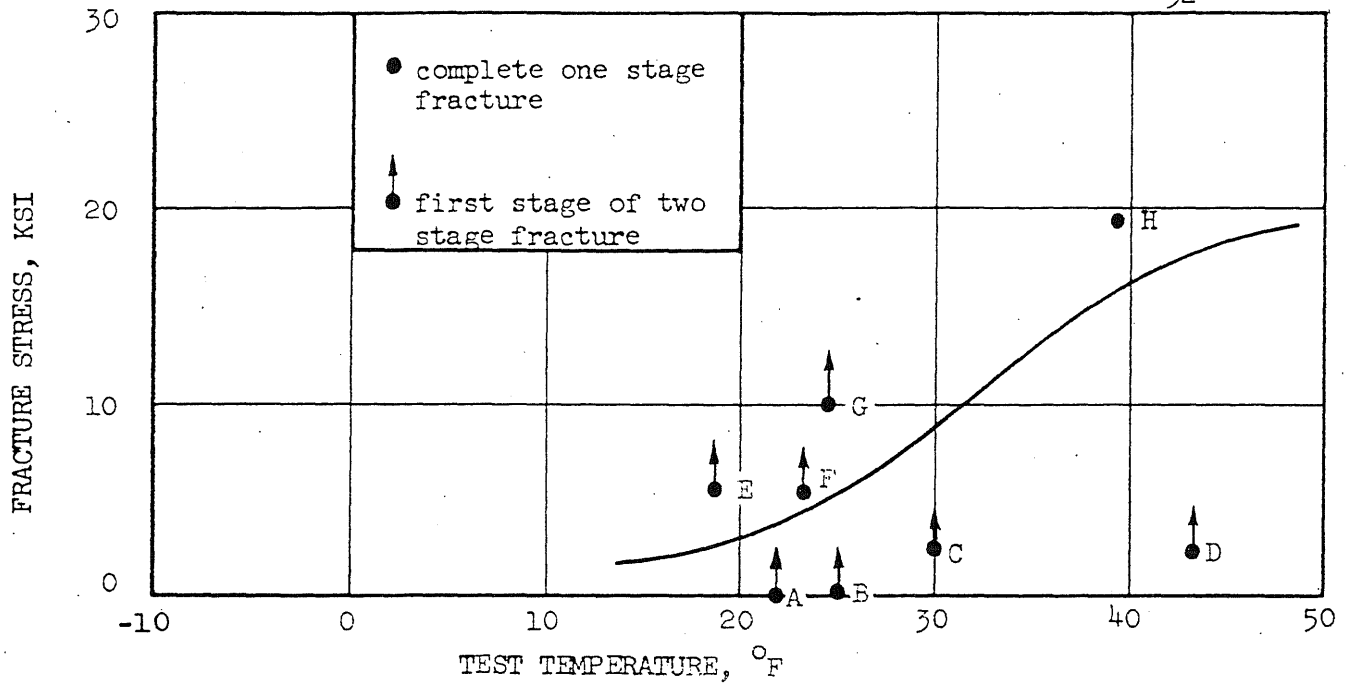


FIG. 3.2 FRACTURE STRESS VERSUS TEST TEMPERATURE, WIDE-PLATE TEST SERIES 1

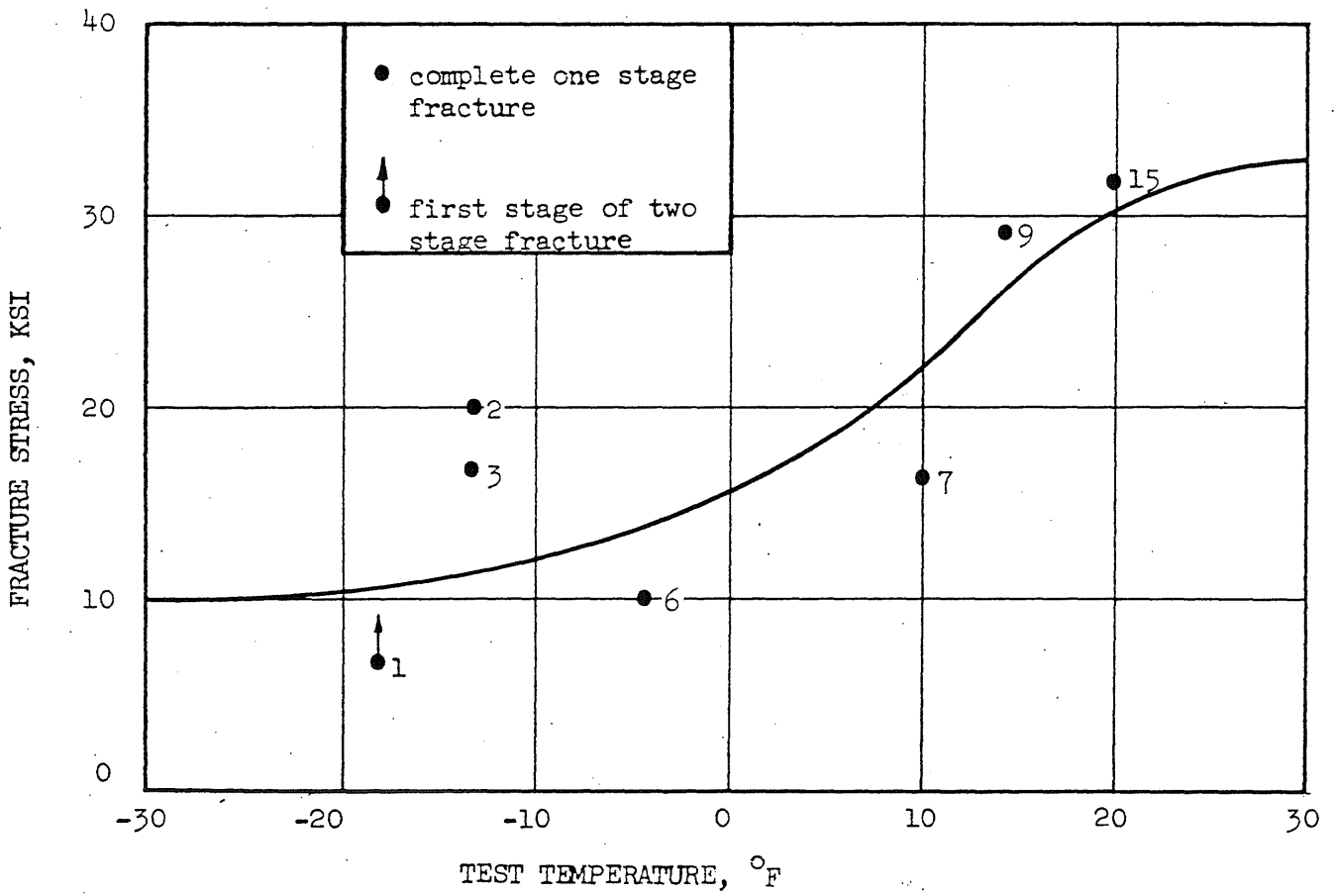


FIG. 3.3 FRACTURE STRESS VERSUS TEST TEMPERATURE, WIDE-PLATE TEST SERIES 2

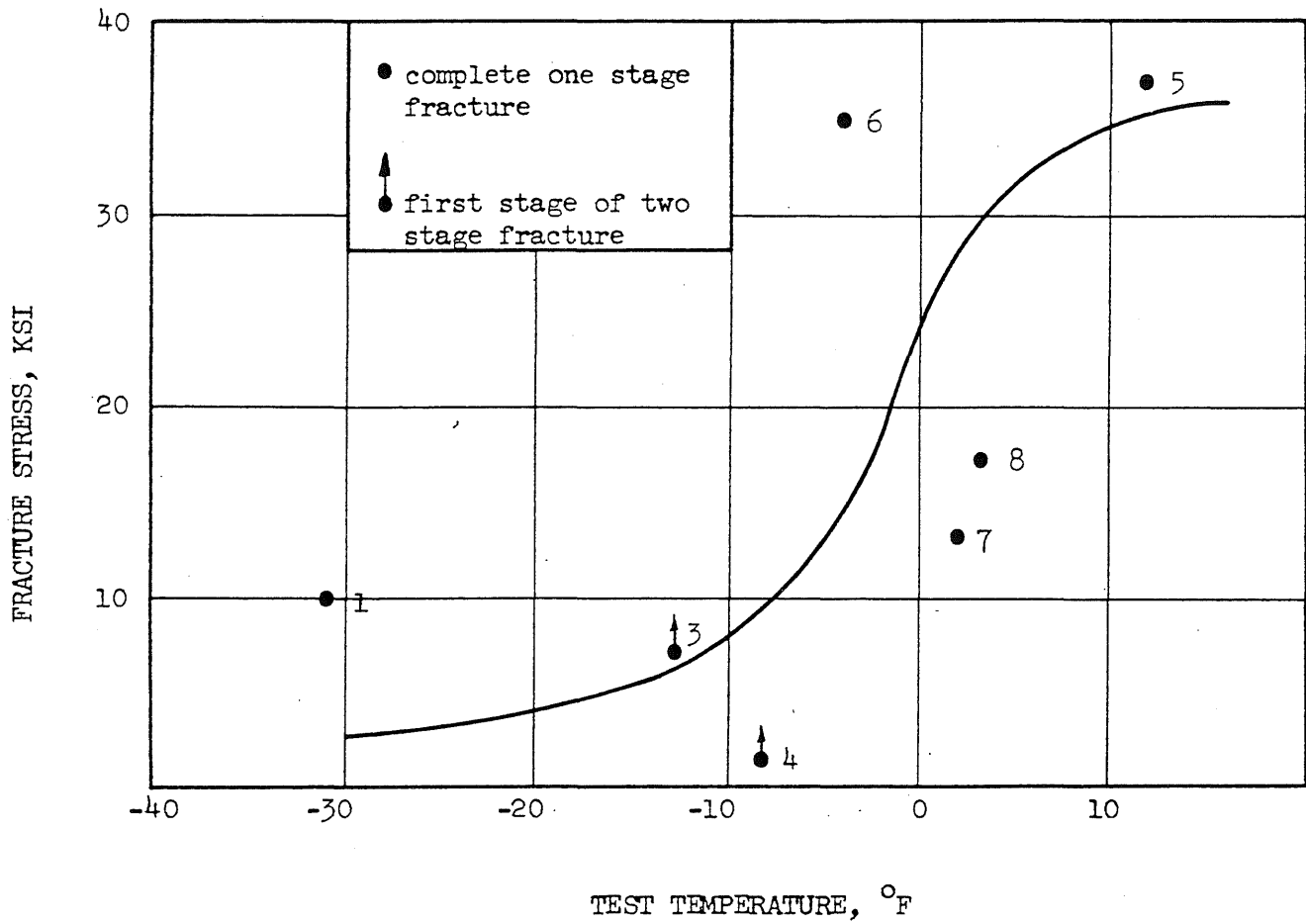


FIG. 3.4 FRACTURE STRESS VERSUS TEST TEMPERATURE, WIDE-PLATE TEST SERIES 3

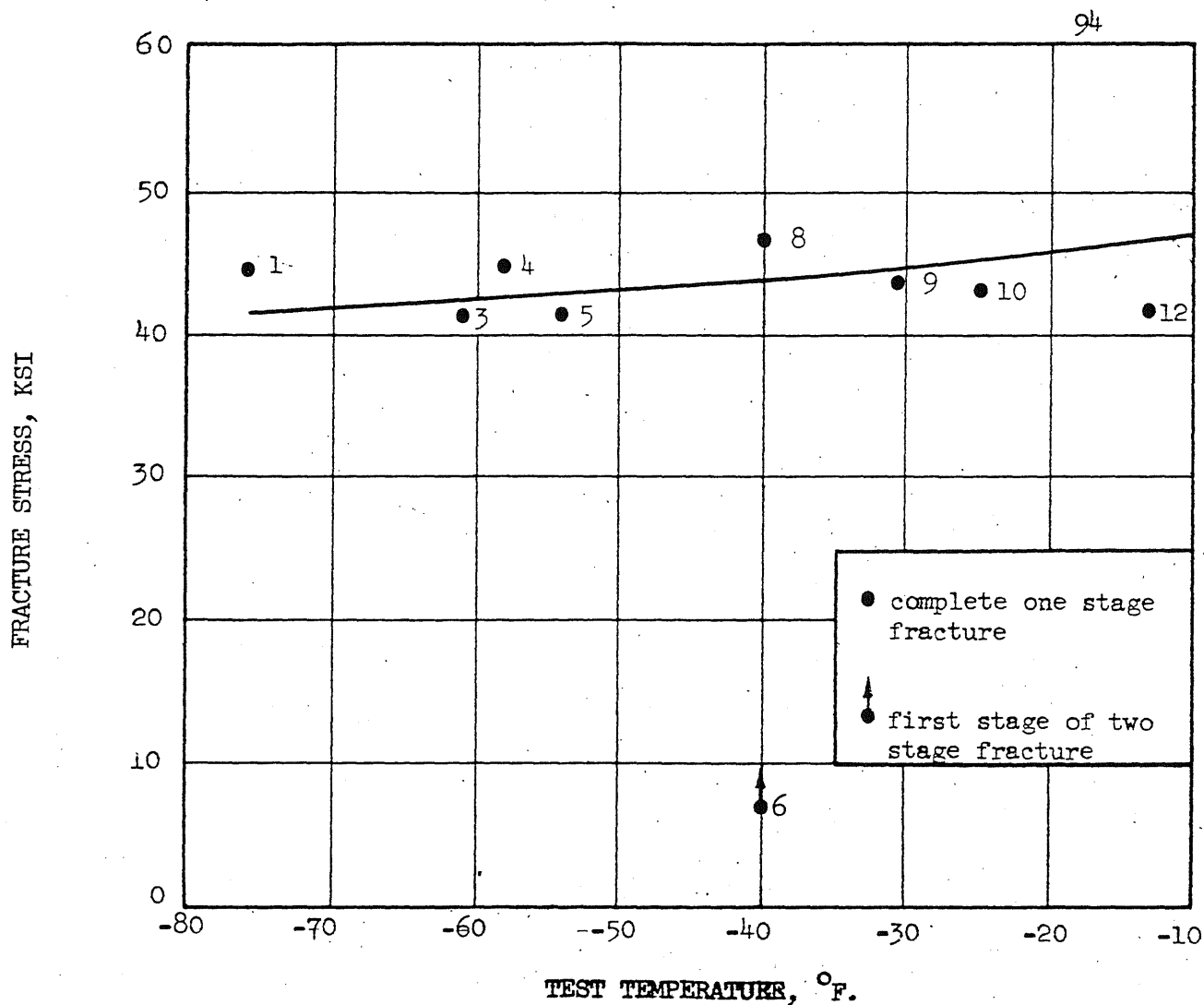


FIG. 3.5 FRACTURE STRESS VERSUS TEST TEMPERATURE, WIDE-PLATE TEST SERIES 4

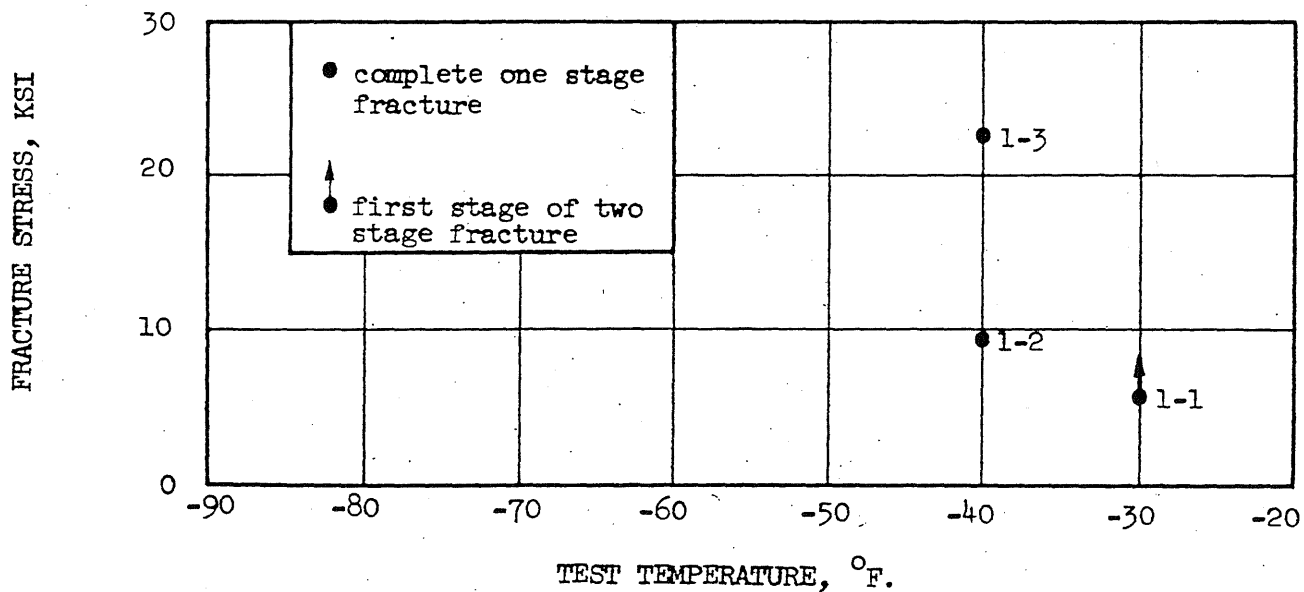


FIG. 3.6 FRACTURE STRESS VERSUS TEST TEMPERATURE, WIDE-PLATE TEST SERIES 5

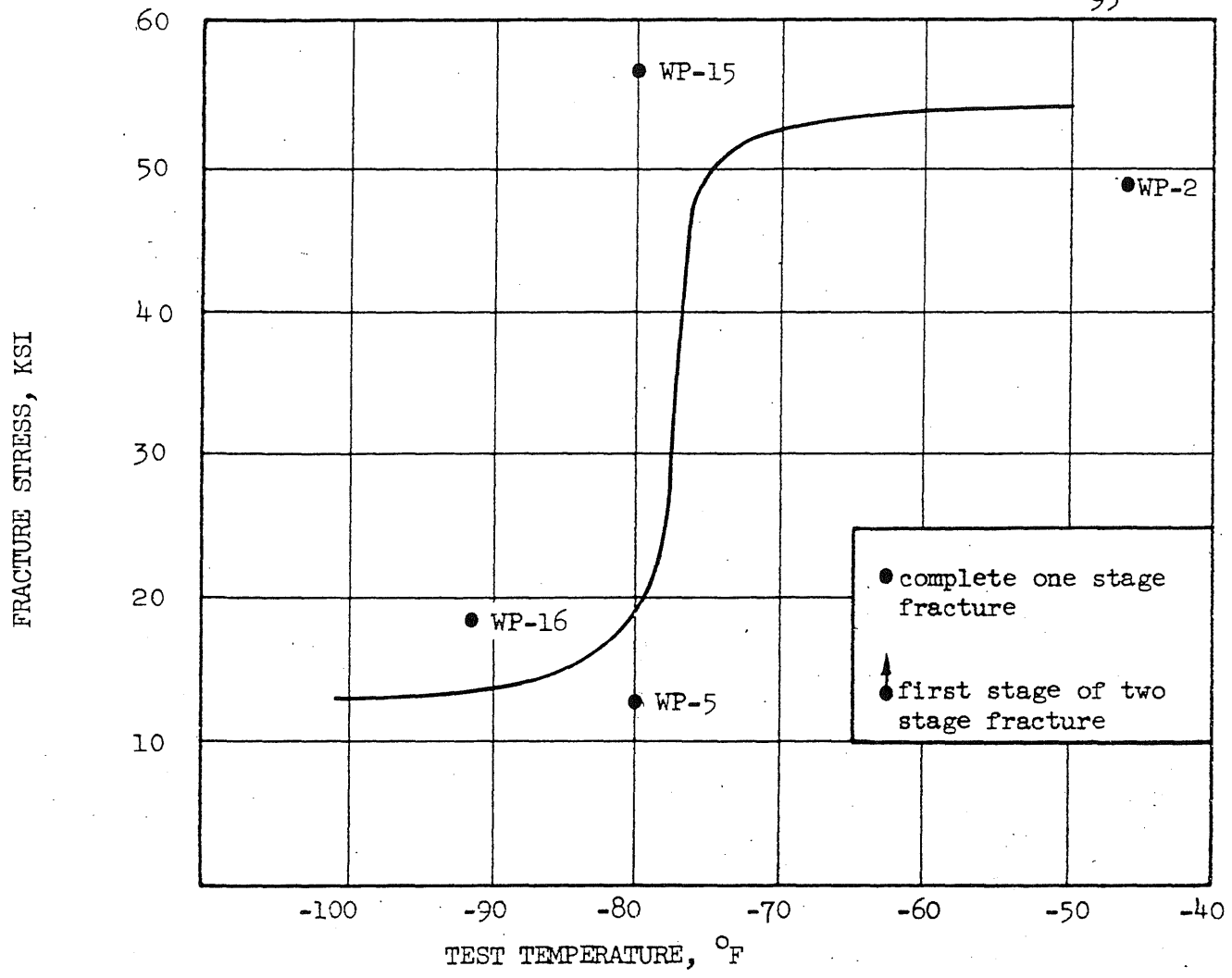


FIG. 3.7 FRACTURE STRESS VERSUS TEST TEMPERATURE, WIDE-PLATE TEST SERIES (6a)

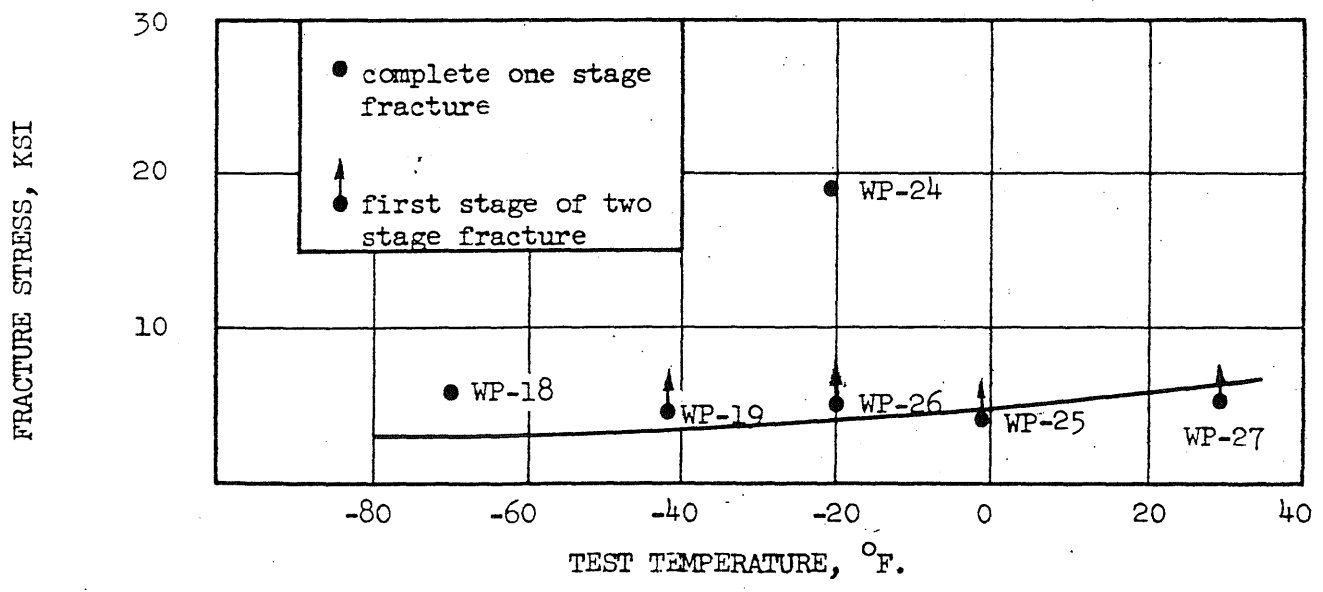


FIG. 3.8 FRACTURE STRESS VERSUS TEST TEMPERATURE, WIDE-PLATE TEST SERIES (6b)

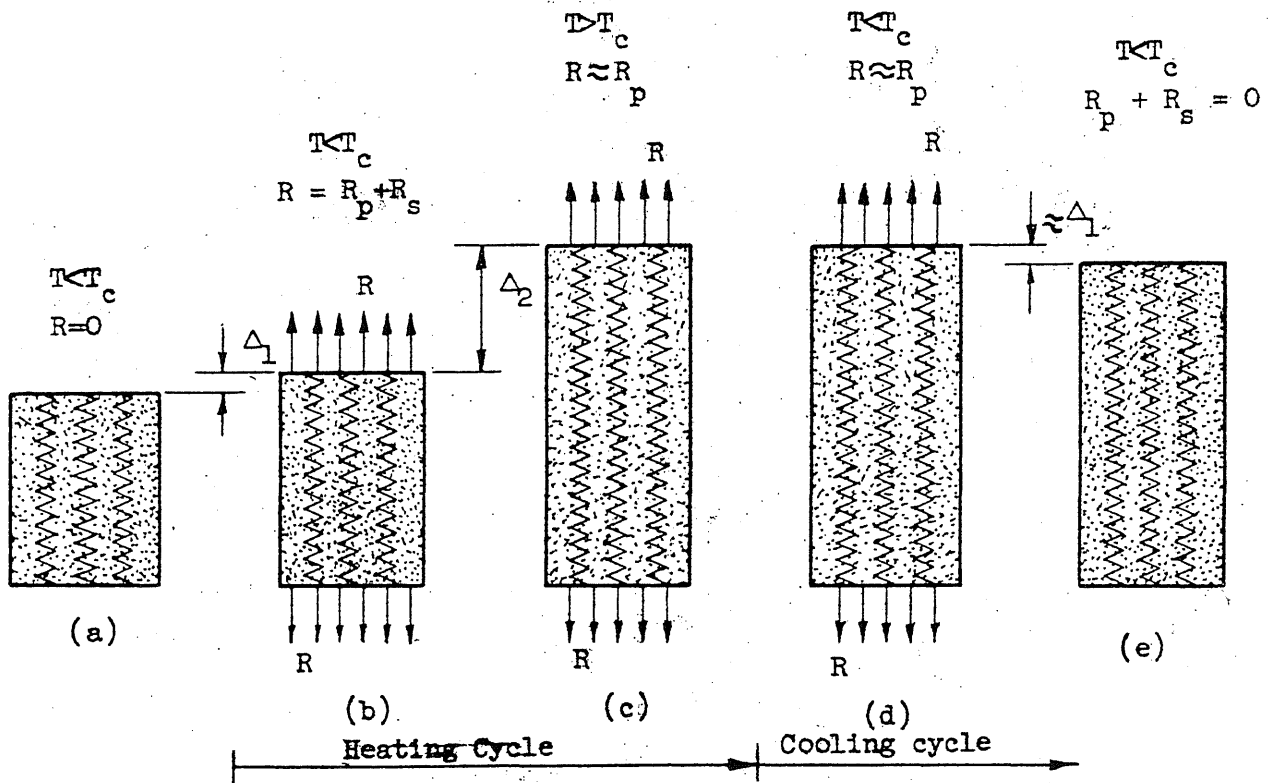
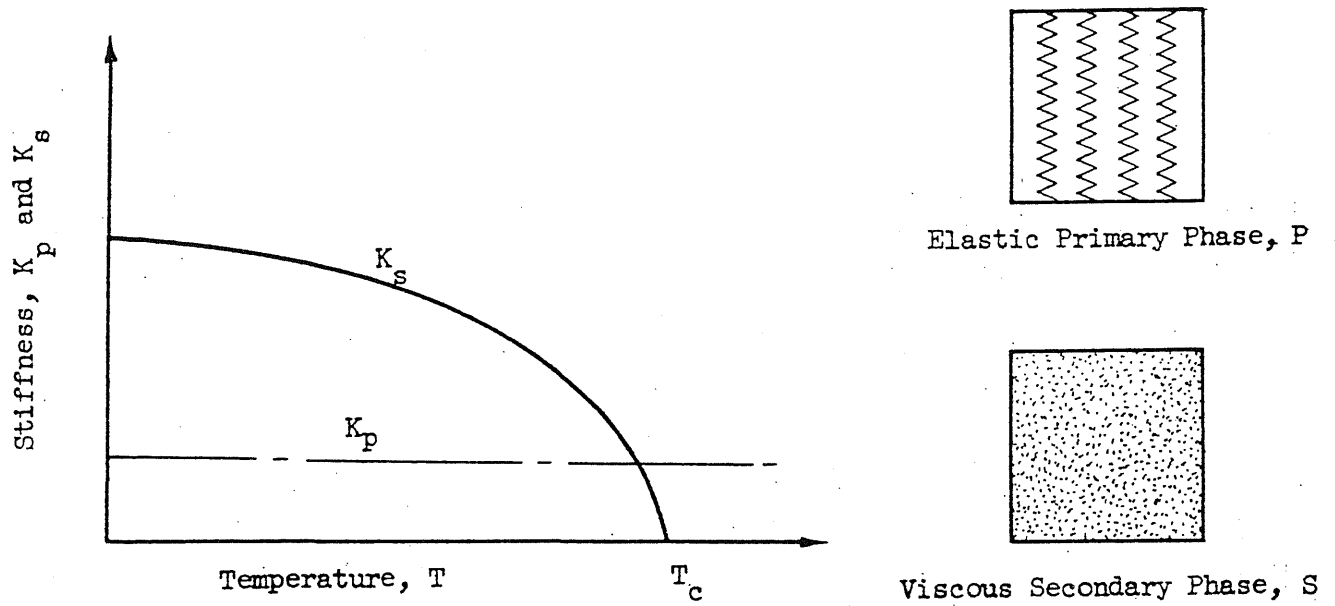


FIG. 4.1 TWO-PHASE MODEL ILLUSTRATING ACCOMPLISHMENT OF STRESS FREEZING

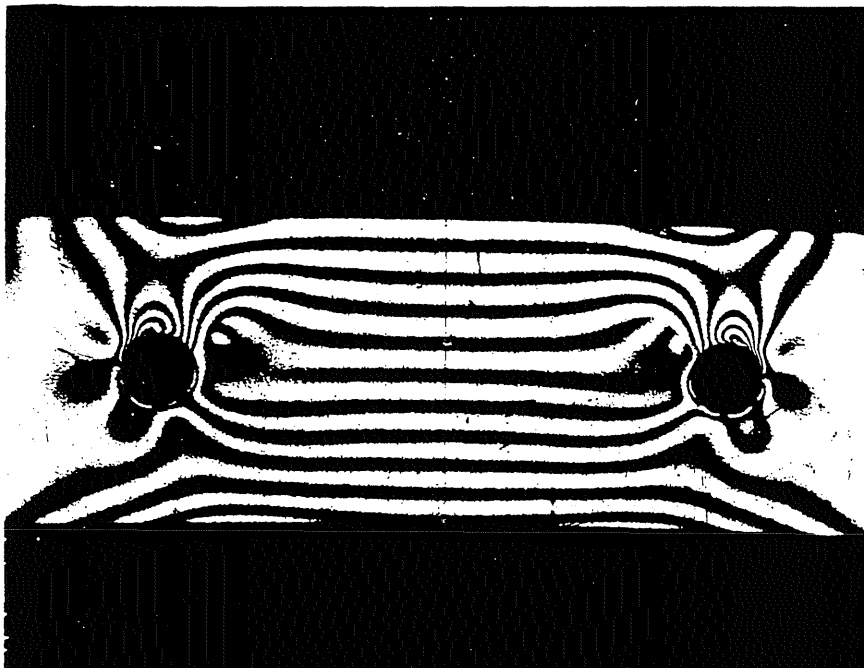


FIG. 4.2 ISOCHROMATIC FRINGE PHOTOGRAPH OF CALIBRATION
BEAM INTO WHICH STRESSES HAVE BEEN FROZEN

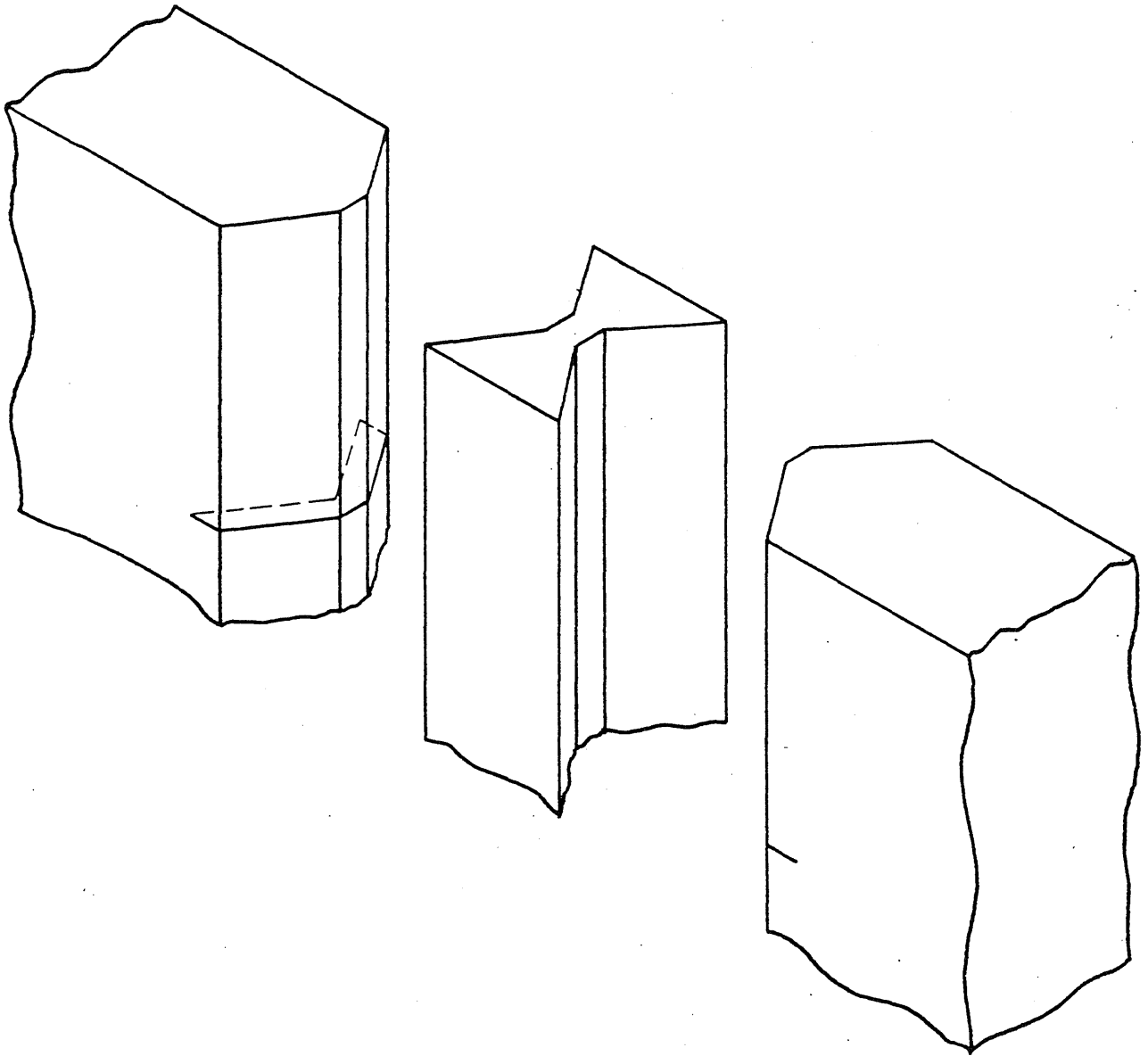


FIG. 4.3 UNASSEMBLED COMPONENTS OF EPOXY MODEL OF WELLS NOTCH

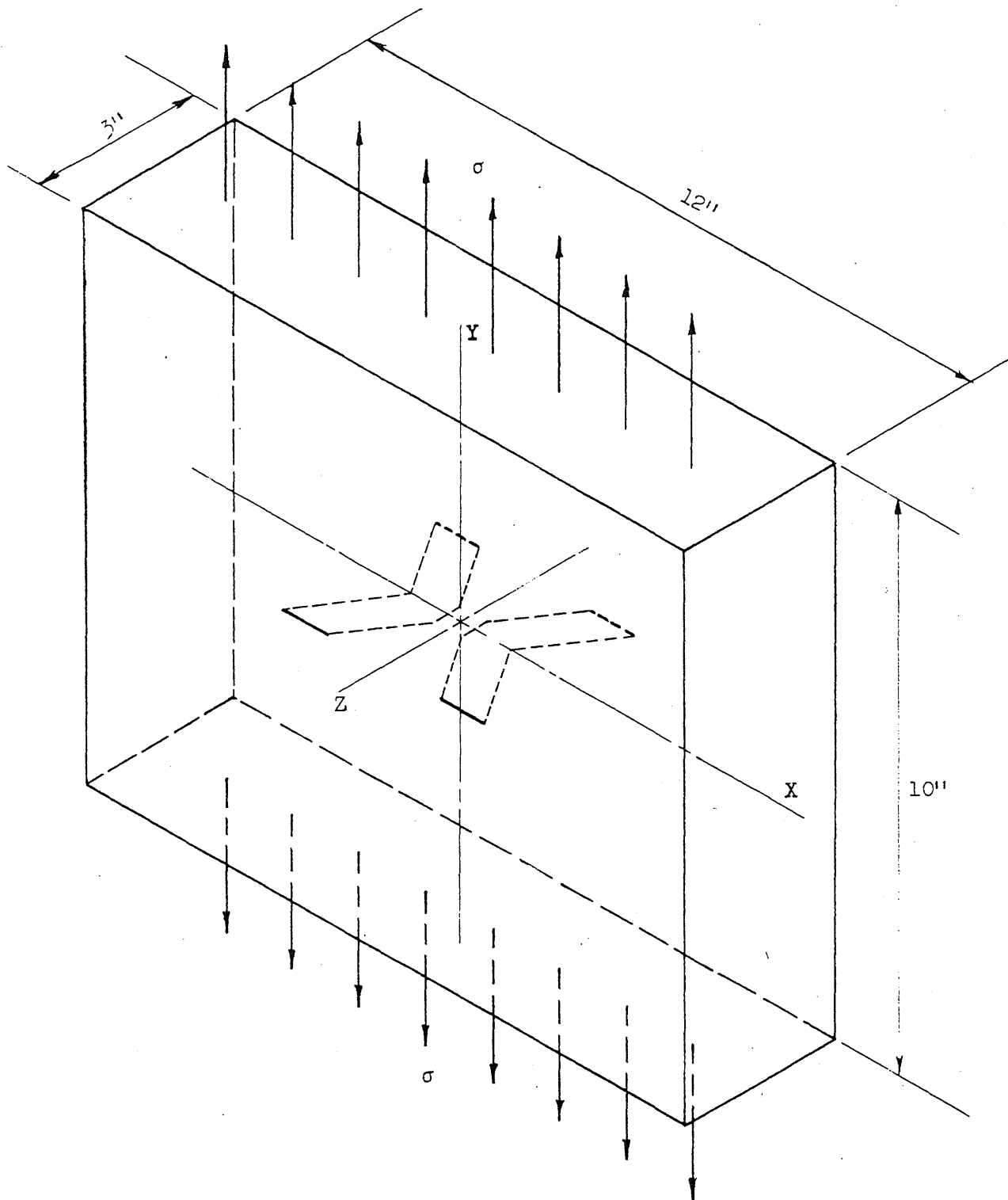


FIG. 4.4 EPOXY MODEL OF WELLS-TYPE NOTCH

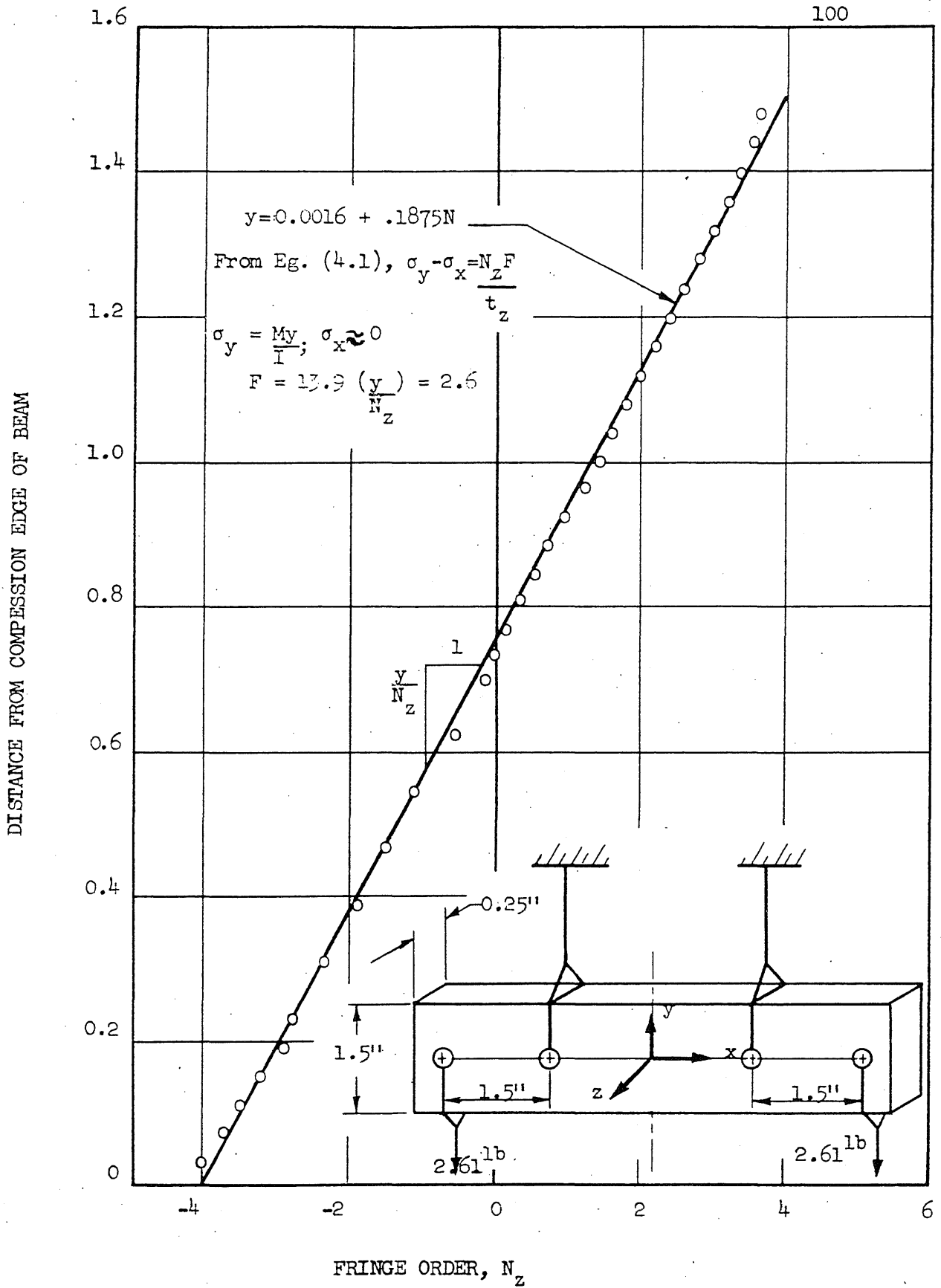


FIG. 4.5 BEAM CALIBRATION SPECIMEN AND CURVE FOR DETERMINATION OF STRESS-OPTICAL CONSTANT, F .

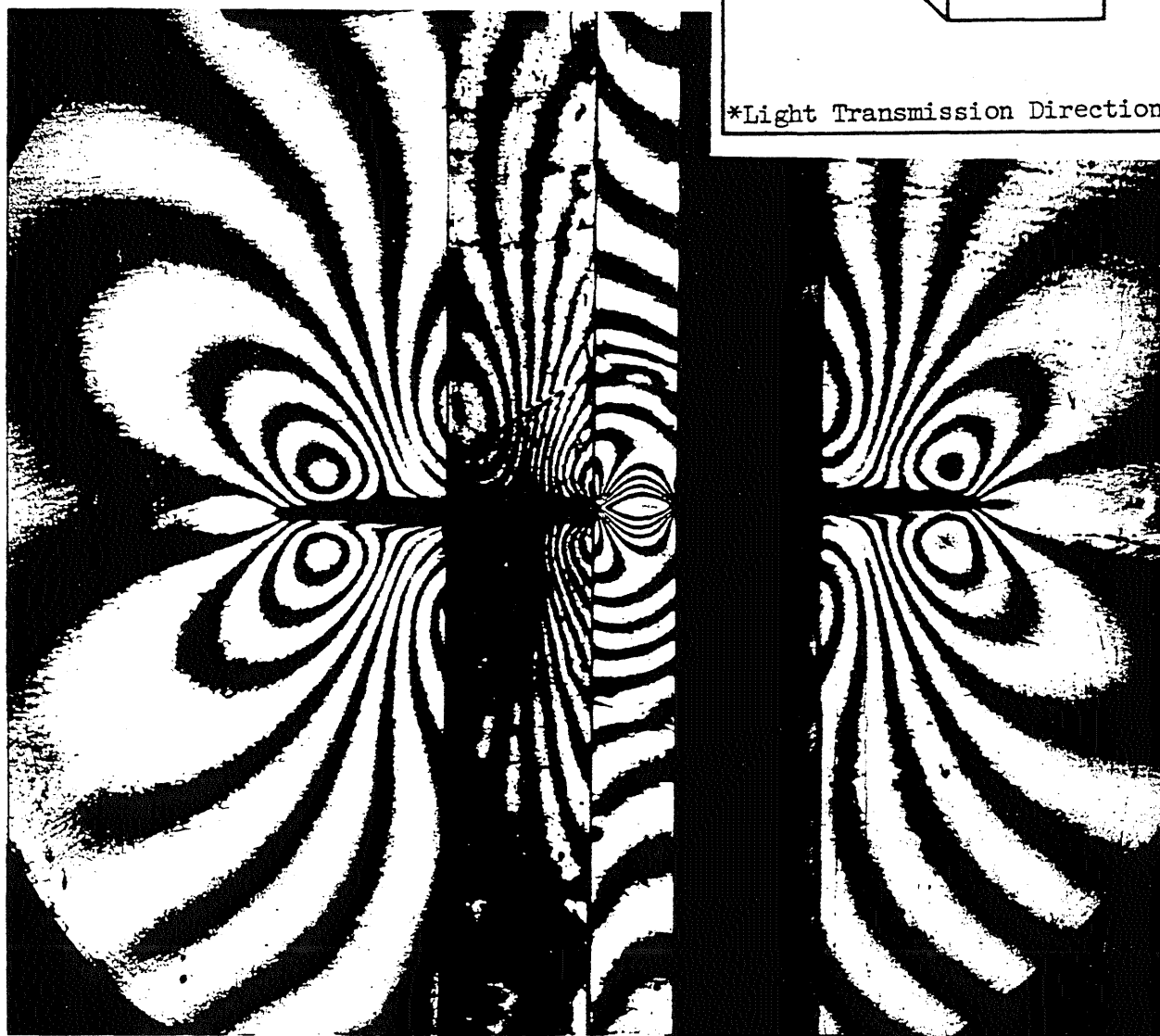
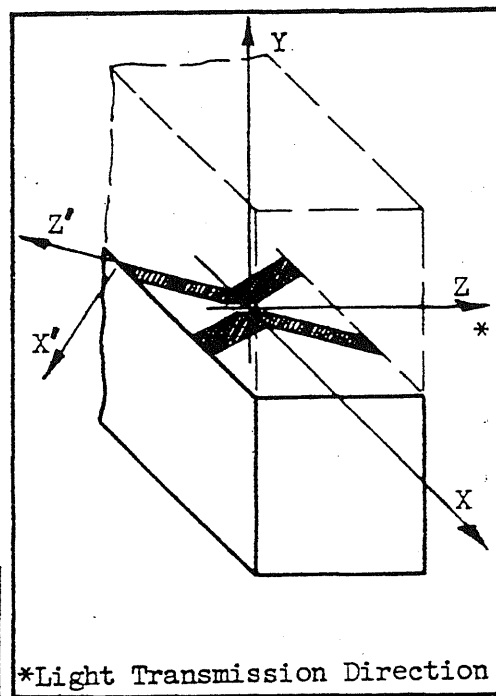


FIG. 4.6 ISOCHROMATIC FRINGE PHOTOGRAPH OF UNSLICED MODEL; $m = 1$

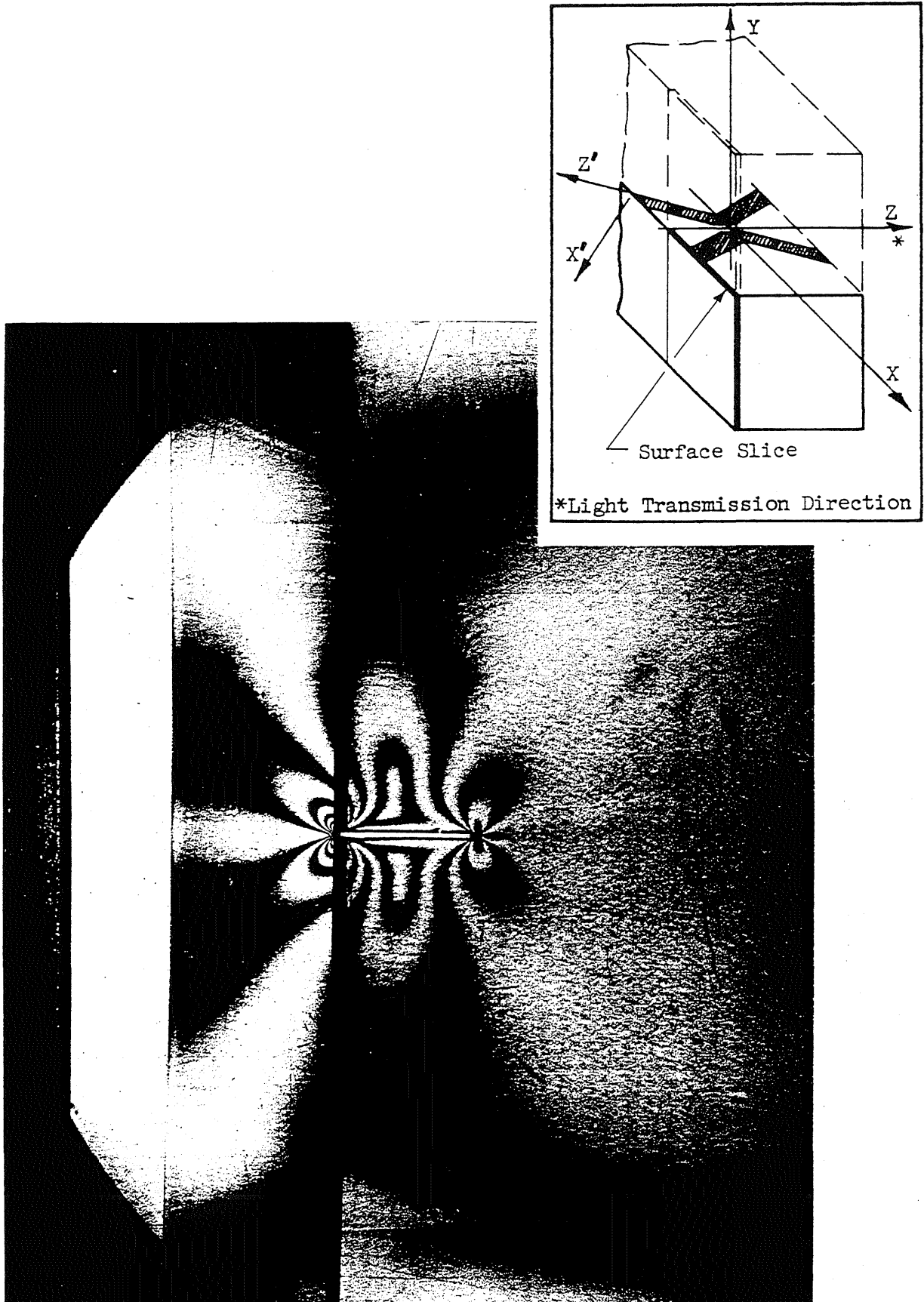


FIG. 4.7 ISOCHROMATIC FRINGE PHOTOGRAPH OF SURFACE SLICE OF MODEL; $m = 3$.

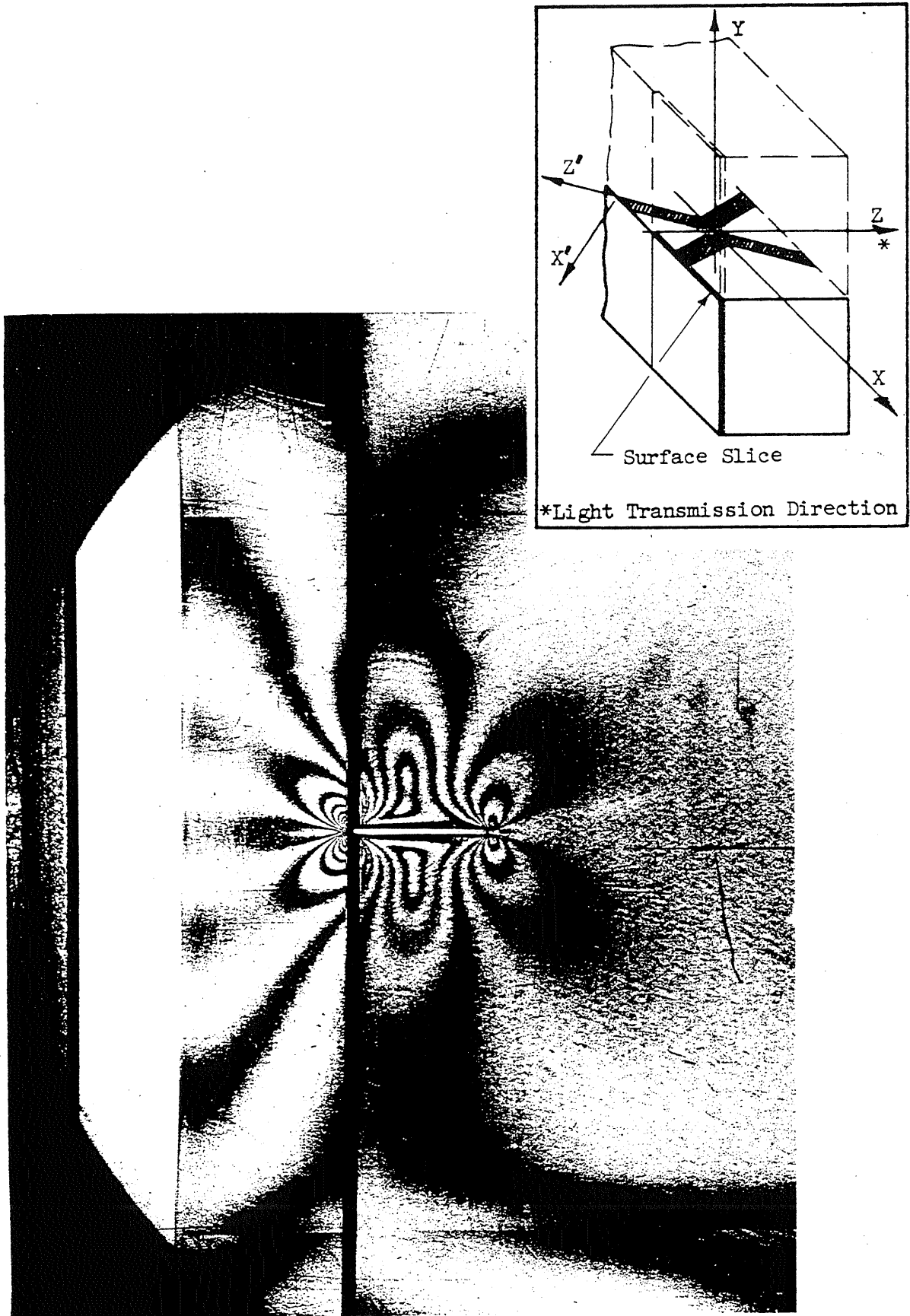


FIG. 4.8 ISOCHROMATIC FRINGE PHOTOGRAPH OF SURFACE SLICE OF MODEL; $m = 5$

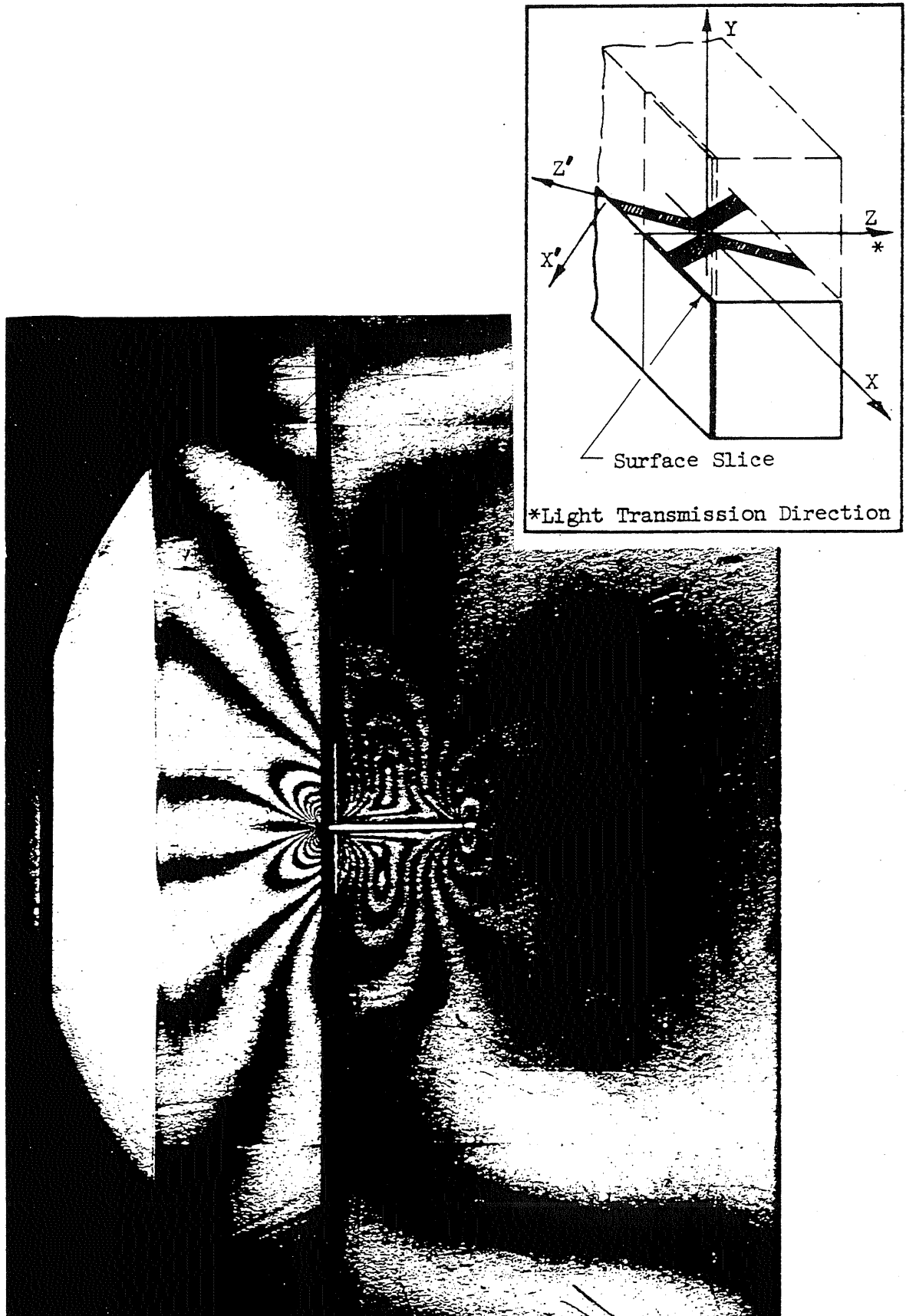


FIG. 4.9 ISOCHROMATIC FRINGE PHOTOGRAPH OF SURFACE SLICE OF MODEL; $m = 7$

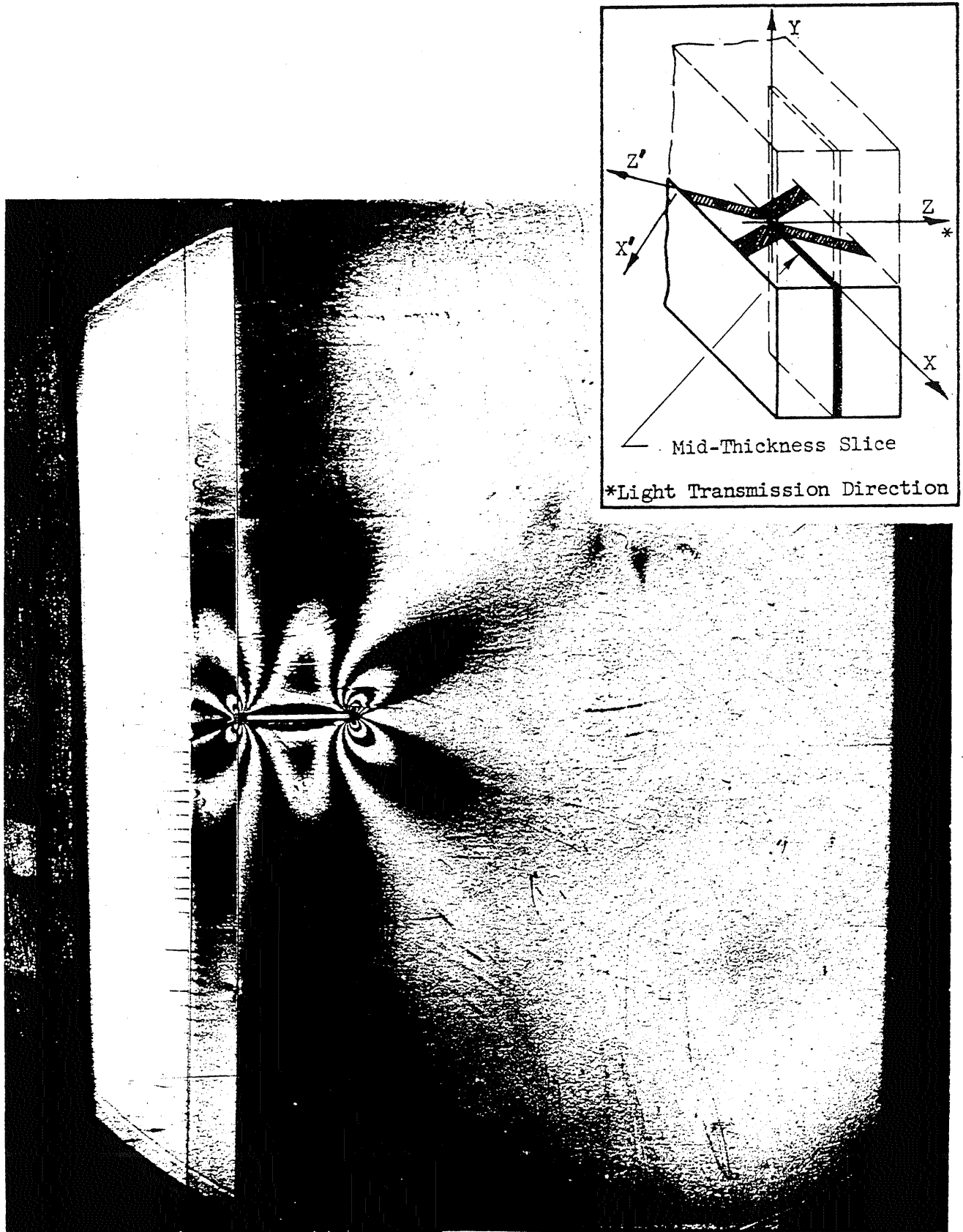


FIG. 4.10 ISOCHROMATIC FRINGE PHOTOGRAPH OF MID-THICKNESS SLICE OF MODEL; $m = 3$

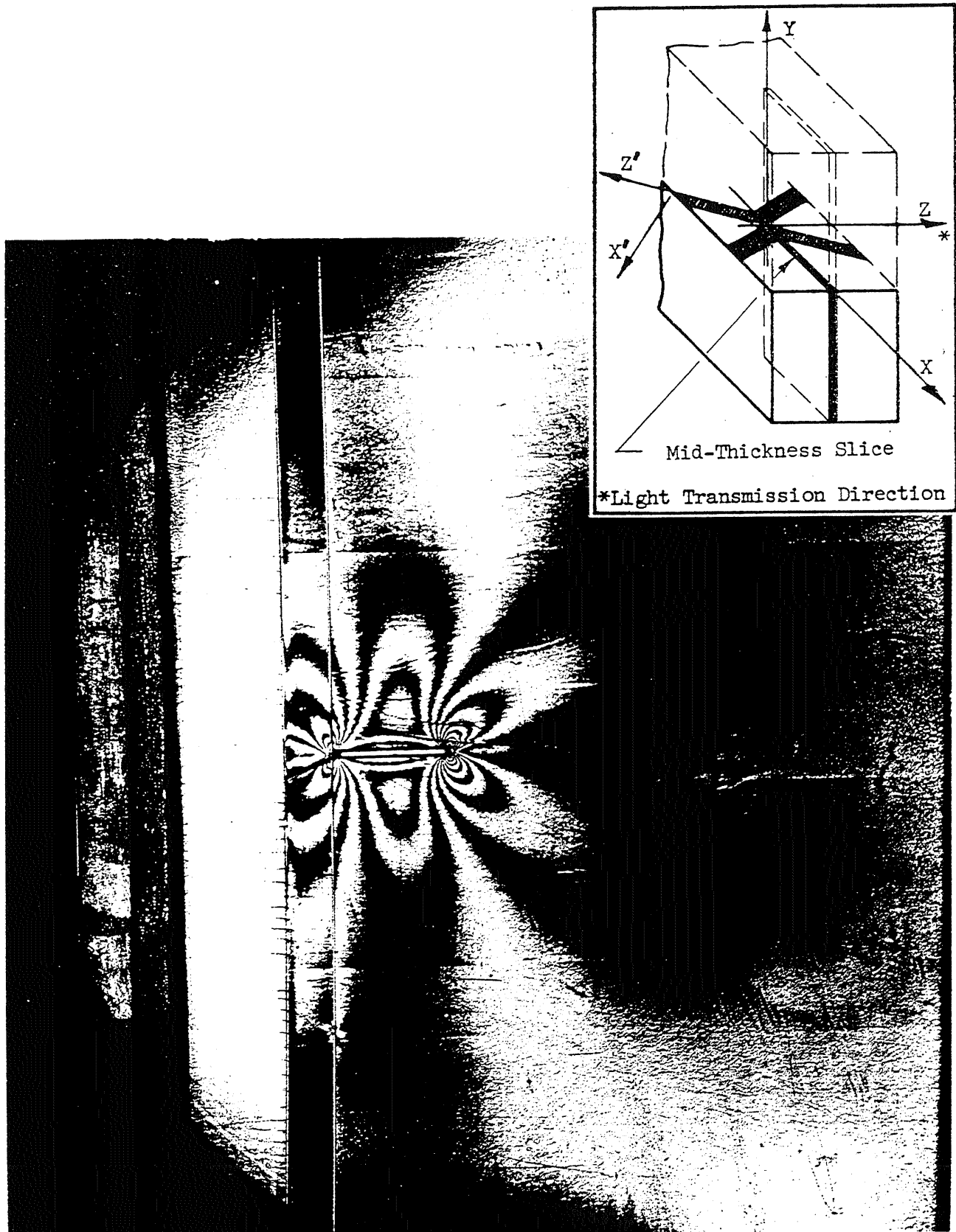


FIG. 4.11 ISOCHROMATIC FRINGE PHOTOGRAPH OF MID-THICKNESS SLICE OF MODEL; $m = 5$

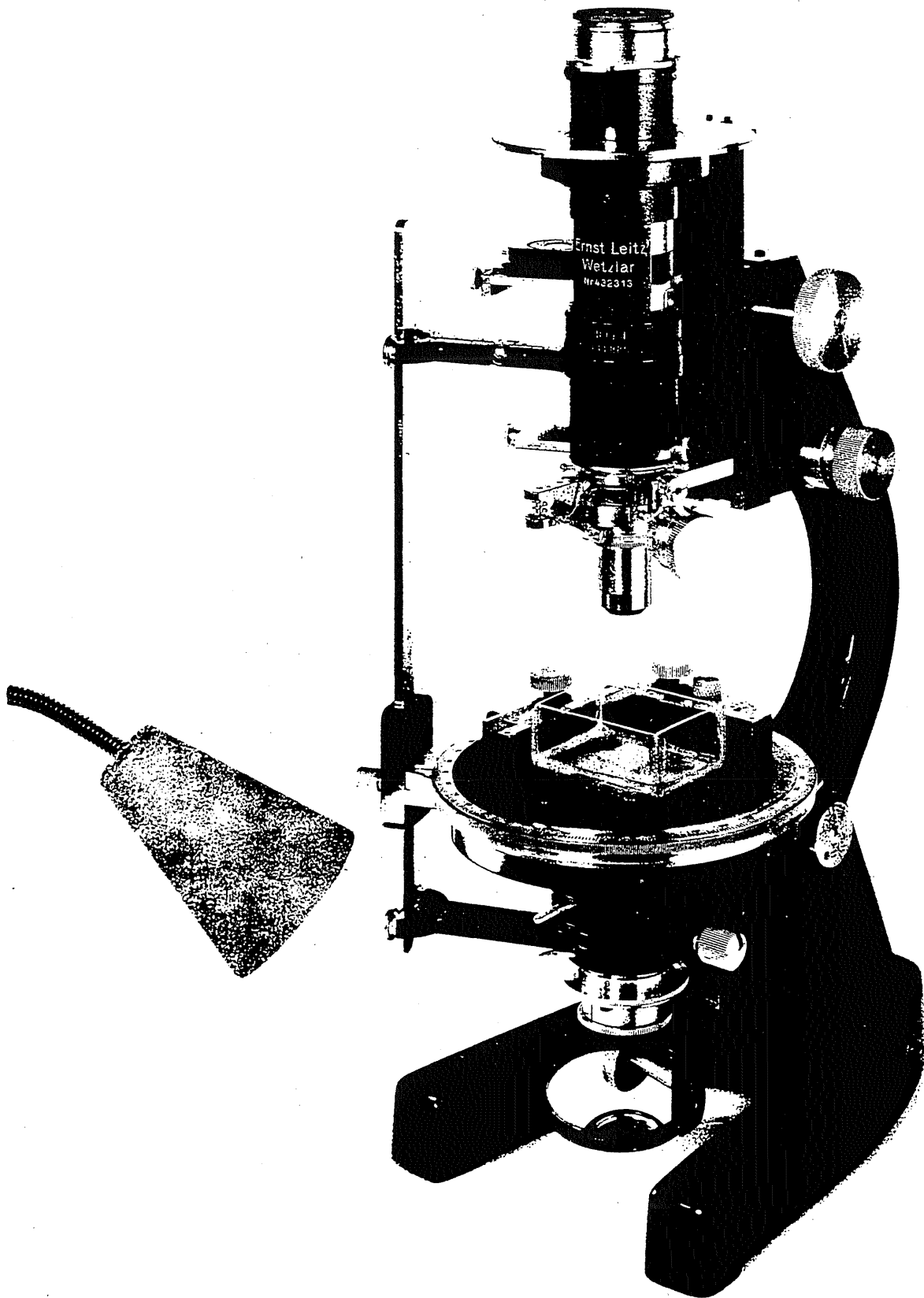
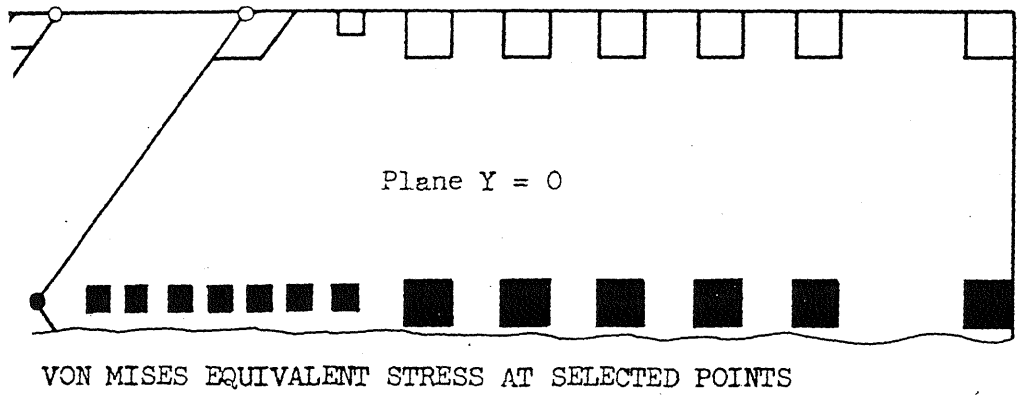
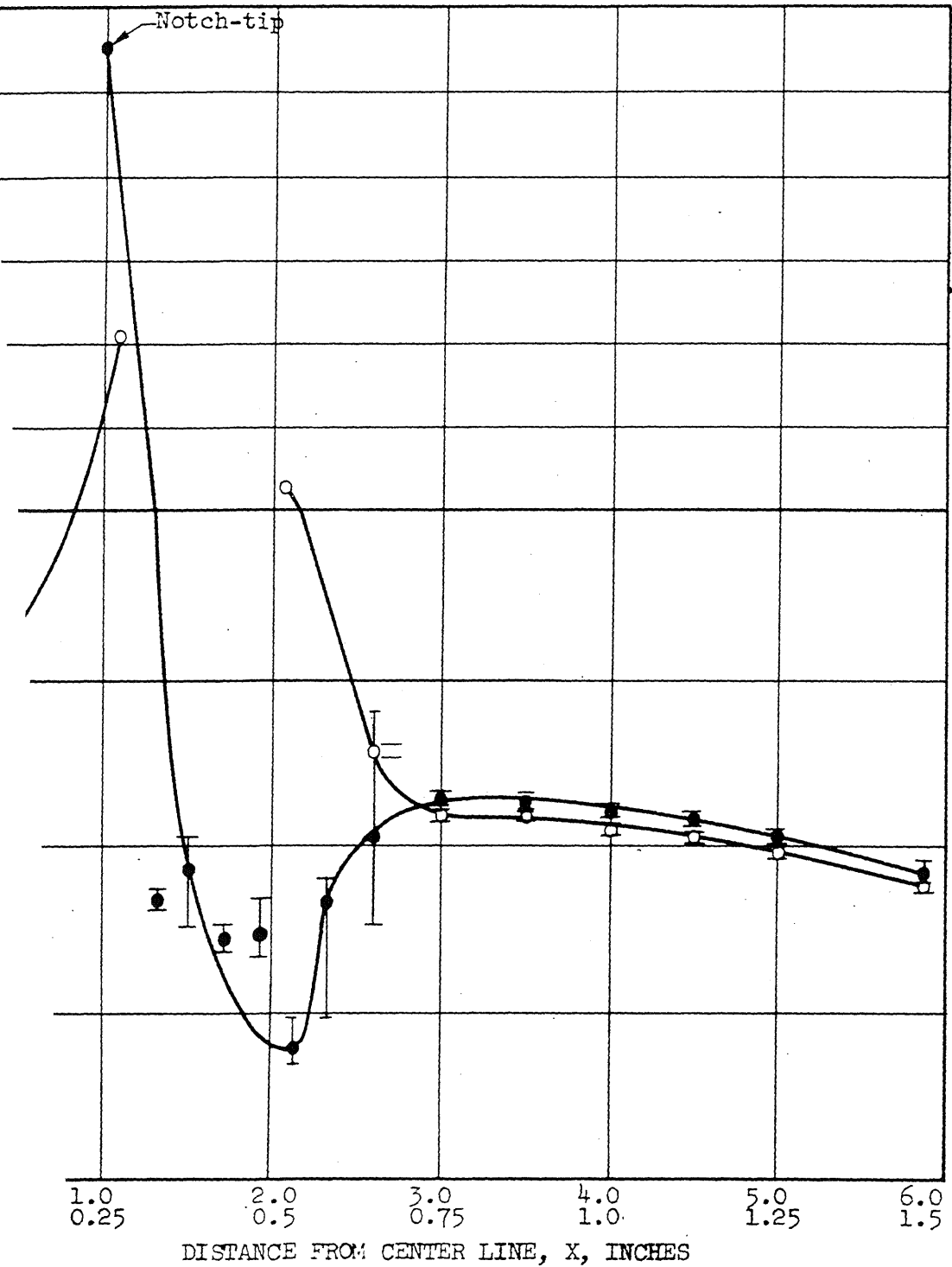


FIG. 4.12 PHOTOGRAPH OF POLARIZING MICROSCOPE



VON MISES EQUIVALENT STRESS AT SELECTED POINTS

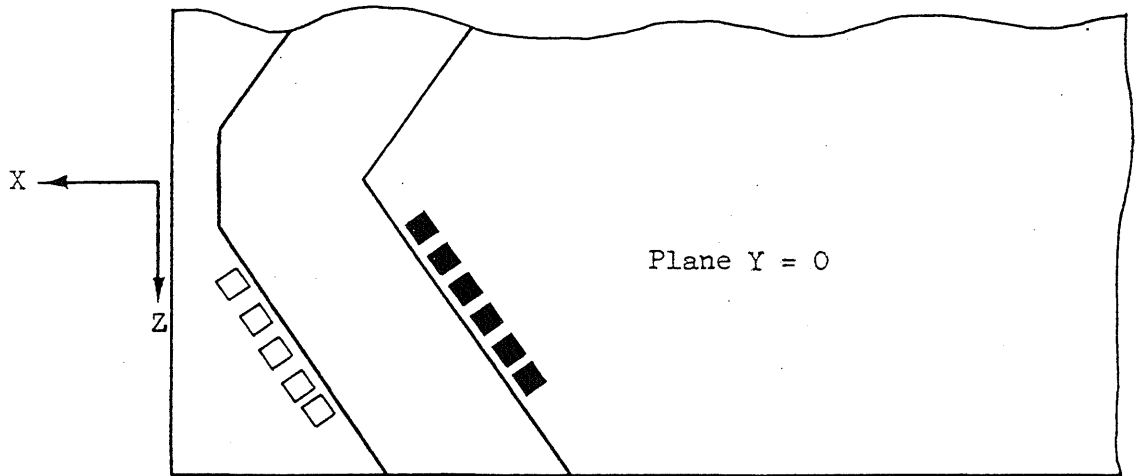
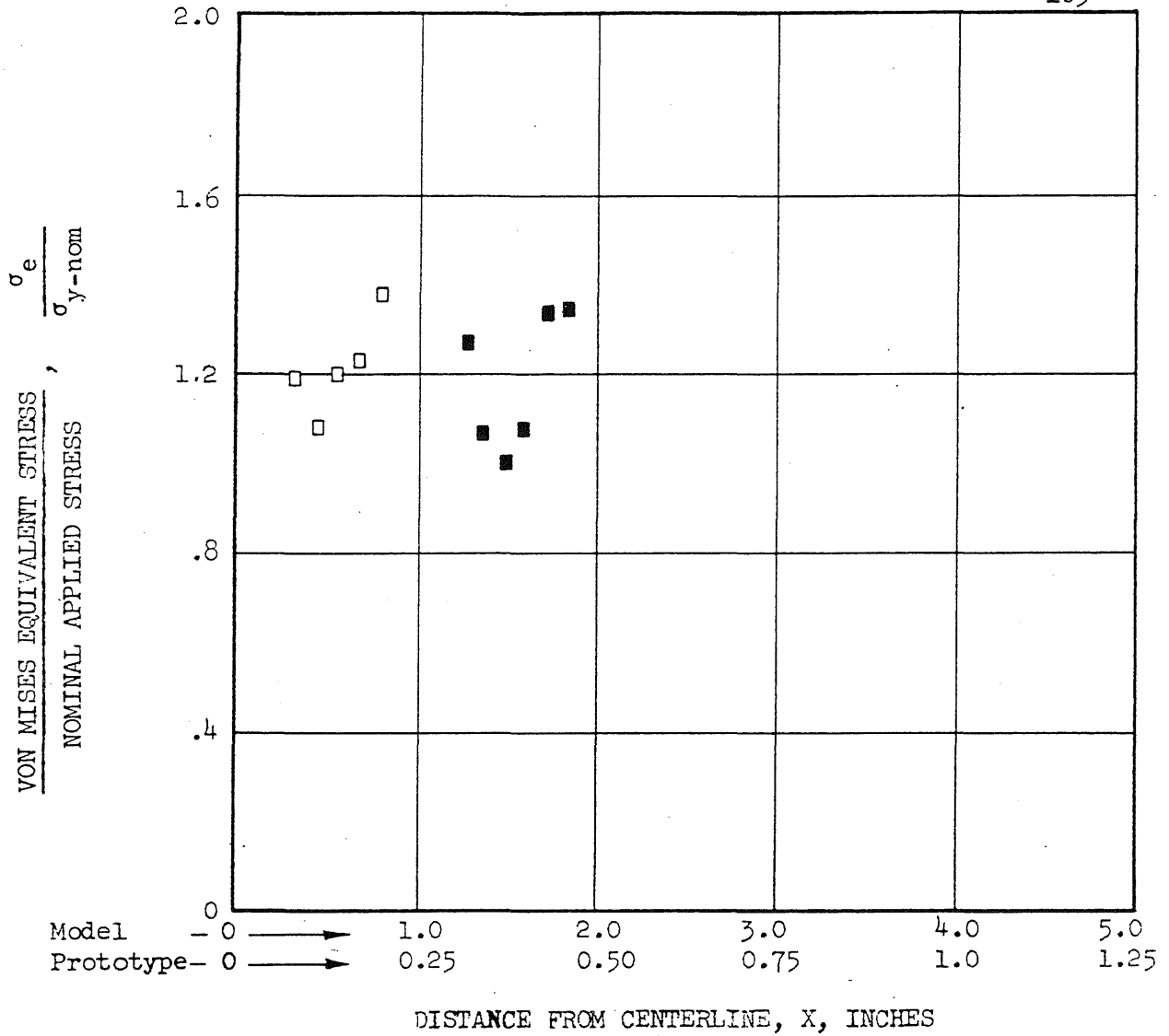


FIG. 4.14 VON MISES EQUIVALENT STRESS AT SELECTED LOCATIONS ON NOTCH PERIMETER

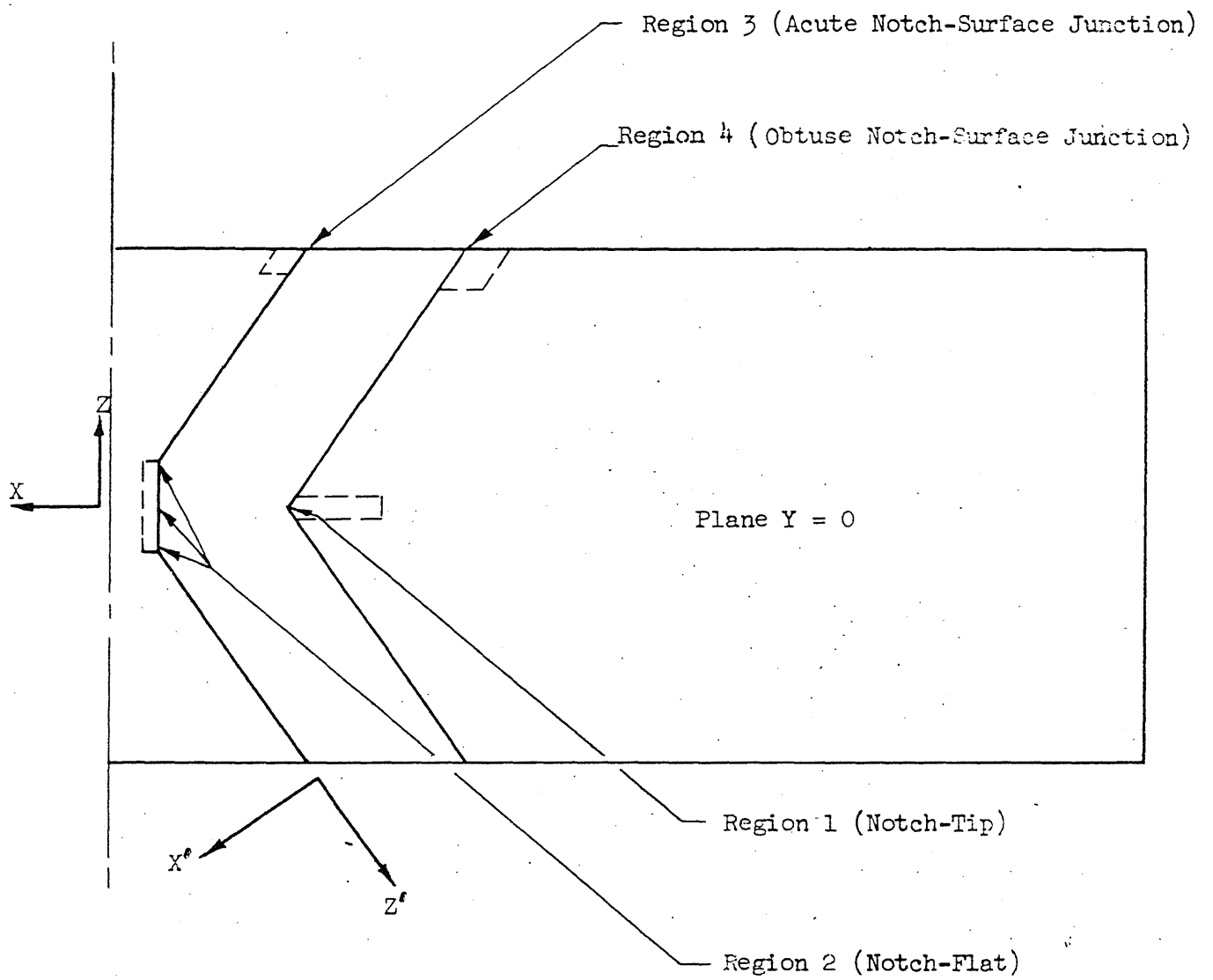


FIG. 4.15 REGIONS FOR WHICH BOUNDARY STRESSES, σ_y , ARE DETERMINED

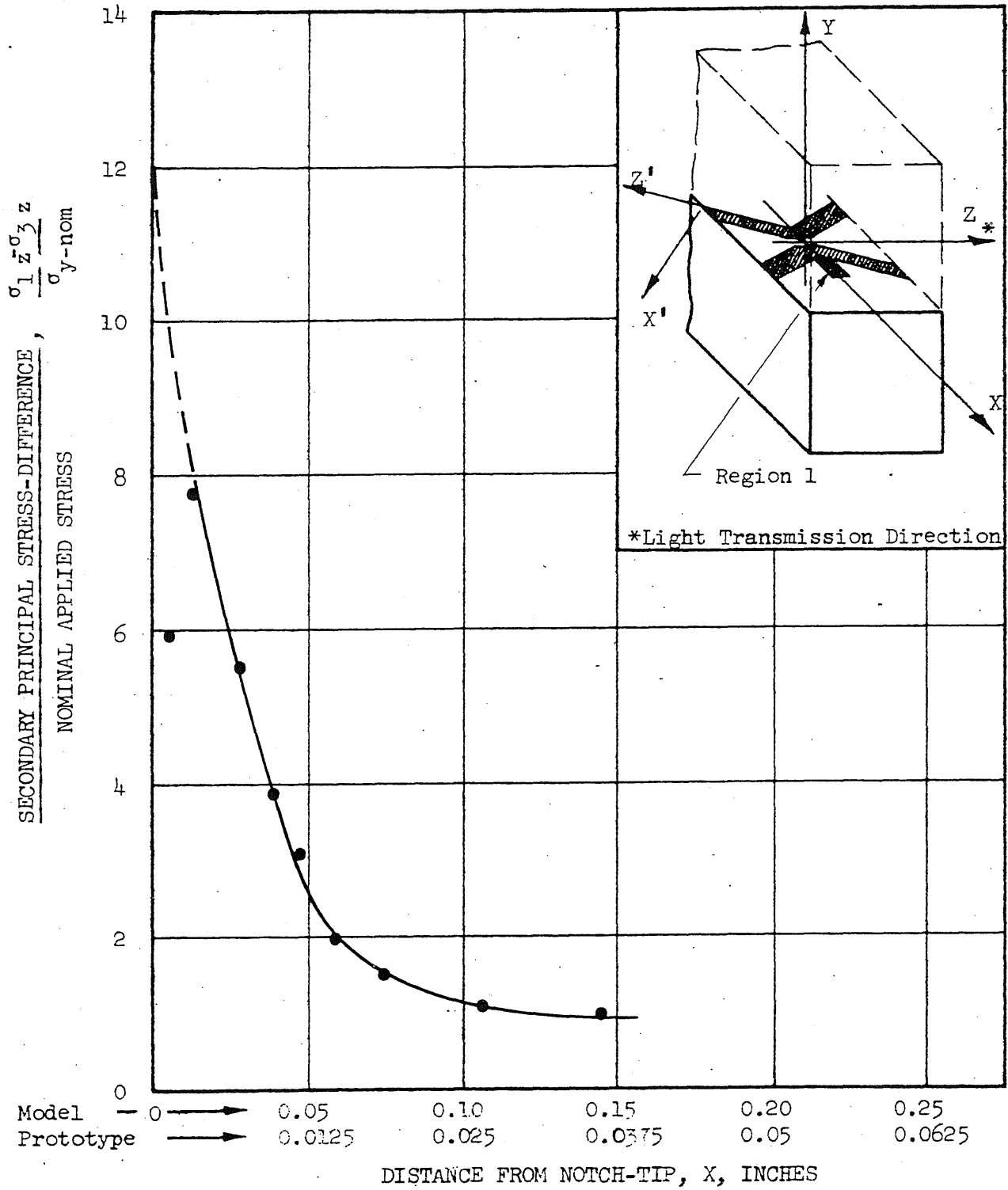


FIG. 4.16 SECONDARY PRINCIPAL STRESS-DIFFERENCE, $\sigma_1 z - \sigma_3 z$, IN VICINITY OF NOTCH-TIP: REGION 1

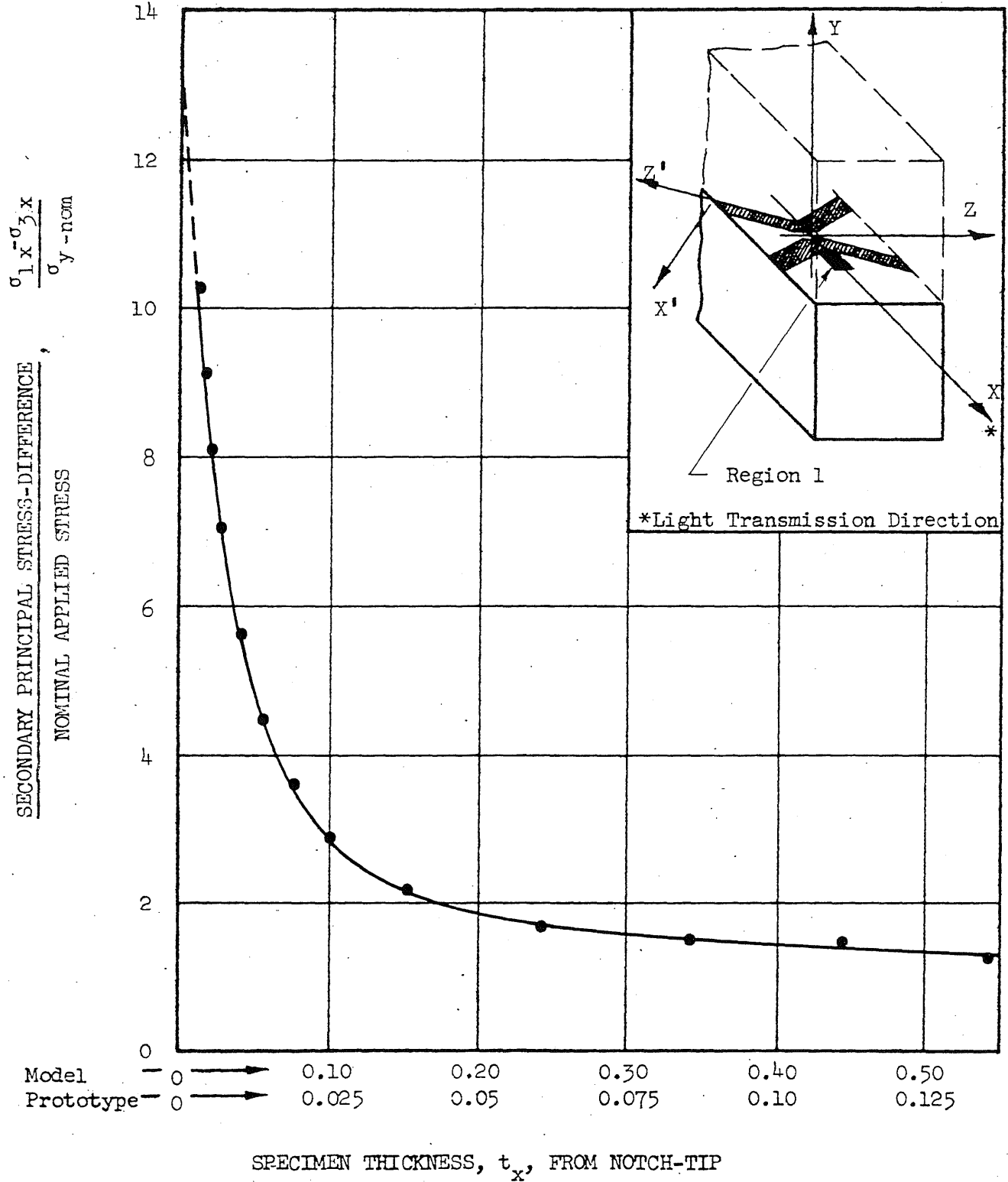


FIG. 4.17 SECONDARY PRINCIPAL STRESS-DIFFERENCE, $\sigma_{1x} - \sigma_{3x}$, IN VICINITY OF NOTCH-TIP: REGION 1

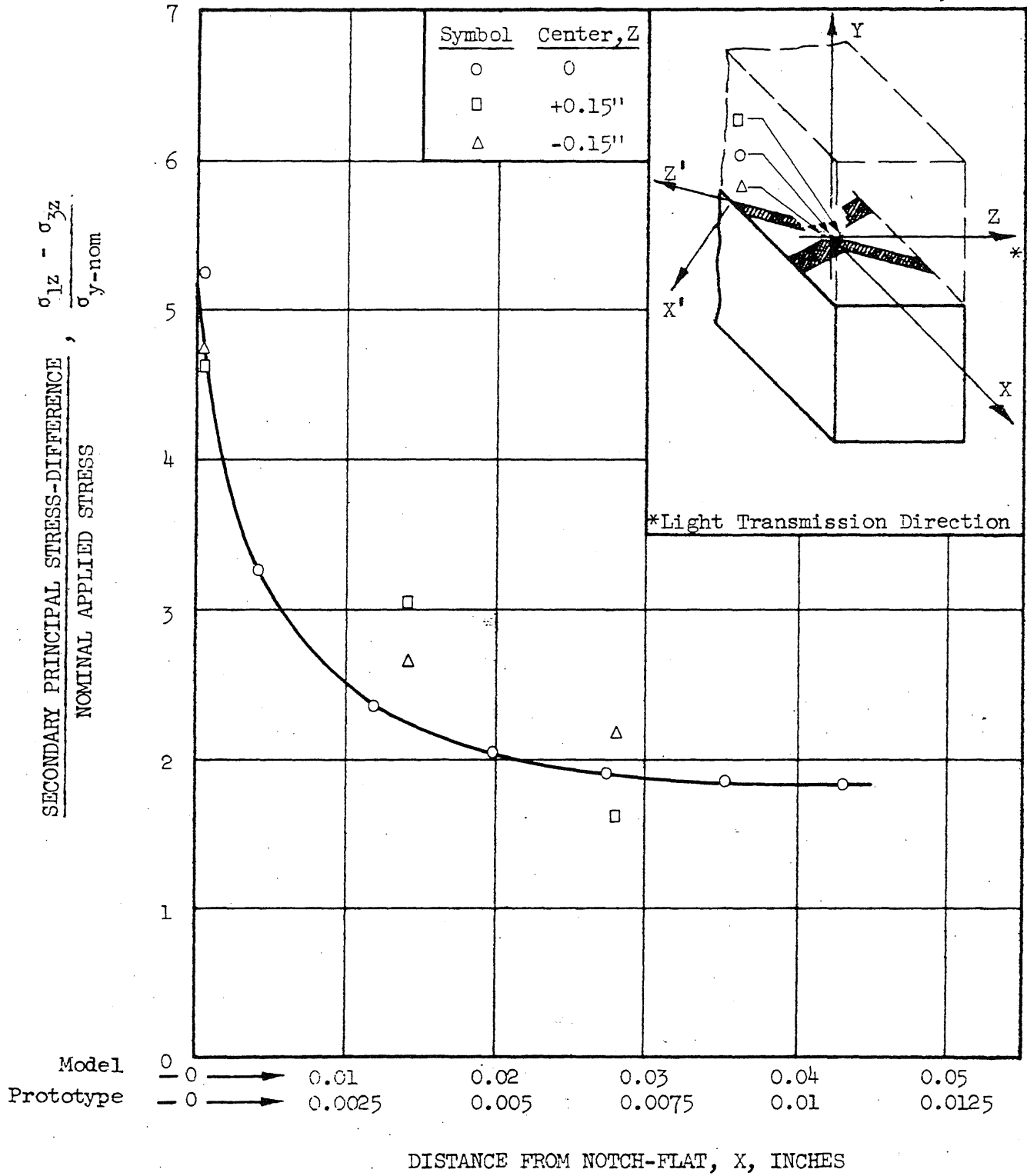


FIG. 4.18 SECONDARY PRINCIPAL STRESS-DIFFERENCE, $\sigma_{1z} - \sigma_{3z}$, IN VICINITY OF NOTCH-FLAT: REGION 2

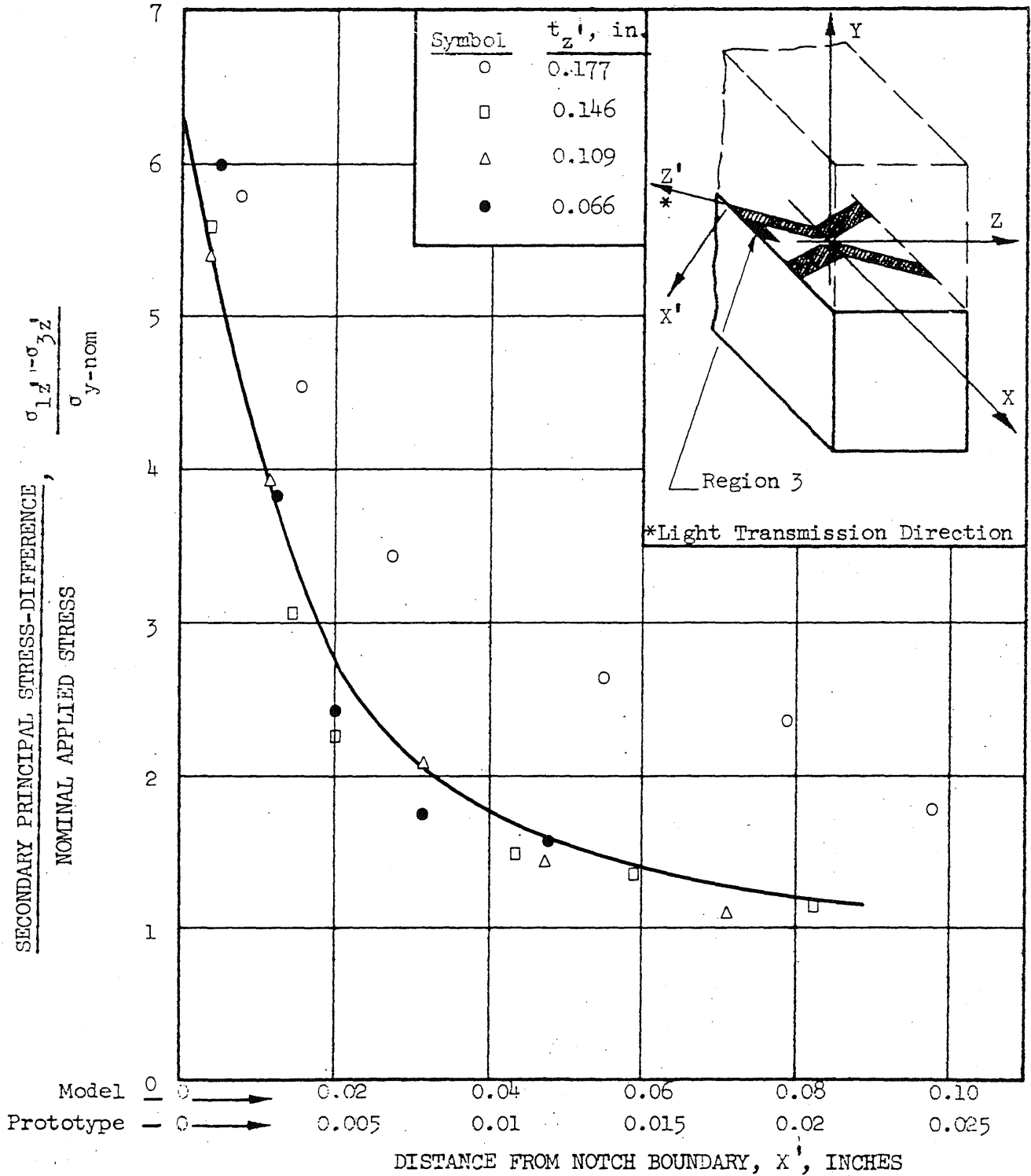


FIG. 4.19 SECONDARY PRINCIPAL STRESS-DIFFERENCE, $\sigma_{1z'} - \sigma_{3z'}$,
 NEAR NOTCH BOUNDARY AND MODEL SURFACE: REGION 3

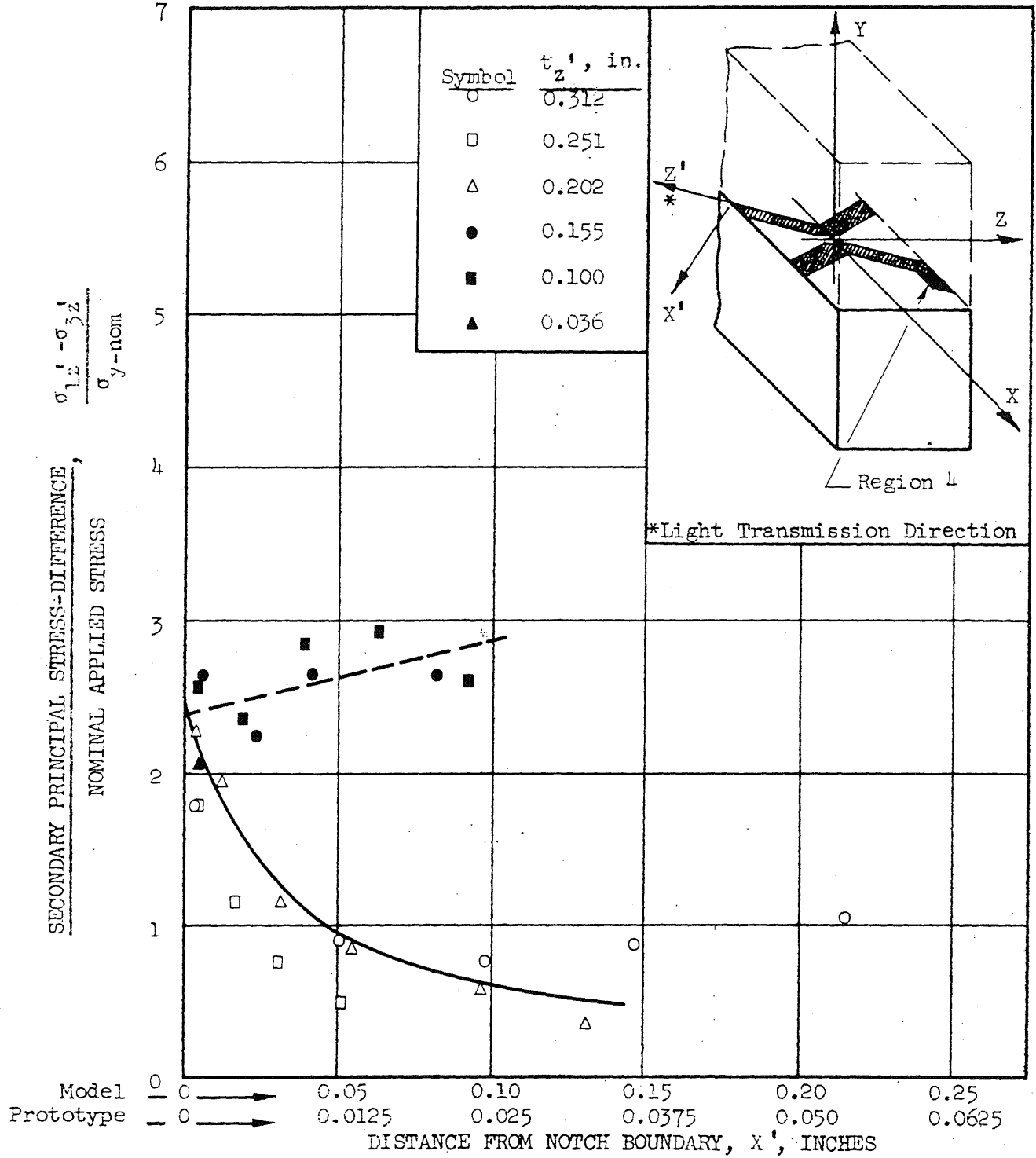


FIG. 4.20 SECONDARY PRINCIPAL STRESS-DIFFERENCE, $\sigma_{1z}' - \sigma_{3z}'$, NEAR NOTCH BOUNDARY AND MODEL SURFACE: REGION 4

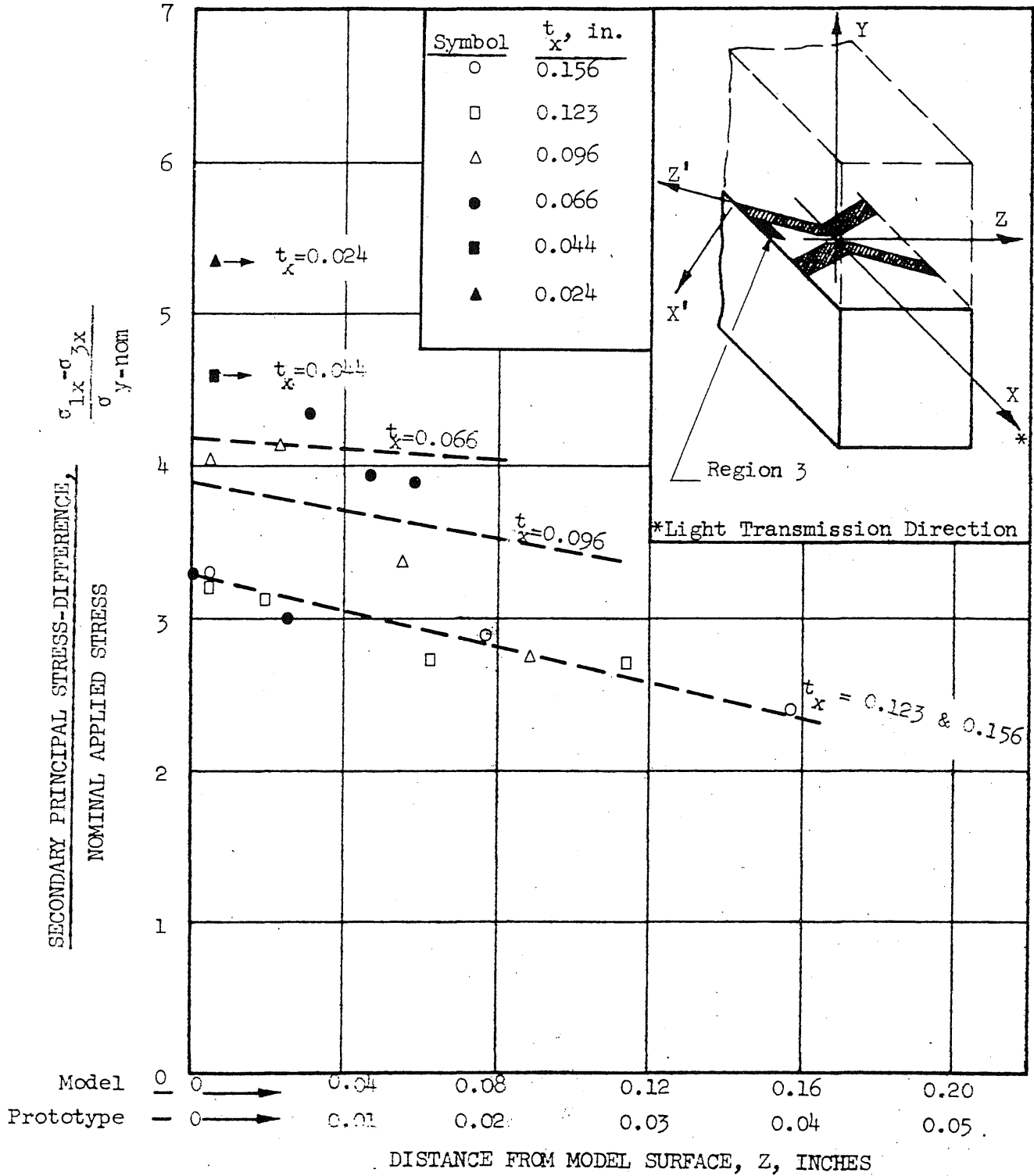


FIG. 4.21 SECONDARY PRINCIPAL STRESS-DIFFERENCE, $\sigma_{1x} - \sigma_{3x}$, NEAR NOTCH BOUNDARY AND MODEL SURFACE: REGION 3

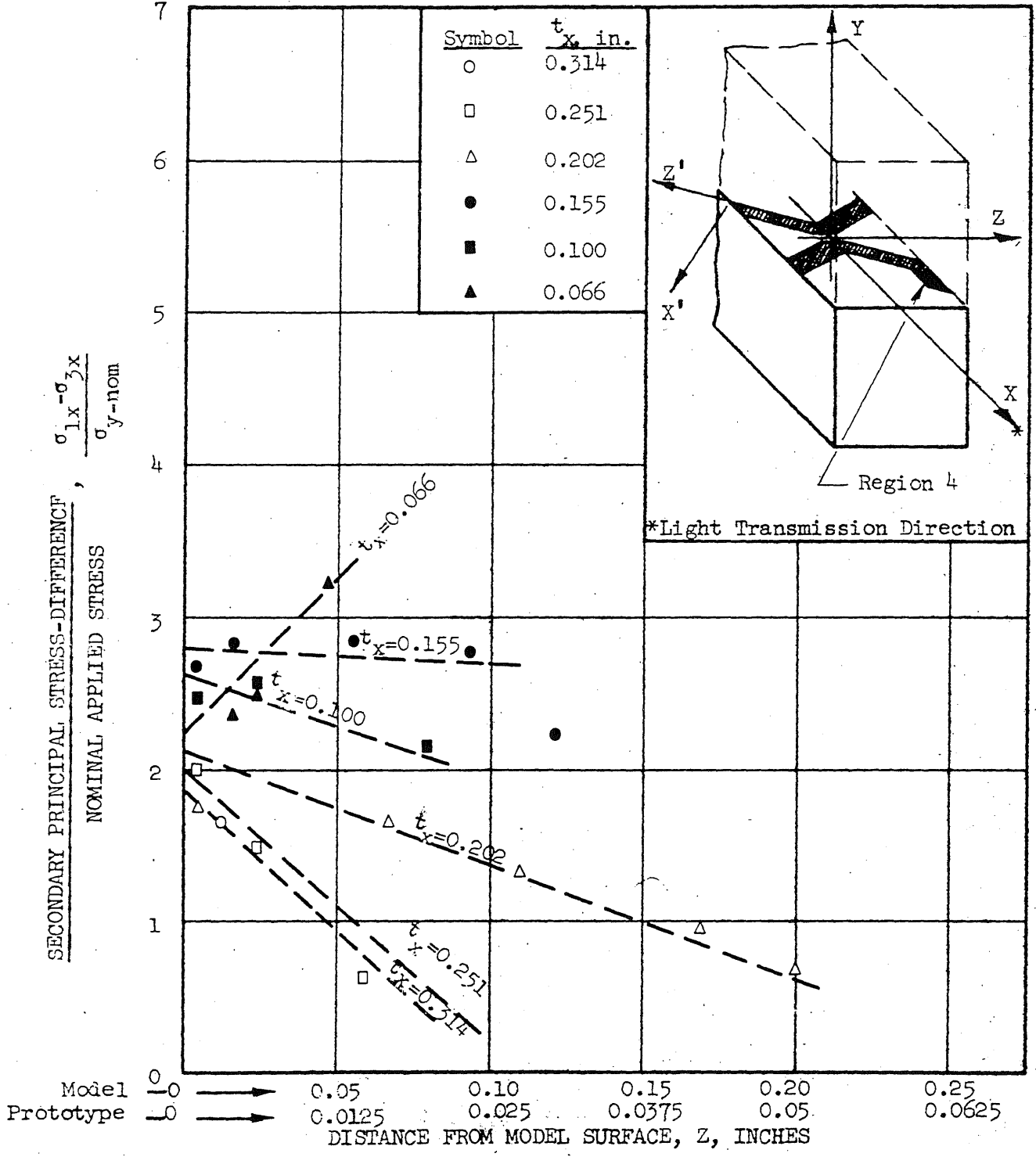


FIG. 4.22 SECONDARY PRINCIPAL STRESS-DIFFERENCE, $\sigma_{1x} - \sigma_{3x}$, NEAR NOTCH BOUNDARY AND MODEL SURFACE: REGION 4

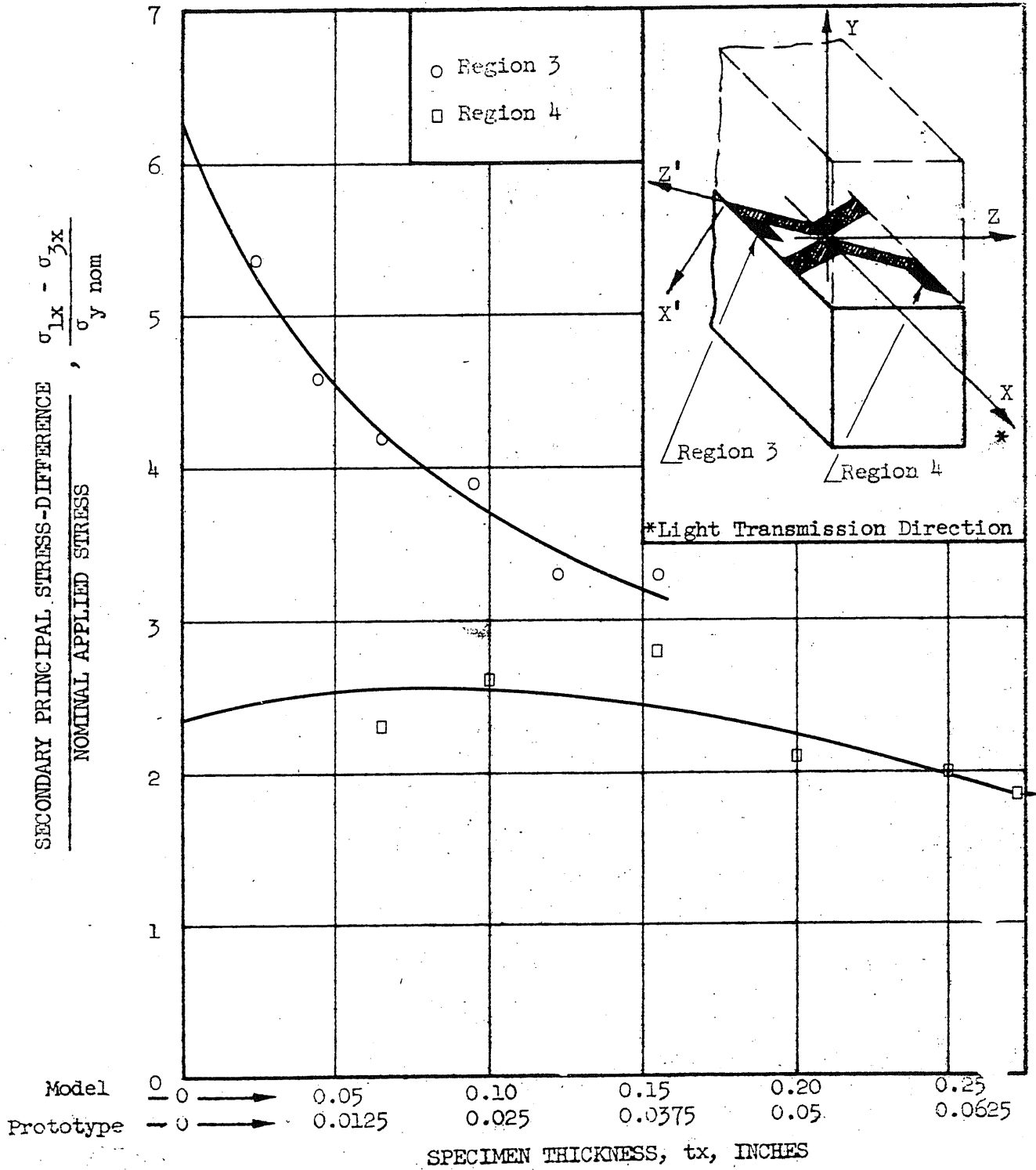


FIG. 4.23 SECONDARY PRINCIPAL STRESS-DIFFERENCE, $\sigma_{1x} - \sigma_{3x}$, AT MODEL SURFACE, VERSUS SPECIMEN THICKNESS: REGIONS 3 and 4

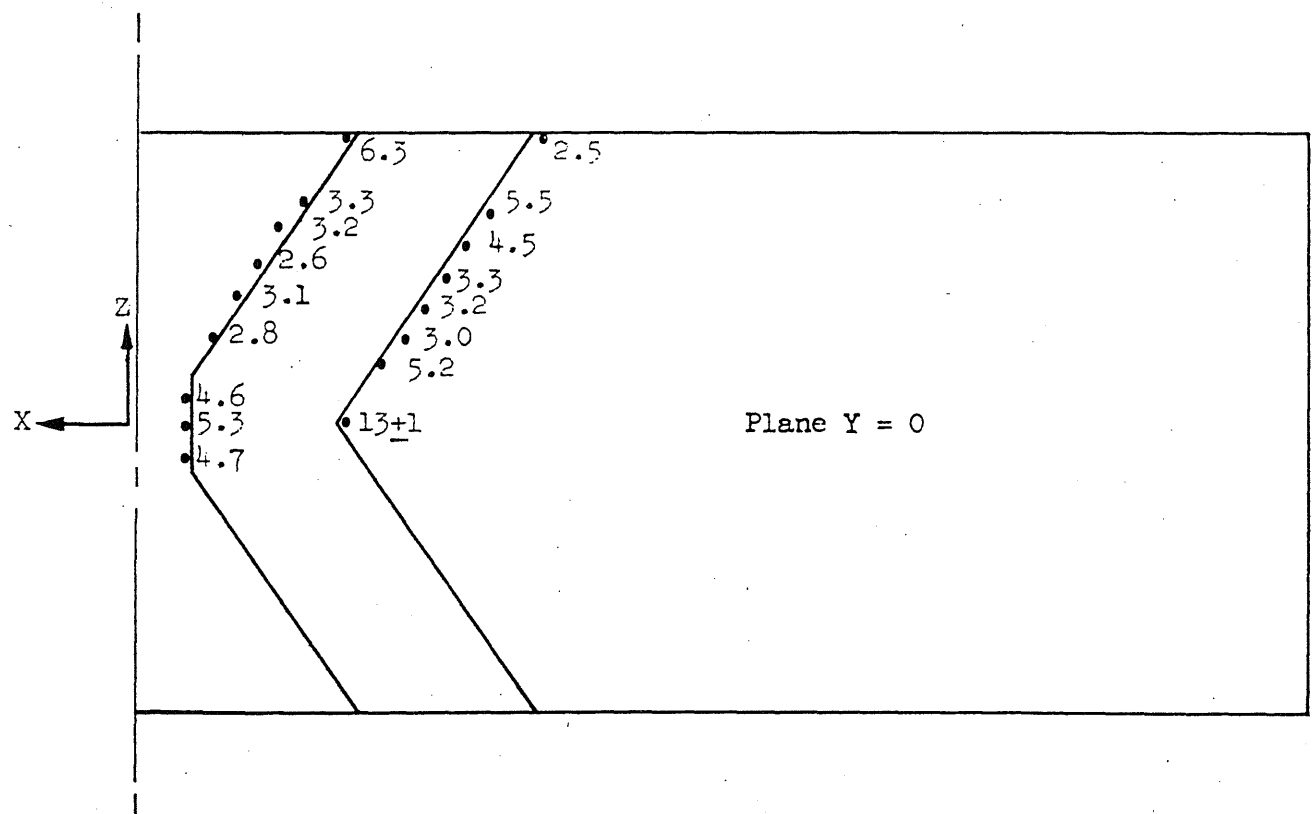
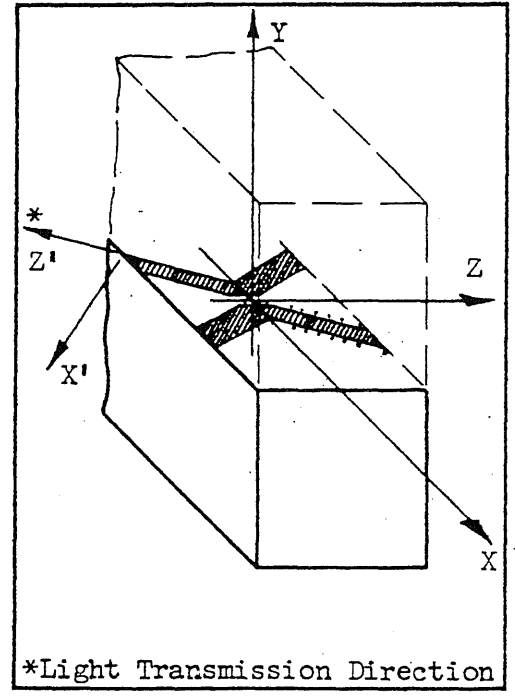
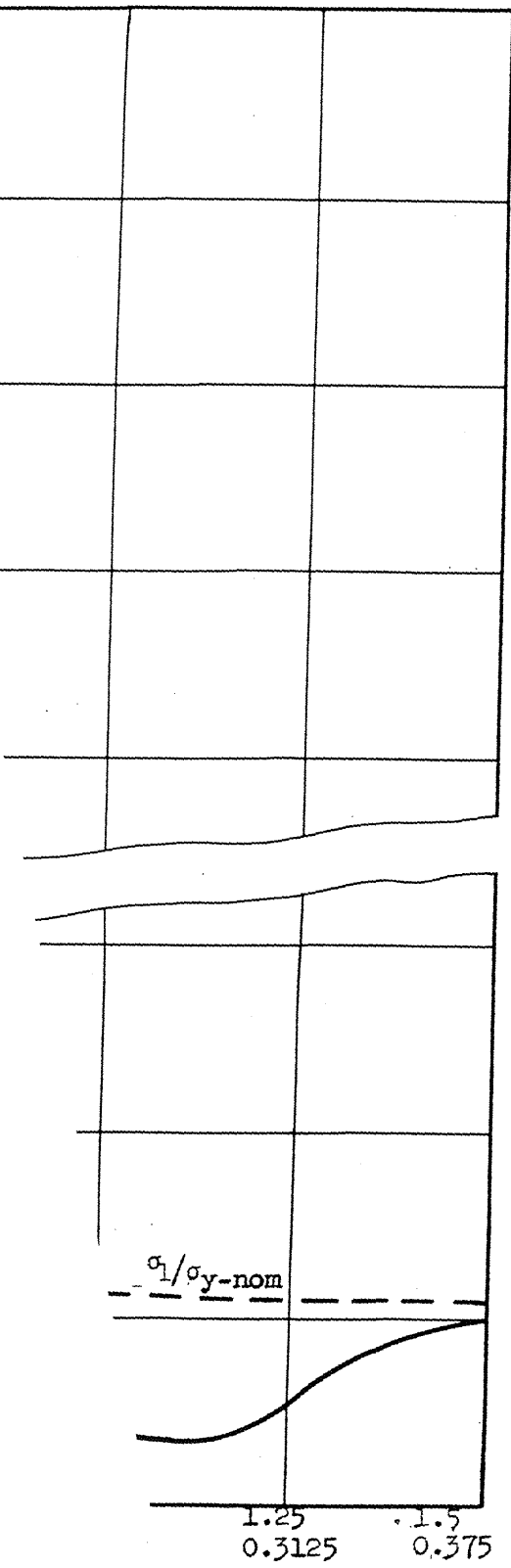


FIG. 4.24 MAXIMUM NORMAL STRESS, σ_y , AT SELECTED POINTS ON NOTCH PERIMETER

120



LENT

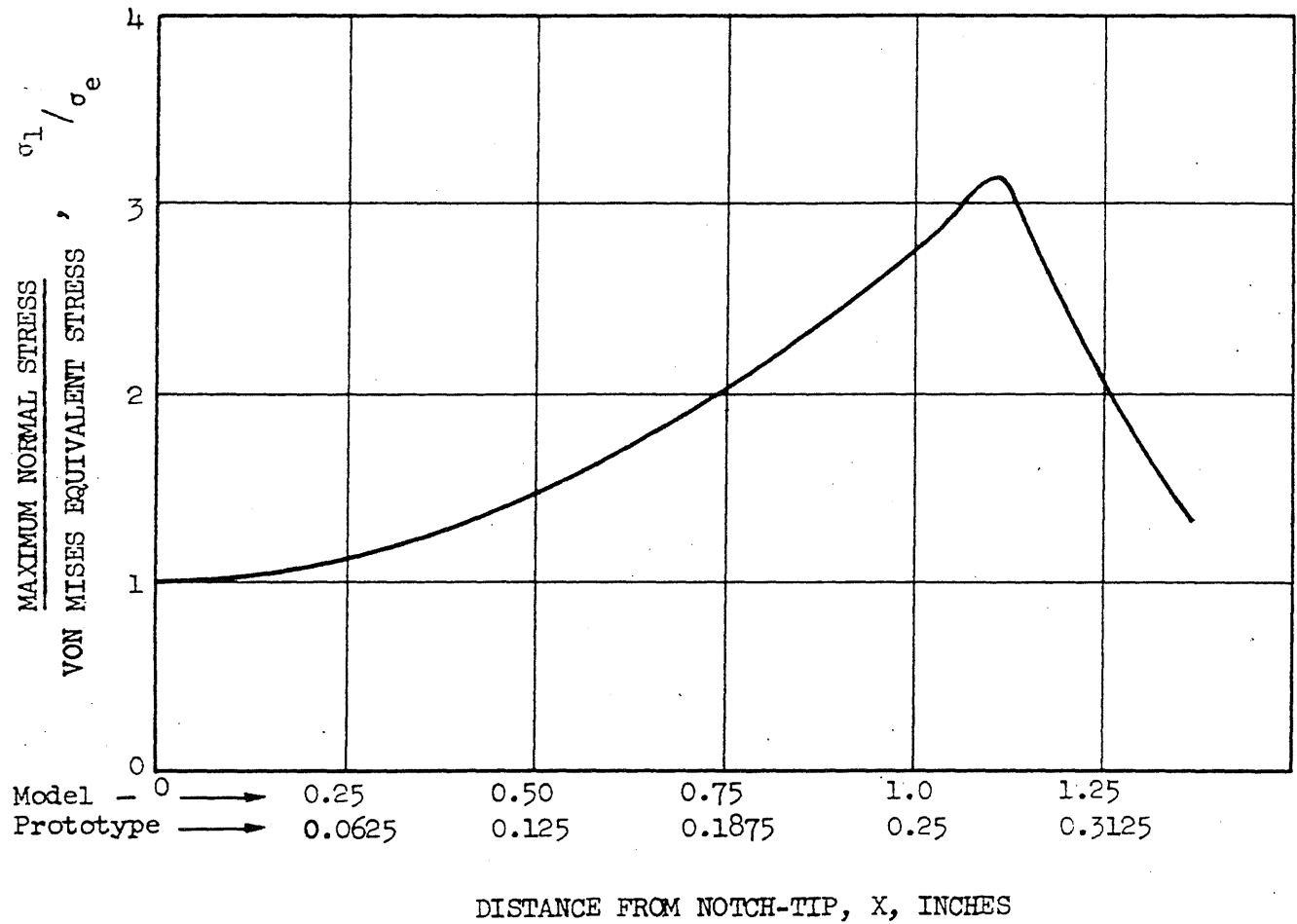


FIG. 5.2 RATIO OF MAXIMUM NORMAL STRESS AND VON MISES
EQUIVALENT STRESS VERSUS DISTANCE FROM NOTCH-TIP



FIG. 5.3 PHOTOMICROGRAPH (200 X) SHOWING CLEAVAGE CRACK INITIATION (Arrow)
IN REGION AWAY FROM NOTCH ROOT (From Knott and Cottrell⁴⁹)

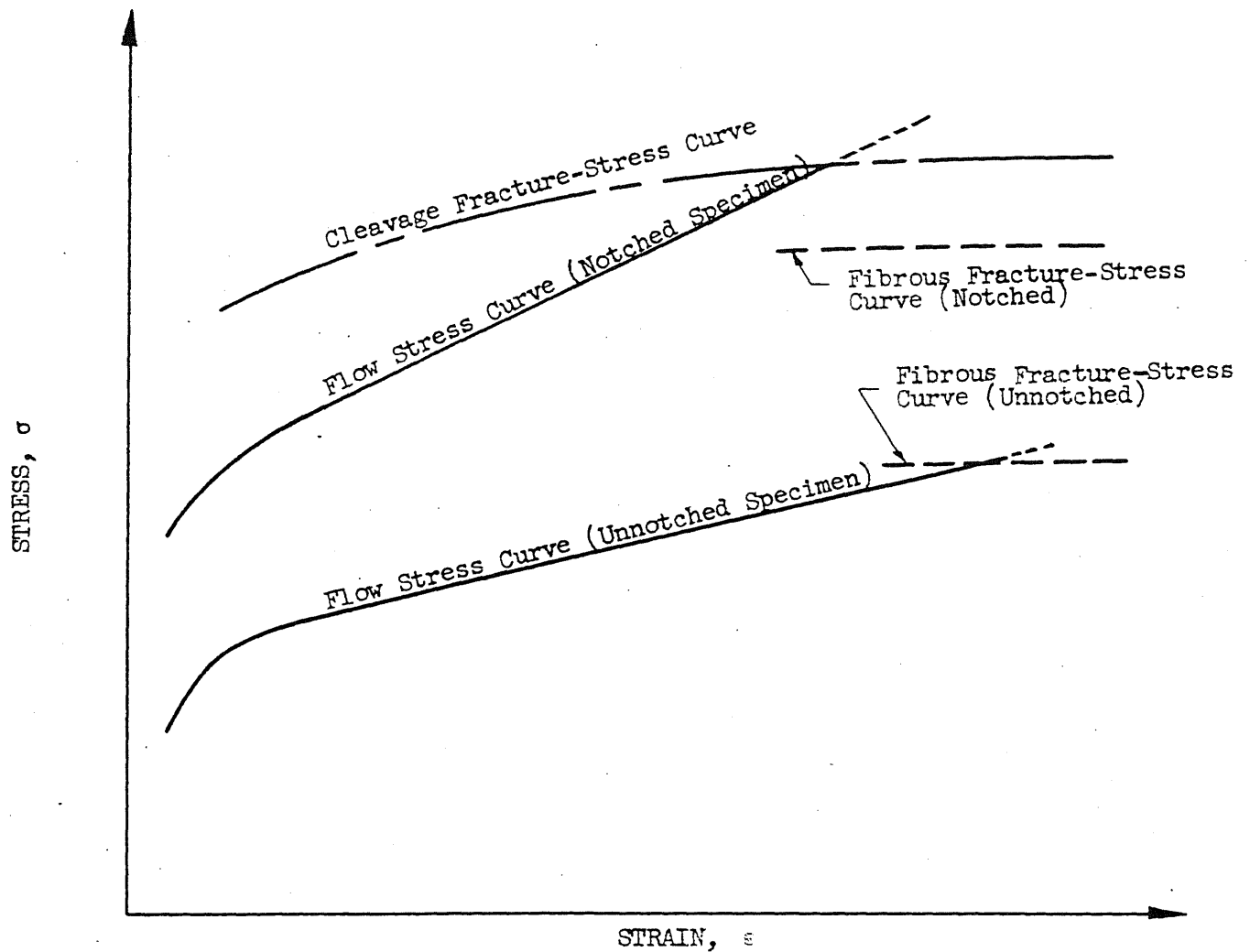


FIG. 5.4 THE ROLE OF A NOTCH IN THE DUAL FRACTURE MODE
BEHAVIOR OF STEEL (After Ōtani and Ideguchi⁽⁵¹⁾)

APPENDIX A

PRINCIPLES OF PHOTOELASTICITY

A.1. Stress-Optical Properties of Birefringent Materials^(41,42)

All materials retard transmission of light. The character of this retardation varies among different materials. A certain class of materials is termed stress-birefringent. These materials exhibit a unique, and measurable, relationship between the state of stress to which they are subjected and the characteristics of light transmitted through them.

Consider a model of birefringent material subjected to a state of plane-stress (Fig. A.1). Plane-polarized light, transmitted in a direction perpendicular to the plane of the model, is assumed to impinge on the model. The orientation of the model's principal stresses, with respect to the plane of polarization, is characterized by the angle θ . Compared to the surrounding air, the unloaded model transmits light at a reduced velocity, but otherwise does not alter it. The magnitude of the reduced velocity, V_m , is used to define the material's refractive index, n_o , by the relationship

$$n_o = \frac{V_a}{V_m} \quad (\text{A.1})$$

where V_a = velocity of light in air (strictly, in vacuum).

The addition of stress to the model causes alteration of the optical properties exhibited by the material. The light no longer

remains polarized in one plane, but splits into two components, each of which is plane-polarized and vibrates in one of the two principal-stress planes. Furthermore, each component exhibits its own retardation effect which is found to be related linearly to the principal stresses in the following manner:

$$\begin{aligned} n_1 - n_o &= A\sigma_1 + C\sigma_2 \\ n_2 - n_o &= A\sigma_2 + C\sigma_1 \end{aligned} \tag{A.2}$$

where A, C = material constants

n_1, n_2 = refractive indices honored by the light components associated with the planes on which the principal stresses, σ_1 and σ_2 , respectively, act.

The equations in Eq. (A.2) can be solved simultaneously for σ_1 and σ_2 to give

$$\begin{aligned} \sigma_1 &= \frac{A(n_1 - n_o) + C(n_o - n_2)}{A^2 - C^2} \\ \sigma_2 &= \frac{A(n_2 - n_o) + C(n_o - n_1)}{A^2 - C^2} \end{aligned} \tag{A.3}$$

The n_o term can be eliminated by subtracting σ_2 from σ_1 , yielding

$$\sigma_1 - \sigma_2 = \frac{n_1 - n_2}{A - C} \tag{A.4}$$

Upon emergence from the stressed medium, there will be an optical path-difference, δ , between the two light components of

$$\delta = t(n_2 - n_1) \tag{A.5}$$

where t is the thickness of the medium perpendicular to the direction of light transmission. The path-difference, δ , is related to the basic wave length, λ , by

$$\delta = N\lambda \quad (\text{A.6})$$

where N is the number of cycles of phase-difference. Equations (A.4), (A.5), and (A.6) lead to

$$\sigma_1 - \sigma_2 = \frac{\delta}{t(A - C)} = \frac{N\lambda}{t(A - C)} \quad (\text{A.7})$$

Equation (A.7) is the general form of the stress-optic relationship for two-dimensional stress-states. The number of cycles of phase-difference, N , is known as the fringe order. The fringes are rendered visible by insertion into the optical system of another filter which produces plane-polarized light. The position of this element, termed the analyzer, is beyond the model, as shown in Fig. A.1. The analyzer is usually oriented with its axis of polarization perpendicular to that of the polarizer. Without altering the phase-difference between light components, the analyzer projects them onto a single plane so that their effect on each other visibly displays itself in the well-known fringe patterns. Minimum light intensity (extinction) occurs when the two light components are an integral number of wave lengths out-of-phase. Maximum light intensity occurs when there is a one-half wave length phase-difference.

The material constants, A and C , in Eq. (A.7) are usually combined with the light wave length, λ , to form a term, F , defined as

$$F = \frac{\lambda}{A - C} \quad (\text{A.8})$$

Equation (A.7) can now be written in a less general, but more familiar, form as

$$\sigma_1 - \sigma_2 = \frac{NF}{t} \quad (\text{A.9})$$

where F must now be evaluated for the material and wave length of light, which can be considered constant if monochromatic light is used.

By using white light one other important piece of information can be learned from the optical examination of the model (Fig. A.1) in the plane-polariscope. It is clear that if the orientation of the principal-stress axes coincides with that of the polarizer-analyzer axes, extinction will occur. This provides a method for determining principal stress orientation.

The stress-optical laws for three-dimensional stress-states do not differ, fundamentally, from those governing the plane-stress model used in the previous development. Equation (A.2) can be generalized to account for the additional principal stress component, σ_3 . Polarized light, impinging normally on the plane on which σ_3 acts, will be relatively retarded by an amount proportional to the principal stress difference, $\sigma_1 - \sigma_2$. The proportionality is expressed by Eq. (A.9). Similar relationships hold for the other principal directions leading to

$$\sigma_1 - \sigma_2 = \frac{N_3 F}{t_3}$$

$$\sigma_2 - \sigma_3 = \frac{N_1 F}{t_1} \quad (\text{A.10})$$

$$\sigma_3 - \sigma_1 = \frac{N_2 F}{t_2}$$

where the subscripts on fringe order, N , and thickness, t , refer to the direction of light transmission.

A more general three-dimensional case involves polarized light's impinging normally on a non-principal plane. The relative retardation is not affected by the normal stress on the plane of light incidence or by shear stresses on this plane.⁽⁴¹⁾ The stresses which follow a proportionality law of the type expressed by Eq. (A.10) are the components of the principal stresses which act in a direction perpendicular to the direction of light transmission. In order to differentiate them from true principal stresses, these components are termed "secondary principal stresses." Stress-optic equations for the secondary principal stresses will be developed in Appendix A.2.

A.2. Photoelastic Determination of the von Mises Equivalent Yield Stress⁽⁴⁵⁾

The von Mises yield criterion postulates that material flow will impend when the shear-deformation energy reaches a certain constant value. A body's shear-deformation energy can be formulated in general terms by subtracting the dilatational energy from the total strain energy. The latter can be expressed as

$$U = \iiint_V \frac{1}{2} (\sigma_x \epsilon_x + \sigma_y \epsilon_y + \sigma_z \epsilon_z + \tau_{xy} \gamma_{xy} + \tau_{xz} \gamma_{xz} + \tau_{yz} \gamma_{yz}) dx dy dz \quad (\text{A.11})$$

where the integrand is the strain energy density, termed U_o . The following formulation is in terms of energy densities, since yielding occurs when the energy condition is satisfied anywhere. The strain energy density, U_o , can be expressed completely in terms of stresses by use of the stress-strain relationships

$$\begin{aligned}
 \epsilon_x &= \frac{1}{E} [\sigma_x - \mu(\sigma_y + \sigma_z)] \\
 \epsilon_y &= \frac{1}{E} [\sigma_y - \mu(\sigma_x + \sigma_z)] \\
 \epsilon_z &= \frac{1}{E} [\sigma_z - \mu(\sigma_x + \sigma_y)] \\
 \gamma_{xy} &= \frac{\tau_{xy}}{G} \\
 \gamma_{yz} &= \frac{\tau_{yz}}{G} \\
 \gamma_{xz} &= \frac{\tau_{xz}}{G}
 \end{aligned} \tag{A.12}$$

Substitution of Eq. (A.12) into the expression of U_o in Eq. (A.11) leads to

$$U_o = \frac{1}{2E} \left[(\sigma_x^2 + \sigma_y^2 + \sigma_z^2) - \frac{\mu}{E} (\sigma_x \sigma_y + \sigma_y \sigma_z + \sigma_z \sigma_x) + \frac{1}{2G} (\tau_{xy}^2 + \tau_{yz}^2 + \tau_{zx}^2) \right] \tag{A.13}$$

The dilatational (hydrostatic) strain energy, U_{od} , per unit volume is defined as

$$U_{od} = \frac{1}{2} \cdot \frac{1}{3} [\sigma_1 + \sigma_2 + \sigma_3][\epsilon_1 + \epsilon_2 + \epsilon_3] = \frac{1}{6} I_1 J_1 \tag{A.14}$$

where I_1 and J_1 are the first stress and strain invariants, respectively.

Equation (A.14) can be written in terms of the coordinate stress components by use of Eq. (A.12), together with the stress and strain invariant definitions. The result is

$$U_{od} = \frac{1 - 2\mu}{12(1 + \mu)G} (\sigma_x + \sigma_y + \sigma_z)^2 \quad (A.15)$$

The shear-deformation energy density, U_{os} , is obtained by subtracting Eq. (A.15) from Eq. (A.13):

$$U_{os} = U_o - U_{od} = \frac{1}{12G} \left[(\sigma_x - \sigma_y)^2 + (\sigma_y - \sigma_z)^2 + (\sigma_z - \sigma_x)^2 + 6(\tau_{xy}^2 + \tau_{yz}^2 + \tau_{xz}^2) \right] \quad (A.16)$$

To tie the shear-deformation energy to a known yield condition, the stress-state for uniaxial coupon testing is adopted. The direction of applied load is assumed to coincide with the Y direction. Then, for yielding to occur, $\sigma_x = \sigma_z = \tau_{xy} = \tau_{yz} = \tau_{xz} = 0$; $\sigma_y = \sigma_{yp}$ where σ_{yp} is the material's conventionally-determined yield point. For the uniaxial case considered, Eq. (A.16) gives

$$U_{os} = \frac{1}{12G} (2\sigma_y^2) = \frac{\sigma_{yp}^2}{6G} \quad (A.17)$$

Equation (A.17) establishes the value of U_{os} for which yielding will impend. Accounting for a possible non-yield condition by replacing σ_{yp} with the so-called von Mises equivalent stress, σ_e , leads, by combining Eqs. (A.16) and (A.17), to

$$2\sigma_e^2 = \left[(\sigma_x - \sigma_y)^2 + (\sigma_y - \sigma_z)^2 + (\sigma_z - \sigma_x)^2 + 6(\tau_{xy}^2 + \tau_{yz}^2 + \tau_{xz}^2) \right] \quad (\text{A.18})$$

Equation (A.18) expresses the von Mises equivalent stress condition in terms of the coordinate stress components.

A physical interpretation of Eq. (A.18) is possible. The right side of the equation represents the stress state's yielding power, which is sufficient to cause yielding if the equivalent stress, σ_e , computed from Eq. (A.18), equals or exceeds the uniaxial yield value, σ_{yp} . Thus, comparing the direct computation of σ_e from Eq. (A.18) with the material's uniaxial yield stress reveals the propensity of the material at the point in question to yield. It remains to note that Eq. (A.18) can be written in terms of principal stresses as

$$2\sigma_e^2 = (\sigma_1 - \sigma_2)^2 + (\sigma_2 - \sigma_3)^2 + (\sigma_3 - \sigma_1)^2 \quad (\text{A.19})$$

The form of Eq. (A.19) suggests that photoelasticity can be applied to determine the Mises stress, σ_e , if relative retardation measurements corresponding to the terms in the right side of Eq. (A.19) are made. For a "cube" of material into which birefringence is fixed, the relative retardations in the three orthogonal principal directions provide the desired principal stress-differences directly. That is, by using Eq. (A.10) from Appendix A.1, Eq. (A.19) can be written as

$$2\sigma_e^2 = \left[\frac{N_3 F}{t_3} \right]^2 + \left[\frac{N_1 F}{t_1} \right]^2 + \left[\frac{N_2 F}{t_2} \right]^2 \quad (\text{A.20})$$

or for true cubes of side t

$$2\sigma_e^2 = \left(\frac{F}{t}\right)^2 (N_1^2 + N_2^2 + N_3^2) \quad (\text{A.21})$$

The Mises stress can also be evaluated photoelastically for a more generally chosen cube, in which cube faces are not necessarily principal planes (Fig. A.2(a)). The orthogonal, but otherwise arbitrary, axes of the cube are denoted X, Y, Z . The retardation measurements, N , and the orientation, θ , of the secondary principal stresses for light incidence on a given plane are functions of the stresses not acting on that plane. Therefore, $(N_x, \theta_x) = f(\sigma_y, \sigma_z, \tau_{yz})$, etc., where the subscripts on N and θ denote the direction of light transmission. The functions relating the stress components can be found by referring to Fig. A.2(b), in which light transmission in the X direction is presumed. From the geometry of the figure it is seen that

$$D_x^2 = (\sigma_y - \sigma_z)^2 + 4\tau_{yz}^2 \quad (\text{A.22})$$

and

$$\tau_{yz}^2 = (D_x/2)^2 \sin^2 2\theta_x \quad (\text{A.23})$$

where D_x is the Mohr circle diameter, equal to the difference of secondary principal stresses, $\sigma_{1x} - \sigma_{3x}$. Photoelastically, D_x is given by

$$D_x = \sigma_{1x} - \sigma_{3x} = \frac{N_x F}{t_x} \quad (\text{A.24})$$

Equations (A.22), (A.23), and (A.24) represent light transmission in

the X direction. For light transmission in the Y and Z directions, additional equations are obtained by an appropriate permutation of the indices.

Using Eq. (A.18), which expresses the Mises equivalent stress in terms of the coordinate stresses, as the basic equation into which substitutions are made from Eqs. (A.22), (A.23), and (A.24) leads to

$$\sigma_e^2 = \left(\frac{F}{2t}\right)^2 \left[N_x^2 (2 + \sin^2 2\theta_x) + N_y^2 (2 + \sin^2 2\theta_y) + N_z^2 (2 + \sin^2 2\theta_z) \right] \quad (\text{A.25})$$

Equation (A.25) is used to determine the Mises stress for any arbitrary cube, without resort to terms other than the usual photoelastic parameters, N and θ , for the three orthogonal directions, X, Y, and Z.

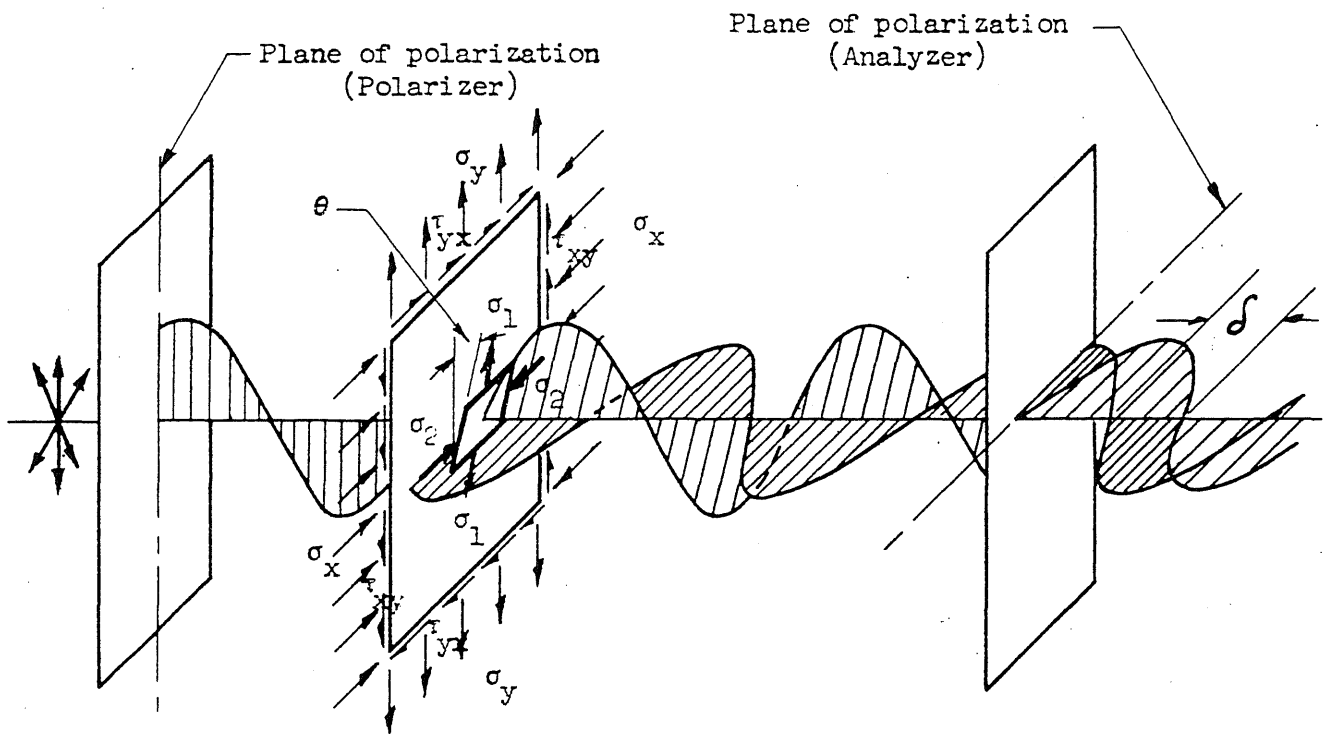
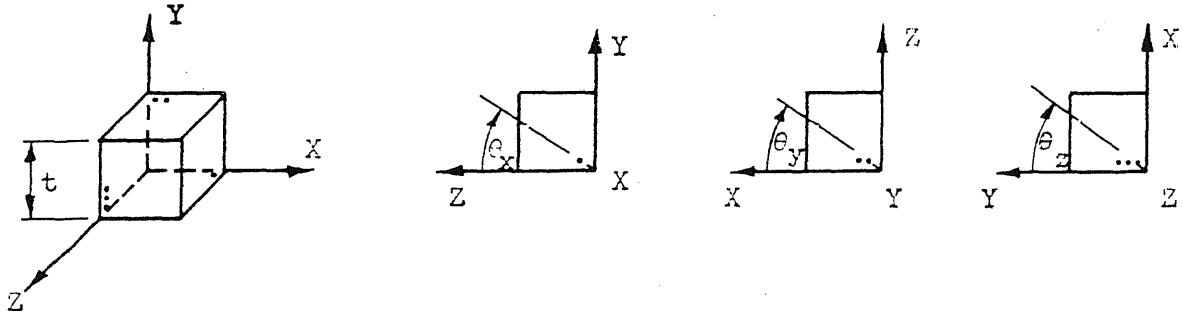


FIG. A.1 RETARDATION OF POLARIZED LIGHT TRANSMITTED THROUGH A PLANE-STRESS MODEL

(a) ORIENTATION OF CUBES CUT FROM PHOTOELASTIC MODEL



(b) MOHR CIRCLE REPRESENTATION OF SECONDARY PRINCIPAL STRESSES

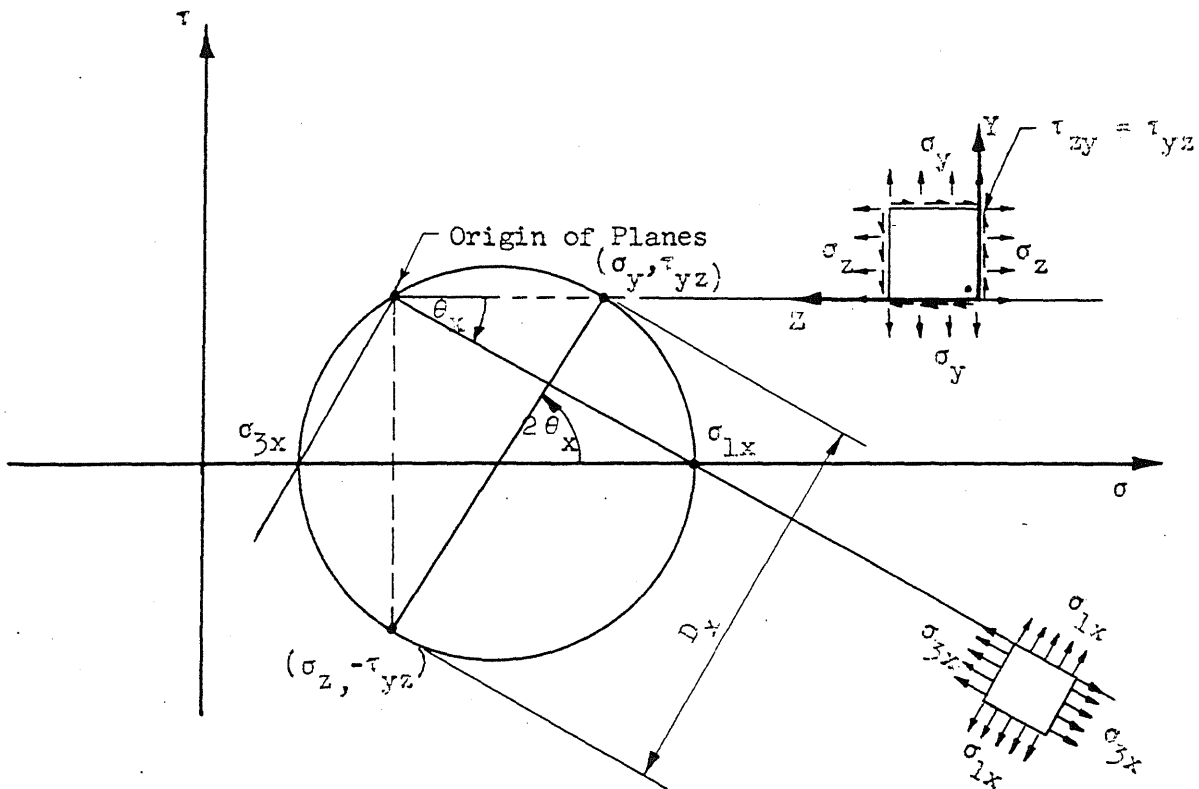


FIG. A.2 SECONDARY PRINCIPAL STRESSES IN ARBITRARILY ORIENTED CUBES CUT FROM MODEL INTO WHICH STRESSES HAVE BEEN FROZEN

APPENDIX B

NOTATION*

A	constant
a	crack length
B	brittle strength curve
b	length
C	constant
c	subscript denoting critical values
D	secondary principal stress-difference
E	Young's modulus
F	optical constant
G	crack-extension force; also shear modulus
I	moment of inertia
I_1	first stress tensor invariant
J_1	first strain tensor invariant
K	stress intensity factor
K_p, K_s	stiffnesses of epoxy polymer primary and secondary phases
L	wide-plate specimen width
M	bending moment
m	fringe-multiplication
N	fringe-order
n	refractive index

* For specificity, subscripted variations of this basic notation occur; all notation is defined in the text as it first occurs.

P	primary phase
q	constraint factor
R	load on epoxy model
r	polar coordinate
S	secondary phase
T	temperature
t	thickness
U	total strain energy
U_0	strain energy density
V	total potential energy
V_a	velocity of light in air
V_m	velocity of light in photoelastic model material
W	potential energy of surface tension
X,Y,Z	rectangular coordinate axes
x,y,z	rectangular coordinate axes, calibration beam
Y_d	ductile strength curve
α	surface tension
γ	shear strain
Δ	elongation
δ	optical path-difference
ϵ	tensile strain
θ	isoclinic angle; also polar coordinate
λ	wave length
μ	Poisson's ratio
σ	normal stress
σ_e	von Mises equivalent yield stress

$\sigma_{y\text{-nom}}$ nominal applied stress
 σ_{yp} uniaxial yield stress
 τ shear stress